Development of microfabricated optical chemical sensor platforms using polymer processing technology

By

Conor Stephen Burke B.Sc. (Hons)

A Thesis presented

to

Dublin City University

For The Degree Of Doctor Of Philosophy

Research Supervisor:

Prof. Brian D. MacCraith,

School of Physical Sciences,

Dublin City University.

July 2004

Declaration

I hereby certify that this material, which I now submit for assessment on the programme of study leading to the award of Doctor of Philosophy is entirely my own work and has not been taken from the work of others save and to the extent that such work has been cited and acknowledged within the text of my work.

Signed: Conor Burke (Candidate) ID No.: 95035761

Date: 15/09/04

Dedication

To Mam and Dad

Acknowledgements

Over the past few years, I've received highly valued support and encouragement from several sources. Firstly, I'd like to thank all members of the Optical Sensors Laboratory, past and present, for helping to provide an ideal research environment and for being the most professional (and sociable!) group of people I've worked with. Thanks in particular to Phil, John, Kieran, Pat, Honza, Jean-Marc, Ondra, Henry, Adam and Orla for their input!

For invaluable assistance in the use of the CNC micromiller and the fabrication of moulds, thanks are due to Des Lavelle, Cian Merne and Nigel Kent. Thanks also to Des for all his machining services over the past few years, always of the highest quality irrespective of his workload!

Thanks to Lubos Polerecky for the invaluable insights into efficient experimental development and management that I gained from working with him.

I can't forget to thank Aisling, the second-busiest person I know, for always being on hand to discuss project issues. I don't know how you managed to make time but it was much appreciated. I'd also like to thank Colette for her help in understanding all things related to oxygen sensing.

Now to the busiest person I know, my supervisor Brian MacCraith. I feel privileged to have worked in a centre involved in such applied, cutting-edge research and I'm extremely grateful to have been allowed to pursue my Ph.D. under your supervision. Your drive and scientific vision have helped show me what research is all about (and I'm not being smart!).

On a more personal note, I'd like to thank my friends, both from home and from my undergrad years, who have put up with such a pauper as a friend for such a ridiculously long time. My parents have given me unwavering support — both mental and financial when necessary — and "thanks" doesn't express my gratitude adequately (but it'll have to do!). Thanks also to my brother, John and my sisters, Stephanie and Suzanne for not being afraid to tell me to be quiet when I was boring them! To Christoph, not only were you my "chemistry guru", you were an excellent friend. Finally, I could quite easily have run amok were it not for the calming influence of my girlfriend, Helen. Thank you for putting up with me and helping me to get past the various obstacles this project has thrown at me.

Abstract

This work describes the design and fabrication of enhanced polymer waveguide platforms for absorption-based optical chemical sensors and the use of soft lithographic techniques for the fabrication of optical sensor chips. The design of the enhanced polymer waveguide platforms was based on a previously reported theoretical model that was verified experimentally in this work. The platforms were fabricated by micro-injection moulding and subsequently coated with sol-gel-derived sensing layers doped with a colorimetric indicator compound. The sensor response to both gaseous ammonia and solution pH was examined using a LED-based prototype sensor head. Soft lithographic patterning techniques, based on the use of a poly(dimethylsiloxane) (PDMS) patterning element, were employed to produce a variety of sol-gel-based structures with applications in optical sensing. These included discrete sensor spots, surface corrugation grating couplers and ridge waveguides. As a proof of principle, these techniques were applied to the development of an integrated optical oxygen sensor based on the quenching of fluorescence from a sol-gel-encapsulated ruthenium complex that was deposited as a sensor spot onto a ridge waveguide. This work highlights the feasibility of using rapid prototyping technology to fabricate sensitive, mass-producible sensor platforms that employ generic configurations, thereby facilitating their use in a broad range of applications.

Contents

Chapter 1

Introduction

1.1 Introduction

Sensors are devices that provide continuous, reversible monitoring of physical parameters or of concentrations of chemical or biological target analytes. They exist in many forms and are rapidly becoming an integral part of modern society. Applications are wide-ranging and include areas as diverse as environmental monitoring, Formula One racing and biometrics and new applications are developed on a regular basis. Sensors exploit a variety of transduction mechanisms including electrical, electrochemical, thermal, mechanical and optical phenomena. This thesis concentrates on the development of optical sensors.

Recent developments in microsystems technology have led to the widespread application of microfabrication techniques for the production of sensor platforms. The evolution of these techniques is due primarily to the semiconductor industry and the need to improve the efficiency and speed of integrated circuits. However, polymer processing technology has also had a major influence on microfabrication techniques, the most obvious example of this being compact disc (CD) technology. These techniques have had a major impact on the development of so-called "Lab-on-a-Chip" devices. These devices are intended to provide quantitative chemical or biochemical information on samples such as blood, sweat and saliva while using minimal sample volume. One of the ultimate aims of this area of work is the development of diagnostic "chips" that can be used in point-of-care applications and, in certain situations, reduce the frequency of hospital visits by

people suffering from chronic or long-term illnesses. The production of micro- and nanometer-scale devices has enormous implications for the development of highly sensitive sensor platforms that can yield quantitative information about systems on a molecular level and the field of optical sensor research has been quick to embrace these technologies and their associated potential.

In order to effectively establish the viability of a particular sensor concept, it has become necessary to develop rapid, flexible fabrication protocols that facilitate the production of prototype sensor platforms within a relatively short time frame, e.g, 24 hours. This process is known as "rapid prototyping" and has become a powerful tool for the development of microsystems for sensing applications.

The impetus behind the work reported here was the development of generic, potentially disposable platforms for optical chemical sensors by exploiting microfabrication and rapid prototyping techniques and integrating them with well-established optical transduction techniques.

1.2 Optical sensors

Optical sensors are devices that employ light in order to monitor physical parameters or chemical / biological analytes. Optical physical sensors have been developed for a range of parameters including strain [1, 2], temperature [3, 4] and pressure [5, 6]. However, the focus of this thesis is on optical chemical sensors and on the transduction techniques typically employed for the detection of chemical species. Optical chemical sensors may exploit any of the broad range of spectroscopic phenomena available as well as other analyte-sensitive optical phenomena. However, the vast majority of reported systems can be divided into three main groups – absorption-based, fluorescence-based and refractometry-based. In the case of fluorescence-based sensors, the presence of the target analyte modifies the fluorescence properties of the indicator material, e.g., causes a reduction in the level of fluorescence due to dynamic (collisional) quenching. Sensors employing refractometry exploit the change in the real part of the refractive index caused by the presence of the analyte to yield a sensor response. However, the work reported here has concentrated primarily on the development of platforms for absorption-based optical chemical sensors.

Absorption-based sensors can rely on the intrinsic absorbance of a particular analyte, in which case the method of detection is that of direct spectroscopy. In this case, the target analyte itself absorbs light at the interrogating wavelength. Alternatively, the sensing principle can be reagent-based, i.e., based on the detection of a colour change due to an analyte-sensitive indicator compound, for example a pH-sensitive dye. The latter method, despite being arguably an indirect detection mechanism, offers a distinct advantage over direct spectroscopy. This becomes apparent when the required light sources for the two methods are considered. Direct spectroscopy typically requires sources in the near ultraviolet wavelength range (e.g., for the detection of nitrate) or in the near to mid-infrared range (e.g., ammonia, methane or water detection systems). While several light sources that cover these wavelength ranges are available, they are typically quite expensive and not always well suited to deployment outside a laboratory environment. In contrast, reagent-based systems are compatible with low-cost LED's, which are available with emission spectra covering a large fraction of the visible wavelength range. These sources are low-cost and robust, making them attractive candidates for the development of rugged sensor platforms. Reagent-based sensor platforms were, therefore, a logical choice for the work reported here.

Although there are several commonly employed transduction mechanisms (e.g., electrochemical), for the development of chemical sensors, optical sensors offer several advantages over these other sensor types:-

1. Due to the fact that sensor information is provided by optical means, the signal is not influenced by electrical interference.

2. The reversible nature of many optical sensing mechanisms means that the analyte concentration is not modified during sensing, i.e., the sensor does not consume the analyte.

3. Optical sensors are suitable for use in explosive / hazardous environments due to the low possibility of sparking presented by them.

4. Optical microsystems are not limited in size by the inclusion of electrodes, thus providing a means for more compact, portable sensor platforms.

5. In the past, optical sensing was limited by the range of available light sources. However, with the advent of UV, blue and white light emitting

diodes (LED's) and green and blue laser diodes (LD's), it is now possible to address reagent-based systems (including those relying on fluorescence excitation) over most of the visible spectrum. This increases the number of indicator / fluorescent compounds that can be used, thus extending the range of detectable analytes so that optical sensors can no longer be seen as severely limited by a lack of suitable light sources.

While it is true that the advances mentioned above have made optical sensors an increasingly attractive choice, there are some challenges that need to be addressed:

1. The signal from absorption and fluorescence intensity-based optical sensors can be influenced by ambient light, necessitating the use of optical isolation and / or lock-in detection techniques. In the case of fluorescence-based systems, the use of phase fluorometric techniques [7, 8] can help overcome this issue.

2. The use of indicator compounds exposes the sensor to the problems of photobleaching and leaching, both of which adversely affect the long-term stability of the sensor.

3. Optoelectronic components such as LED's and photodiodes suffer from signal drift due to aging and / or temperature, making signal referencing an important issue in sensor development.

4. As alluded to in the previous point, optical sensors are temperature sensitive. Temperature referencing techniques are therefore required for the development of a reliable sensor.

Many of the above problems can be addressed through correct choice of indicator compound and sensing mechanism coupled with adequate referencing techniques. It should also be pointed out that problems such as electronic drift and temperature compensation are not particular to optical sensors and need to be addressed in any system employing electronic circuitry.

Given the popularity of optical sensors, it is not surprising that they exist in many different configurations and employ various methods of optical interrogation. Some of the most common configurations are described in Chapter 5 but the configuration of most interest here is that based on waveguide interactions.

1.3 Waveguide-based sensor platforms

An optical waveguide is a device, formed from a high dielectric material, that confines and transports electromagnetic radiation with wavelengths lying in the visible or near-infrared portions of the spectrum. This section briefly outlines the various configurations employed for waveguide-based sensing applications.

1.3.1 Optical fibre-based sensors

Optical fibre-based sensors employ waveguiding to yield a signal and Fig. 1.1 is a generalised illustration of light propagation within an optical fibre.

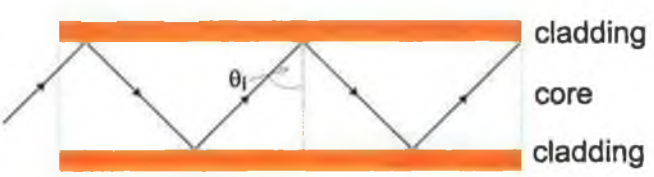

Figure 1.1: An optical fibre-based waveguide.

An optical fibre typically consists of a high refractive index core (e.g., silica) surrounded by a lower index cladding. The cladding layer can be surrounded by a protective jacket (not shown) depending on the application. Light propagates in the fibre by total internal reflection at the core - cladding interface. In this regime of propagation, the light is not confined solely to the core of the fibre as suggested by the ray optics representation shown in Fig. 1.1. Instead, the exponential tail of the propagating electromagnetic radiation extends into the cladding. This is known as the evanescent field of the propagating light. In sensor applications, the evanescent field provides information on the optical properties of the fibre cladding, providing the basis for evanescent-wave optical fibre sensors. For such sensors, the cladding often consists of a porous polymer material doped with an indicator phase. The porous cladding acts as a permeable membrane through which the target analyte is free to diffuse. Any changes in the absorption properties of the cladding result in changes in the output light intensity from the fibre due to the absorption of the evanescent wave by the doped cladding.

Extensive research has been carried out on optical fibre-based sensors which exploit evanescent-wave sensing [9, 10, 11, 12] and systems which facilitate the development of both probe-type [13, 14] and distributed sensor systems [15, 16, 17].

However, there are several disadvantages associated with the use of optical fibres as sensor elements that make them unsuited to the development of the optical sensor systems that form the focus of the work reported here. The majority of these issues are related to the geometry of the fibres themselves. They are often quite fragile and their inclusion in a sensor head detracts from its robustness and also restricts the possibilities for miniaturisation. The necessity of maintaining effective light coupling to the fibre increases the level of complexity in the sensor head design, as any change in this greatly impairs the efficiency and stability of the device. It is possible to address this issue effectively in a laboratory environment. However, the development of a fibre-based sensor head for field use is far more problematic due to an inability to control the operational environment of the sensor and the resulting impact this could have on the precise alignment required to couple light efficiently to the fibre. The geometry of optical fibres does not lend itself readily to conventional micropatterning techniques, making the incorporation of integrated optical components or microsystems a complex and time consuming task. For sensing applications, the properties of the cladding are of vital importance as they determine the rate of diffusion of the analyte into the sensing layer, which has a direct impact on the response time of the sensor. This means that commercially available optical fibres cannot be tailored towards the detection of a particular analyte unless they are de-clad and coated with an analyte-specific sensing layer. This coating step is quite difficult to implement, mainly due to the geometry of optical fibres. For instance, it is not possible to use techniques such as spin-coating or knife-coating to deposit a uniform sensing layer onto an optical fibre. Dip-coating is the only viable method and requires larger volumes of material compared with those mentioned above.

In contrast, a planar waveguide does not suffer from these disadvantages. Its geometry is inherently more robust than that of an optical fibre and, as a result, such waveguides can be incorporated into the design of a compact sensor head, devoid of moving parts, with relative ease. A planar geometry is compatible with modern microfabrication techniques and facilitates the deposition of uniform sensing layers by a variety of methods including spin-coating and dip-coating. The versatility of this configuration makes it more attractive for the development of practical optical chemical sensors and, for this reason, planar waveguide-based platforms have formed the focus of the work reported here.

1.3.2 Planar waveguide based sensors

A typical thin film-based planar waveguide chemical sensor is depicted in Fig. 1.2.

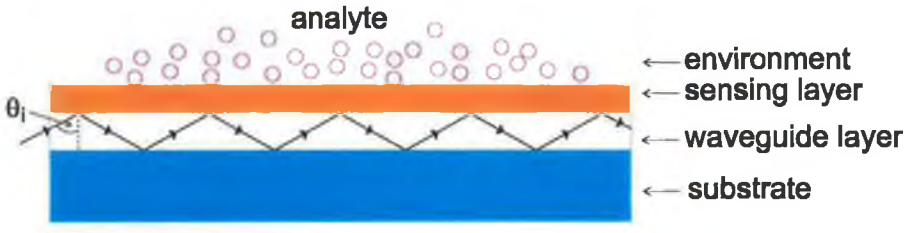

Figure 1.2: A typical thin film-based planar waveguide chemical sensor.

The device consists of a high refractive index thin film deposited on a lower index, planar substrate. An additional lower index superstrate layer, which acts as a sensing layer, is deposited on top of the high index film that acts as the waveguide. Light propagates by total internal reflection along the waveguide layer and the sensing layer is interrogated by the evanescent field of the propagating radiation (a more detailed theoretical description of the operation of these planar waveguides is given in Chapter 2). The use of the term "thin film" when referring to this waveguide configuration signifies the use of a waveguide layer typically less than 5μm in thickness. When employing visible light, this means that the waveguide would be single-mode or low-mode in nature. Such waveguides have restrictive coupling conditions that detract from the robustness of the platform. Furthermore, the low number of guided modes results in a low sensor signal level, which has a detrimental effect on the signal to noise ratio (SNR) of the device. Consequently, this work has concentrated solely on the use of highly multimode planar waveguides as optical sensor platforms due to the less restrictive coupling requirements and higher light levels associated with these platforms. Fig. 1.3 illustrates the typical configuration of such a platform.

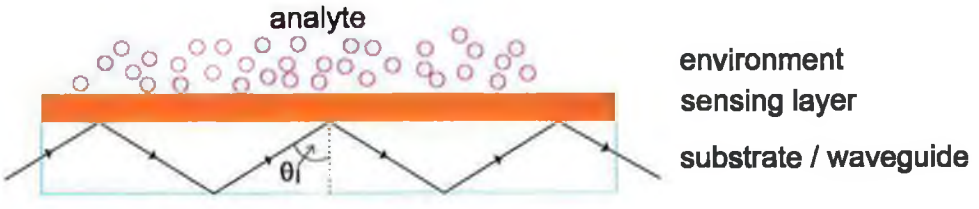

Figure 1.3: A multimode planar waveguide-based sensor.

The platform consists of a thick ($\approx$ 1mm) substrate, coated with a thin ($<$ 1μm) sensing layer. This sensing layer has a lower refractive index than the substrate, which acts as the multimode waveguide. The target analyte is present in the environment and is free to diffuse into the sensing layer. Light is coupled to the substrate / waveguide and interrogates the sensing layer to an extent dependent on the angle at which it is incident on the layer, θ_i. In a typical evanescent-wave-based multimode sensor platform, incident angles are greater than the critical angle determined by the refractive indices of the waveguide and sensing layer, θ_c. Alternative modes of interrogation are described in Chapter 2, and in particular, the effect of interrogating the sensing layer at different angles of incidence on platform sensitivity is examined in Chapter 5.

While planar waveguides typically suffer from higher propagation losses than optical fibres, their geometry and ease of fabrication makes them an ideal candidate for the fabrication of integrated optical microsystems. There are several methods commonly employed for the fabrication of planar waveguides including chemical vapour deposition (CVD) and potassium ion exchange (PIE). However, these processes are more suited to the fabrication of low-mode waveguides. In this work, both glass microscope slides and polymer platforms fulfilled the role of multimode waveguides, the latter being fabricated by micro-injection moulding (see Chapter 7, Sec. 7.1). The sensing layer that was deposited on these waveguides was most commonly sol-gel-based due to the versatile nature of sol-gel technology and the mechanical stability of such layers.

1.4 Sol-gel technology

The sol-gel process [18] is a technique for the production of glass and ceramic materials at low temperatures. It is achieved by the hydrolysis and condensation of metal alkoxide precursors using water, a solvent and a catalyst. This ultimately results in the formation of a viscous, porous gel which is then thermally cured to provide a hardened glass-like material. Prior to gel formation, the sol can be coated on a substrate as a thin film, then cured at a variety of temperatures depending on the intended application. Low temperatures ($<$ 100°C) result in a porous film suitable for use as a sensing membrane while high curing temperatures ($>$ 400°C) yield a densified film that can be used as a waveguide. In the case of

porous sol-gel thin films, it is possible during the preparation stage to incorporate an indicator compound which will become encapsulated in the cured, porous film making it accessible to the target analyte of choice, which is free to diffuse into the sol-gel layer. Refractive index modifiers can be included to ensure the refractive index of a densified sol-gel thin film is adequately high for waveguiding purposes and it is also possible to tailor the surface properties of a sol-gel film through correct choice of precursors.

One very important aspect of sol-gel technology is the mouldable nature of the liquid sol itself. This property of sol-gel materials make them an excellent choice for use in rapid prototyping techniques such as pin-printing [19], ink-jet printing [20] and soft lithographic micromoulding techniques, facilitating the production of low-cost, mass-producible optical microsystems. It is also possible to include UV-curable moieties into a sol-gel formulation so that it can be patterned in a manner similar to commercial negative-tone photoresists using an appropriate light source [21, 22].

1.5 Soft Lithography

Soft lithography is the name given to set of patterning techniques developed by George Whitesides and his team at Harvard University [23]. All techniques employ a rubber patterning element, the material of choice for this stamp being poly(dimethylsiloxane) (PDMS). This suite of techniques offers several advantages in the area of rapid prototyping and microfabrication, the majority of these advantages being directly linked to the versatile nature of the PDMS patterning element itself. PDMS is a cheap, non-toxic material available commercially as Sylgard 184 from Dow Corning. It is elastomeric and makes conformal contact with the surface to be patterned, facilitating the patterning of non-planar substrates. It is optically transparent and can also be used as a microfluidic material due to its ability to form a hermetic seal with a sufficiently smooth surface, thus rendering the microfluidic system optically addressable from outside.

There are several lithographic techniques encompassed by the term soft lithography and these will be explained in detail in Chapter 4, Sec. 4.1. One of the most important aspects of these techniques is the fabrication of the PDMS patterning element and it is this process which makes soft lithography such an attractive

candidate for rapid prototyping of microsystems. It is possible to fabricate a prototype element in approximately one hour, provided the desired master against which to cast the liquid prepolymer is available. Given the fact that it is frequently possible to fabricate the master using one of the rapid prototyping techniques described in Chapter 4, it is feasible to produce a prototype patterning element within 24 hours of design conception. The combination of soft lithography with rapid prototyping techniques provides a powerful tool for microsystems fabrication and, in this work, these techniques are applied to the production of optical sensor systems.

1.6 Polymer processing technology

Central to the fabrication of low-cost, mass-producible microsystems is the need for high throughput processing technologies that yield potentially disposable platforms. Semiconductor technology, whilst fulfilling the criterion of mass production capability, does not lend itself readily to the production of disposable microsystems as silicon and other semiconductor materials are quite expensive and unsuitable for many chemical sensing applications.

Polymer processing technology [24], on the other hand, provides a route for the fabrication of mass-producible, low-cost microsystems due to the nature of polymers themselves. There are many commercially available polymers providing a range of chemical and physical characteristics that can be used in high throughput polymer processing technologies such as injection moulding and compression moulding. These polymers are cheap, yet capable of fulfilling the physical and chemical requirements placed on them by the target application. The best known example of polymer processing technology is the CD which is fabricated by compression moulding. CD's are durable yet low-cost and provide a perfect example of high-quality, inexpensive polymer platforms.

A major objective of this work was the production of polymer sensor platforms capable of enhanced performance. Polymer technology is attractive, not only for the reasons mentioned above, but for its compatibility with rapid prototyping processes. These characteristics allow for the development of versatile design and fabrication protocols which can be implemented or modified in hours or days rather than weeks or months, as is sometimes the case for semiconductor

fabrication processes.

1.7 Current state of the art

1.7.1 Planar optical absorption-based sensing platforms

In recent years, efforts have been made by several groups to develop optical absorption-based sensors displaying enhanced sensitivity by employing new optical configurations. Suzuki *et al.* [25] reported the development of "active waveguides" which outperformed conventional evanescent-wave-based devices. Such devices employed prism couplers to inject light into a poly(vinylchloride) (PVC) thin film which fulfilled the role of both waveguide and sensing layer. This layer was doped with analyte sensitive indicators, e.g., calcium-selective and sodium-selective ionophores, and displayed sensitivity in the range of 10^{-4}M to 1M for Ca^{2+} and from 10^{-5}M to 10^{-2}M for Na^{+}. However, both sputtering and spin-coating techniques were employed to produce this device which made use of four different materials, i.e., three types of glass and the PVC layer. The relatively complex nature of this design along with the use of prism couplers renders this device impractical from the point of view of both mass production and field use. The "integrated waveguide absorbance optodes" (IWAO's) developed by Puyol *et al.* [26] employ input and output anti-resonant reflecting optical waveguide (ARROW) structures and a free propagation region between the two where the sensing membrane is placed. The membrane supports the guided mode from the input waveguide and this mode is then coupled to the larger output waveguide for detection. This device was applied to the detection of potassium ions (K^{+}) and was sensitive over the range 1M to 10^{-5}M. The fabrication of this device is again relatively complex, involving low-pressure chemical vapour deposition (LPCVD), plasma-enhanced chemical vapour deposition (PECVD), reactive ion etching (RIE) and spin-coating steps. A device displaying excellent sensitivity to gaseous ammonia was developed by Qi *et al.* [27]. It consisted of a potassium ion-exchanged (PIE) waveguide deposited on a glass substrate. A tapered film of Bromothymol Blue (a pH indicator dye) was deposited onto the PIE waveguide by vacuum evaporation and the two formed a composite optical waveguide (COWG). This device displayed a limit of detection (LOD) for gaseous ammonia of 1ppb,

outperforming any evanescent-wave-based devices developed to date. However, the film deposition process does not lend itself well to mass production and the use of prism couplers in the setup makes the device unsuitable for use outside a laboratory environment. Goddard *et al.* [28] have exploited polymer microfabrication techniques to produce leaky waveguide-based polystyrene sensor chips with integrated grating couplers. These platforms are quite versatile and can be applied to both absorption-based and fluorescence-based optical sensor platforms. Optical interrogation of the superstrate is provided by leaky light modes which propagate within this medium (see Chapter 2 for a description of such modes, also referred to as radiation modes). The use of grating couplers introduces an added technical challenge to the development of the sensor platform but this step also highlights the versatility of the fabrication protocol.

1.7.2 Microsystems and rapid prototyping technology

The development of microsystems for sensing applications is an area of intense research currently, especially when combined with the development of microfluidic systems (μFS). Polymer technology has been widely exploited to this end and among the most frequently employed materials for the fabrication of μFS is PDMS, which is also the material of choice for the soft lithographic techniques mentioned in Sec. 1.5. Whitesides *et al.* have developed several μFS based on PDMS. These have adopted various configurations including fluidic diffraction gratings [29], microfluidic networks with integrated optical excitation sources [30] and three-dimensional μFS [31]. Scherer *et al.* have also employed PDMS μFS in the development of integrated absorption and fluorescence microspectrometers [32]. Lee *et al.* [33] have demonstrated microlens arrays based on liquid-filled PDMS and Grover *et al.* have fabricated valves and pumps for μFS from PDMS [34] as have Quake *et al.* [35] and Berg *et al.* [36]. Beebe *et al.* have also carried out extensive work on the development of μFS including the fabrication of biomimetic hydrogel valves [37] and investigations of surface-directed liquid flow [38, 39]. Rapid prototyping methods for the production of polymer microsystems have been extensively investigated by Whitesides *et al.* [40, 41] and also by McCreedy [42]. These methods involve the production of a suitable photomask using a high resolution printer to print the design onto acetate [40] or onto

paper. In the latter case, a photographic reduction step is employed to produce the photomask [41, 42].

A variety of optical microsystems have been produced using soft lithographic techniques including microring optical resonators [43], polymer lasers [44], photonic crystal lasers [45], ridge waveguides [46, 47] and deformable diffraction gratings for pressure monitoring [5]. Other polymer processing technologies have also been applied to the development of micro-optical and microfluidic systems. These techniques are hot-embossing [48] and injection moulding [49]. The former was employed by MacCraith *et al.* in the development of a multianalyte florescence-based sensor chip [50], while the latter was used by Malins *et al.* in the production of polymer leaky waveguide devices for optical sensing [28]. Yet another polymer processing technique, that of laser micromachining, was employed by Bowden *et al.* for the fabrication of a microfluidic chip for phosphate sensing [51].

It should be noted that these examples are intended to serve as a cross-section of the various applications of polymer processing technology in microsystems development and optical sensing and, as such, should not be viewed as a comprehensive review of the field.

1.8 Thesis structure

Chapter 2 details waveguide theory as it relates to planar waveguide platforms and the following chapter contains a detailed description of the sol-gel technology used to produce the sensing layers that were deposited onto the planar waveguides. This description includes the various materials involved and their effect on the characteristics of the thin films fabricated by this route.

Chapter 4 details the rapid prototyping technologies that can be applied to the production of planar sensor platforms, in particular soft lithography and polymer processing technology.

Chapter 5 describes absorption-based optical chemical sensing and outlines some common configurations, concluding with a description of the enhancement strategy for such sensors formulated within the laboratory where this work was performed. The experimental verification of this strategy is discussed in Chapter 6 and applied to the production of a prototype, LED-based sensor, the performance of which was compared to current state of the art. Polymer processing technology

was exploited in the following stage of this work, described in Chapter 7, to fabricate enhanced polymer waveguide platforms that were designed in accordance with the enhancement strategy presented in the two previous chapters. Polymer platforms coated with sol-gel-derived sensing layers were applied to the detection of gaseous ammonia and similar (pH-sensitive) sensing layers were used in a second set of experiments intended to establish the dependence of sensitivity on platform interaction length.

Chapter 8 demonstrates the application of soft lithographic techniques to optical sensor and microsystems fabrication. In particular, soft lithography and high-resolution pin-printing were applied to the development of an integrated optical oxygen sensor based on the quenching of fluorescence from a sol-gel-encapsulated ruthenium complex.

Chapter 9 draws conclusions from the work reported here and highlights possible future applications.

1.9 Thesis objectives

The overall goal of this project was the development of enhanced platforms for optical chemical sensing applications. To this end, the following were the specific objectives:

1. Experimental verification of theoretical predictions related to the modal dependence of sensitivity for absorption-based optical chemical sensors.

2. Development of a prototype sensor platform, designed according to the dedicated enhancement strategy provided by theory. This device should demonstrate an enhanced performance compared to previously reported sensor platforms.

3. Extension of the enhancement strategy to the design and fabrication of mass-producible, enhanced polymer waveguide platforms and an examination of the effect of sample interaction length on device sensitivity.

4. Exploitation of soft lithographic techniques for the fabrication of optical microstructures with applications in optical sensing, including the development of an integrated optical sensor platform.

In general, it was intended that this work should highlight the capability of rapid prototyping technology in developing efficient sensor platforms when coupled with dedicated sensor enhancement strategies. This combination should prove viable as the basis for an effective rational design protocol for optical chemical sensors.

Bibliography

[1] M. J. O'Dwyer, G. M. Maistros, S. W. James, R. P. Tatam, and I. K. Partridge, "Relating the state of cure to the real-time internal strain development in a curing composite using in-fibre Bragg gratings and dielectric sensors," *Measurement Science and Technology*, vol. 9, no. 8, pp. 1153–1158, 1998.

[2] S. W. James, R. P. Tatam, S. R. Fuller, and C. Crompton, "Monitoring transient strains on a gun barrel using fibre Bragg grating sensors," *Measurement Science and Technology*, vol. 10, no. 2, pp. 63–67, 1999.

[3] S. W. James, M. L. Dockney, and R. P. Tatam, "Simultaneous independent temperature and strain measurement using in-fibre Bragg grating sensors," *Electronics Letters*, vol. 32, no. 12, pp. 1133–1134, 1996.

[4] C. C. Ye, S. W. James, and R. P. Tatam, "Simultaneous temperature and bend sensing with long-period fiber gratings," *Optics Letters*, vol. 25, no. 14, pp. 1007–1009, 2000.

[5] K. Hosokawa, K. Hanada, and R. Maeda, "A polydimethylsiloxane (PDMS) deformable diffraction grating for monitoring of local pressure in microfluidic devices," *Journal of Micromechanics and Microengineering*, vol. 12, no. 1, pp. 1–6, 2002.

[6] J. Hradil, C. Davis, K. Mongey, C. McDonagh, and B. D. MacCraith, "Temperature-corrected pressure-sensitive paint measurements using a single camera and a dual-lifetime approach," *Measurement Science and Technology*, vol. 13, no. 10, pp. 1552–1557, 2002.

[7] E. Rabinovich, M. J. O'Brien, S. R. J. Brueck, and G. P. Lopez, "Phase-sensitive multichannel detection system for chemical and biosensor arrays and fluorescence lifetime-based imaging," *Review of Scientific Instruments*, vol. 71, no. 2, pp. 522–529, 2000.

[8] B. MacCraith, G. O'Keeffe, A. McEvoy, C. McDonagh, and J. McGilp, "Development of a led-based phase fluorimetric oxygen sensor using evanescent

wave excitation of a sol-gel immobilized dye," *Sensors and Actuators B*, vol. 29, pp. 226–230, 1995.

[9] G. O'Keeffe, B. D. MacCraith, A. K. McEvoy, C. M. McDonagh, J. McGilp, B. O'Kelly, J. D. O'Mahony, and M. Cavanagh, "Light-emitting-diode-based oxygen sensing using evanescent wave excitation of a dye-doped sol-gel coating," *Optical Engineering*, vol. 33, no. 12, pp. 3861–3866, 1994.

[10] C. McDonagh, B. D. MacCraith, G. O'Keefe, T. Butler, B. O'Kelly, and J. McGilp, "Fibre optic chemical sensors based on evanescent wave interactions in sol-gel derived porous coatings," *Journal of Sol-Gel Science and Technology*, vol. 2, pp. 661–665, 1994.

[11] E. Scorsone, S. Christie, K. C. Persaud, P. Simon, and F. Kvasnik, "Fibre-optic evanescent sensing of gaseous ammonia with two forms of a new near-infrared dye in comparison to phenol red," *Sensors and Actuators B-Chemical*, vol. 90, no. 1-3, pp. 37–45, 2003.

[12] T. Butler, B. MacCraith, and C. McDonagh, "Development of an extended range fiber optic pH sensor using evanescent wave absorption of sol-gel entrapped pH indicators," in *Chemical, Biochemical, and Environmental Fiber Sensors VII* (A. V. Scheggi, ed.), vol. 2508, pp. 168–178, Proc. of SPIE, 1995.

[13] C. McDonagh, A. McEvoy, and B. MacCraith, "Dissolved oxygen sensor based on fluorescence quenching of oxygen-sensitive ruthenium complexes immobilized in sol-gel derived porous silica coatings," *The Analyst*, vol. 121, pp. 785–788, 1996.

[14] B. D. Gupta and N. K. Sharma, "Fabrication and characterization of u-shaped fiber-optic pH probes," *Sensors and Actuators B-Chemical*, vol. 82, no. 1, pp. 89–93, 2002.

[15] W. B. Lyons, H. Ewald, C. Flanagan, and E. Lewis, "A multi-point optical fibre sensor for condition monitoring in process water systems based on pattern recognition," *Measurement*, vol. 34, no. 4, pp. 301–312, 2003.

[16] S. M. Maughan, H. H. Kee, and T. P. Newson, "Simultaneous distributed fibre temperature and strain sensor using microwave coherent detection of spontaneous brillouin backscatter," *Measurement Science and Technology*, vol. 12, no. 7, pp. 834–842, 2001.

[17] L. J. Ritchie, C. P. Ferguson, C. Bessant, and S. Saini, "A ten channel fibre-optic device for distributed sensing of underground hydrocarbon leakage," *Journal of Environmental Monitoring*, vol. 2, no. 6, pp. 670–673, 2000.

[18] C. J. Brinker and G. W. Scherer, *Sol-Gel Science - The Physics and Chemistry of Sol-Gel Processing*. New York: Academic Press, 1990.

[19] E. J. Cho and F. V. Bright, "Integrated chemical sensor array platform based on a light emitting diode, xerogel-derived sensor elements, and high-speed pin printing," *Analytica Chimica Acta*, vol. 470, no. 1, pp. 101–110, 2002.

[20] A. Atkinson, J. Doorbar, A. Hudd, D. L. Segal, and P. J. White, "Continuous ink-jet printing using sol-gel "ceramic" inks," *Journal of Sol-Gel Science and Technology*, vol. 8, no. 1-3, pp. 1093–1097, 1997.

[21] P. Ayras, J. T. Rantala, S. Honkanen, S. B. Mendes, and N. Peyghambarian, "Diffraction gratings in sol-gel films by direct contact printing using a uv-mercury lamp," *Optics Communications*, vol. 162, no. 4-6, pp. 215–218, 1999.

[22] P. Etienne, P. Coudray, Y. Moreau, J. Porque, and S. Najafi, "Sol-gel channel waveguide on silicon: fast direct imprinting and low cost fabrication," *Optics Communications*, vol. 143, pp. 199–202, 1997.

[23] G. Whitesides and Y. Xia, "Soft lithography," *Angewandte Chemie International Edition*, vol. 37, pp. 550–575, 1998.

[24] H. Becker and C. Gartner, "Polymer microfabrication methods for microfluidic analytical applications," *Electrophoresis*, vol. 21, no. 1, pp. 12–26, 2000.

[25] H. Hisamoto, K.-H. Kim, Y. Manabe, K. Sasaki, H. Minamitani, and K. Suzuki, "Ion-sensitive and selective active waveguide optodes," *Analytica Chimica Acta*, vol. 342, no. 1, pp. 31–39, 1997.

[26] M. D. Valle, M. Puyol, I. Garces, F., Villuendas, C. Dominguez, and J. Alonso, "Integrated waveguide absorbance optode for chemical sensing," *Analytical Chemistry*, vol. 71, no. 22, pp. 5037–5044, 1999.

[27] Z. M. Qi, A. Yimit, K. Itoh, M. Murabayashi, N. Matsuda, A. Takatsu, and K. Kato, "Composite optical waveguide composed of a tapered film of bromothymol blue evaporated onto a potassium ion-exchanged waveguide and its application as a guided wave absorption-based ammonia-gas sensor," *Optics Letters*, vol. 26, no. 9, pp. 629–631, 2001.

[28] C. Malins, J. Hulme, P. R. Fielden, and N. J. Goddard, "Grating coupled leaky waveguide micro channel sensor chips for optical analysis," *Sensors and Actuators B: Chemical*, vol. 77, no. 3, pp. 671–678, 2001.

[29] O. J. A. Schueller, D. C. Duffy, J. A. Rogers, S. T. Brittain, and G. M. Whitesides, "Reconfigurable diffraction gratings based on elastomeric microfluidic devices," *Sensors and Actuators A-Physical*, vol. 78, no. 2-3, pp. 149–159, 1999.

[30] M. L. Chabinyc, D. T. Chiu, J. C. McDonald, A. D. Stroock, J. F. Christian, A. M. Karger, and G. M. Whitesides, "An integrated fluorescence detection system in poly(dimethylsiloxane) for microfluidic applications," *Analytical Chemistry*, vol. 73, no. 18, pp. 4491–4498, 2001.

[31] J. R. Anderson, D. T. Chiu, R. J. Jackman, O. Cherniavskaya, J. C. McDonald, H. K. Wu, S. H. Whitesides, and G. M. Whitesides, "Fabrication of topologically complex three-dimensional microfluidic systems in PDMS by rapid prototyping," *Analytical Chemistry*, vol. 72, no. 14, pp. 3158–3164, 2000.

[32] M. L. Adams, M. Enzelberger, S. Quake, and A. Scherer, "Microfluidic integration on detector arrays for absorption and fluorescence microspectrometers," *Sensors and Actuators a-Physical*, vol. 104, no. 1, pp. 25–31, 2003.

[33] N. Chronis, G. L. Liu, K. H. Jeong, and L. P. Lee, "Tunable liquid-filled microlens array integrated with microfluidic network," *Optics Express*, vol. 11, no. 19, pp. 2370–2378, 2003.

[34] W. H. Grover, A. M. Skelley, C. N. Liu, E. T. Lagally, and R. A. Mathies, "Monolithic membrane valves and diaphragm pumps for practical large-scale integration into glass microfluidic devices," *Sensors and Actuators B-Chemical*, vol. 89, no. 3, pp. 315–323, 2003.

[35] M. A. Unger, H. P. Chou, T. Thorsen, A. Scherer, and S. R. Quake, "Monolithic microfabricated valves and pumps by multilayer soft lithography," *Science*, vol. 288, no. 5463, pp. 113–116, 2000.

[36] J. M. Berg, R. Anderson, M. Anaya, B. Lahlouh, M. Holtz, and T. Dallas, "A two-stage discrete peristaltic micropump," *Sensors and Actuators a-Physical*, vol. 104, no. 1, pp. 6–10, 2003.

[37] Q. Yu, J. M. Bauer, J. S. Moore, and D. J. Beebe, "Responsive biomimetic hydrogel valve for microfluidics," *Applied Physics Letters*, vol. 78, no. 17, pp. 2589–2591, 2001.

[38] B. Zhao, J. S. Moore, and D. J. Beebe, "Principles of surface-directed liquid flow in microfluidic channels," *Analytical Chemistry*, vol. 74, no. 16, pp. 4259–4268, 2002.

[39] B. Zhao, J. S. Moore, and D. J. Beebe, "Surface-directed liquid flow inside microchannels," *Science*, vol. 291, no. 5506, pp. 1023–1026, 2001.

[40] D. C. Duffy, J. C. McDonald, O. J. A. Schueller, and G. M. Whitesides, "Rapid prototyping of microfluidic systems in poly(dimethylsiloxane)," *Analytical Chemistry*, vol. 70, no. 23, pp. 4974–4984, 1998.

[41] T. Deng, H. K. Wu, S. T. Brittain, and G. M. Whitesides, "Prototyping of masks, masters, and stamps/molds for soft lithography using an office printer and photographic reduction," *Analytical Chemistry*, vol. 72, no. 14, pp. 3176–3180, 2000.

[42] T. McCreedy, "Rapid prototyping of glass and PDMS microstructures for micro total analytical systems and micro chemical reactors by microfabrication in the general laboratory," *Analytica Chimica Acta*, vol. 427, no. 1, pp. 39–43, 2001.

[43] Y. Y. Huang, G. T. Paloczi, J. Scheuer, and A. Yariv, "Soft lithography replication of polymeric microring optical resonators," *Optics Express*, vol. 11, no. 20, pp. 2452–2458, 2003.

[44] J. R. Lawrence, G. A. Turnbull, and I. D. W. Samuel, "Polymer laser fabricated by a simple micromolding process," *Applied Physics Letters*, vol. 82, no. 23, pp. 4023–4025, 2003.

[45] O. J. A. Schueller, G. M. Whitesides, J. A. Rogers, M. Meier, and A. Dodabalapur, "Fabrication of photonic crystal lasers by nanomolding of solgel glasses," *Applied Optics*, vol. 38, no. 27, pp. 5799–5802, 1999.

[46] B. T. Lee, M. S. Kwon, J. B. Yoon, and S. Y. Shin, "Fabrication of polymeric large-core waveguides for optical interconnects using a rubber molding process," *IEEE Photonics Technology Letters*, vol. 12, no. 1, pp. 62–64, 2000.

[47] A. Stoddart, X.-M. Zhao, S. Smith, E. Kim, Y. Xia, M. Prentiss, and G. Whitesides, "Fabrication of single-mode polymeric waveguides using micromolding in capillaries," *Advanced Materials*, vol. 8, no. 5, pp. 420–424, 1996.

[48] H. Becker and U. Heim, "Hot embossing as a method for the fabrication of polymer high aspect ratio structures," *Sensors and Actuators a-Physical*, vol. 83, no. 1-3, pp. 130–135, 2000.

[49] H. Schift, C. David, M. Gabriel, J. Gobrecht, L. J. Heyderman, W. Kaiser, S. Koppel, and L. Scandella, "Nanoreplication in polymers using hot embossing and injection molding," *Microelectronic Engineering*, vol. 53, no. 1-4, pp. 171–174, 2000.

[50] C. Malins, M. Niggemann, and B. D. MacCraith, "Multi-analyte optical chemical sensor employing a plastic substrate," *Measurement Science and Technology*, vol. 11, no. 8, pp. 1105–1110, 2000.

[51] M. Bowden, O. Geschke, J. P. Kutter, and D. Diamond, "CO2 laser microfabrication of an integrated polymer microfluidic manifold for the determination of phosphorus," *Lab on a Chip*, vol. 3, no. 4, pp. 221–223, 2003.

Chapter 2

Waveguide Theory

2.1 Introduction

Planar waveguides form the basis of the majority of the optical sensor platforms developed in the work reported here. Such waveguides consist of a dielectric layer surrounded by media of a lower refractive index and are referred to as asymmetric slab waveguides. The term "asymmetric" refers to the fact that the refractive index of the substrate (the medium beneath the waveguide) differs from that of the superstrate (the medium above the waveguide) as is the case for the sensor platforms developed here. This chapter details waveguide theory as it pertains to such structures and the analysis is subsequently extended to a ridge waveguide structure, which forms the basis of the integrated oxygen sensor described in Chapter 8.

2.2 Asymmetric Slab Waveguide

It is possible to analyse the theory of asymmetric slab waveguides using two different approaches: ray optics and wave optics. The former provides a relatively simple physical description of propagation within a waveguide while the latter employs Maxwell's equations to yield a comprehensive description of the guidance conditions for waveguide modes [1, 2, 3, 4, 5]. Consequently, ray optics serves as an introduction to waveguide theory in this chapter, while wave optics is used to provide a rigorous physical analysis of the structures under consideration.

2.2.1 Ray Optics Approach

Fig. 2.1 depicts a generalised asymmetric slab waveguide of the type used during this work. The structure consists of a waveguide layer with refractive index, n_g and thickness, d, on top of which a cover layer (for example, a sensing layer) of refractive index, n_l is deposited. Beneath the waveguide is the substrate with refractive index, n_s, which is assumed to be infinite in extent. This layer was usually air in the work reported here.

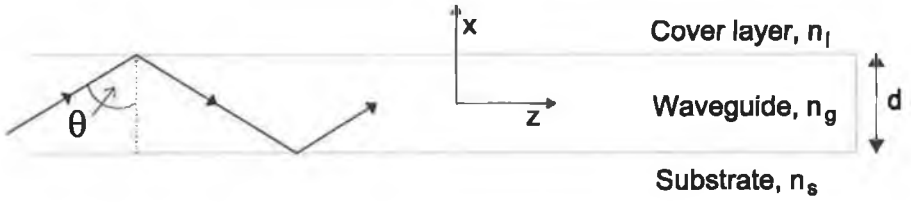

Figure 2.1: A typical asymmetric slab waveguide.

Fig. 2.1 illustrates a beam of light that is incident at an angle θ with respect to the surface normal. The critical angles at the two interfaces are defined as follows:

$$\theta_c^l = \sin^{-1}\left(\frac{n_l}{n_g}\right) \quad \text{Waveguide - cover interface} \tag{2.1}$$

$$\theta_c^s = \sin^{-1}\left(\frac{n_s}{n_g}\right) \quad \text{Waveguide - substrate interface} \tag{2.2}$$

For the work presented here, $n_s < n_l$, which means that $\theta_c^l > \theta_c^s$. Consequently, there are three possible angular ranges over which propagation can occur. These are:

1. $\theta_c^l < \theta < 90°$: This corresponds to the situation where light is totally internally reflected at both interfaces, resulting in a guided mode, as shown in Fig. 2.2.

2. $\theta_c^s < \theta < \theta_c^l$: In this regime of propagation, light undergoes total internal reflection at the waveguide-substrate interface but is free to escape through the cover layer (see Fig. 2.3). This is a cover radiation mode and it plays an

Figure 2.2: Guided mode, $\theta_c^l < \theta < 90°$.

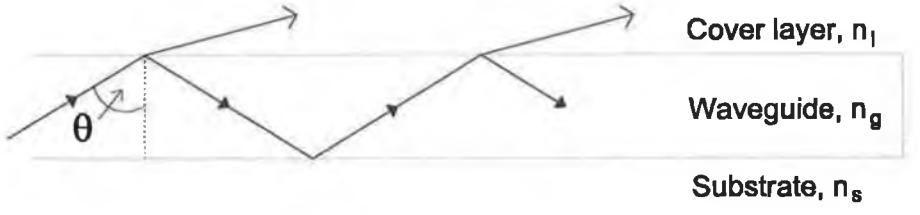

Figure 2.3: Cover radiation mode, $\theta_c^s < \theta < \theta_c^l$.

important role in the sensor enhancement strategy presented in Chapter 5, Sec. 5.3.1.

3. $\theta < \theta_c^s$: This situation is illustrated in Fig. 2.4. Light is free to escape into both the substrate and cover regions, resulting in a substrate-cover radiation mode.

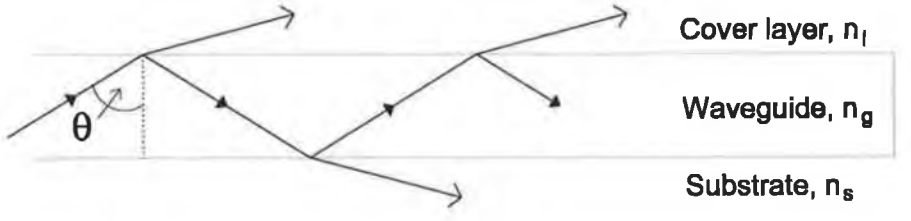

Figure 2.4: Substrate-cover radiation mode, $\theta < \theta_c^s$.

Clearly, ray optics offers a simple explanation of guided modes. However, the more rigorous analysis provided by wave optics is focused upon here.

2.2.2 Wave Optics Approach

Using the wave optics approach, a waveguide mode can be characterised by its effective index, n_{eff}. Fig. 2.5 is a wave-vector diagram that can be used to relate the propagation constants in the x and z directions to the angle of incidence, θ.

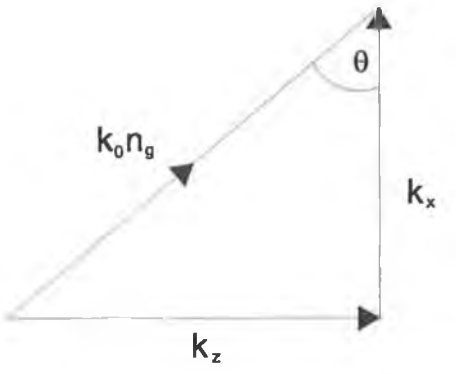

Figure 2.5: Wave-vector diagram

The propagation constant corresponding to a guided ray with incident angle, θ can be written as $k_0 n_g$, where $k_0 = 2\pi/\lambda$ and λ is the free space light wavelength. From Fig. 2.5, it follows that

$$k_x = k_0 n_g \cos\theta \tag{2.3}$$

and

$$k_z = k_0 n_g \sin\theta \tag{2.4}$$

The effective index, n_{eff} can be defined as

$$n_{\text{eff}} = n_g \sin\theta \tag{2.5}$$

Equation 2.5 provides a relationship between the ray optics approach to waveguide mode analysis, characterised by the incident angle θ and the wave optics approach, characterised by the effective index n_{eff}. Furthermore, the plane wave propagation constant along the z direction can now be defined as

$$k_z = k_0 n_{\text{eff}} \tag{2.6}$$

As stated in Sec. 2.2.1, the guiding condition is achieved for angles $\theta_c^l < \theta < 90°$. From equation 2.1, it is possible to write

$$n_g \sin\theta_c^l = n_l \tag{2.7}$$

Coupled with equation 2.5, this means that the propagation regime, $\theta_c^l < \theta < 90°$ corresponds to an effective index range of $n_l < n_{\text{eff}} < n_g$.

In order to establish the guidance conditions in an isotropic, lossless dielectric medium, the relevant Maxwell's equations must be employed. These are

$$\nabla \times \tilde{E} = -\mu_0 \frac{\partial \tilde{H}}{\partial t} \tag{2.8}$$

and

$$\nabla \times \tilde{H} = \epsilon_0 n^2 \frac{\partial \tilde{E}}{\partial t} \tag{2.9}$$

where ϵ_0 and μ_0 are the dielectric permittivity and magnetic permeability of free space, respectively and n is the refractive index. Assuming the plane wave propagates along the z direction with propagation constant k_z, the electromagnetic fields are of the form

$$\tilde{E} = E(x, y) \cdot \exp[j(\omega t - k_z z)] \tag{2.10}$$

$$\tilde{H} = H(x, y) \cdot \exp[j(\omega t - k_z z)] \tag{2.11}$$

where the angular frequency $\omega = 2\pi c/\lambda$ and c is the velocity of light in free space. The electromagnetic fields within the asymmetric slab waveguide are independent of y. Consequently, $\partial/\partial t = j\omega$, $\partial/\partial z = -jk_z$ and $\partial/\partial y = 0$, meaning that equations 2.8 and 2.9 yield two modes possessing polarisation states that are perpendicular both with respect to one another and to the direction of propagation of the electromagnetic wave. These modes are referred to as transverse electric (TE) and transverse magnetic (TM). Here, the propagation characteristics of only the TE waveguide modes will be described. However, TM modes may then be analysed with relative ease by employing duality [1]. The following analysis is taken from Ref. [1] and the complete treatment can be found in Appendix A.

The guidance condition for TE modes is given by

$$\nabla \times \tilde{E} = -\mu \frac{\partial \tilde{H}}{\partial t} = -\omega j \mu \tilde{H} \tag{2.12}$$

For a guided mode, it is assumed that the field is exponentially decaying in both the cover and substrate regions and that it is oscillatory in the waveguide region of thickness d, which leads to fields of the form

$$E_y(x,z) = \left\{ \begin{array}{l} E_l \exp[-\alpha_l x] \\ E_g \cos(k_x x + \psi) \\ E_s \exp[+\alpha_s x] \end{array} \right\} \exp[-jk_z z] \quad \begin{array}{l} \text{Cover} \\ \text{Waveguide} \\ \text{Substrate} \end{array} \tag{2.13}$$

where the transverse wavenumbers are defined by the appropriate dispersion relation in each region

$$\alpha_l = \sqrt{k_z^2 - \omega^2 \mu_l \epsilon_l} \tag{2.14}$$

$$\alpha_s = \sqrt{k_z^2 - \omega^2 \mu_s \epsilon_s} \tag{2.15}$$

$$k_x = \sqrt{\omega^2 \mu_g \epsilon_g - k_z^2} \tag{2.16}$$

and ψ is a phase term, representing the asymmetry of the structure. By exploiting the requirement of continuity of tangential E and H at both interfaces, i.e., at $x = \pm d/2$ and applying boundary conditions at these interfaces, it is possible to write

$$k_x d/2 + \psi = \tfrac{1}{2}\phi_l^{TE} \pm n\pi \tag{2.17}$$

$$k_x d/2 - \psi = \tfrac{1}{2}\phi_s^{TE} \pm m\pi \tag{2.18}$$

where

$$\phi_l^{TE} = \tan^{-1}\left(\frac{\mu_g \alpha_l}{\mu_l k_x}\right) \tag{2.19}$$

$$\phi_s^{TE} = \tan^{-1}\left(\frac{\mu_g \alpha_s}{\mu_s k_x}\right) \tag{2.20}$$

Adding equations 2.17 and 2.18 has the effect of eliminating ψ to produce the following relation

$$2k_x d - \phi_l^{TE} - \phi_s^{TE} = 2p\pi \qquad p = 0, 1, \ldots \tag{2.21}$$

Equation 2.21 is a generalised guiding condition for TE modes within an asymmetric slab waveguide. The next step in this analysis is to simplify this equation in order to obtain the specific characteristics of any guided mode.

This can be achieved by substituting for k_x, ϕ_l^{TE}, ϕ_s^{TE}, α_l and α_s from equations 2.14 – 2.16, 2.19 and 2.20 to obtain

$$d\sqrt{\omega^2\mu_g\epsilon_g - k_z^2} = p\pi + \tan^{-1}\left(\frac{\mu_g\sqrt{k_z^2-\omega^2\mu_l\epsilon_l}}{\mu_l\sqrt{\omega^2\mu_g\epsilon_g-k_z^2}}\right) + \tan^{-1}\left(\frac{\mu_g\sqrt{k_z^2-\omega^2\mu_s\epsilon_s}}{\mu_s\sqrt{\omega^2\mu_g\epsilon_g-k_z^2}}\right) \quad (2.22)$$

Knowing $k_z = \omega\sqrt{\mu\epsilon_{eff}}$ and making the reasonable assumption that all regions are magnetically equivalent results in a further simplification, which yields

$$d\omega\sqrt{\mu}\sqrt{\epsilon_g - \epsilon_{\text{eff}}} = p\pi + \tan^{-1}\left(\sqrt{\frac{\epsilon_{\text{eff}} - \epsilon_l}{\epsilon_g - \epsilon_{\text{eff}}}}\right) + \tan^{-1}\left(\sqrt{\frac{\epsilon_{\text{eff}} - \epsilon_s}{\epsilon_g - \epsilon_{\text{eff}}}}\right) \quad (2.23)$$

This relation can be rewritten as

$$\mathrm{V}\sqrt{1-b} = p\pi + \tan^{-1}\left(\sqrt{\frac{b+a^{TE}}{1-b}}\right) + \tan^{-1}\left(\sqrt{\frac{b}{1-b}}\right) \quad (2.24)$$

where b is the normalised waveguide index, a^{TE} is a measure of the asymmetry of the waveguide and V is a normalised frequency parameter that is a measure of the number of modes a waveguide may support (also known as the V number). These parameters are defined as follows

$$b = \frac{\epsilon_{\text{eff}} - \epsilon_s}{\epsilon_g - \epsilon_s} \quad (2.25)$$

$$a^{TE} = \frac{\epsilon_s - \epsilon_l}{\epsilon_g - \epsilon_s} \quad (2.26)$$

$$\mathrm{V} = k_0\, d\sqrt{(\epsilon_g - \epsilon_s)/\epsilon_0} \quad (2.27)$$

Equation 2.24 fully describes the guidance condition for TE modes within a planar waveguide and yields the dispersion plot shown in Fig. 2.6.

The plots shown are for the first three modes, $p = 0, 1, 2$, with six different asymmetry measures and it is clear that there exists, for each mode, a cut-off value of V beyond which the waveguide can no longer support the guided mode. This is referred to as the cut-off frequency for that particular mode, (V_m) and is defined in equation 2.28.

$$\mathrm{V}_m = \mathrm{V}_0 + m\pi \quad (2.28)$$

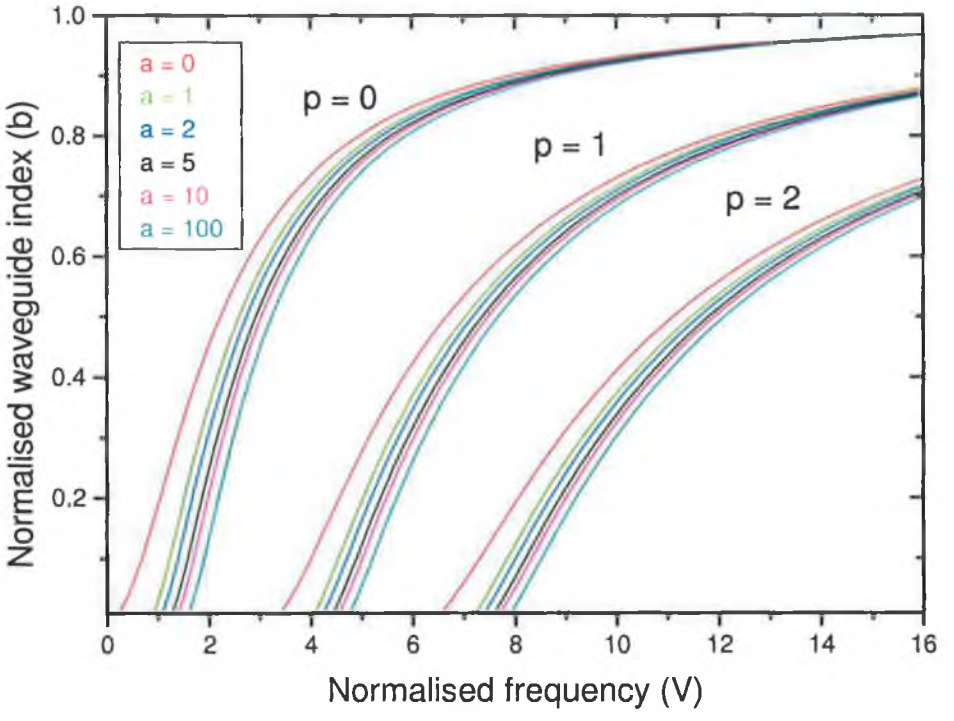

Figure 2.6: Dispersion curve for TE modes in an asymmetric slab waveguide

Here $V_0 = \tan^{-1}\sqrt{a^{TE}}$ corresponds to the cut-off value for the fundamental ($p = 0$) mode. This situation occurs as b approaches zero, i.e., as the effective index of the guided mode approaches the value of the substrate refractive index.

However, in the preceding analysis, b, a^{TE} and V were defined under the assumption that ϵ_{eff} was closer in value to ϵ_s than ϵ_l. In other words, it was assumed that $n_s > n_l$. This is *not* the case for the planar waveguide platforms examined during the course of this work. Instead, this refractive index relation is reversed as the substrate–or more accurately, the medium beneath the waveguide–was usually air and the cover consisted of a sol-gel-derived sensing layer. Intuitively, the guiding condition would not appear to be modified, as this reversal in the refractive index relation effectively inverts the slab waveguide structure and causes no modification of its guiding characteristics. To verify this, it is however necessary to redefine the aforementioned parameters, taking into account the fact that $n_s < n_l$ and that ϵ_{eff} is closer in value to ϵ_l than ϵ_s. Accordingly, the three parameters are redefined as follows

$$b = \frac{\epsilon_{\text{eff}} - \epsilon_l}{\epsilon_g - \epsilon_l} \tag{2.29}$$

$$a^{TE} = \frac{\epsilon_l - \epsilon_s}{\epsilon_g - \epsilon_l} \tag{2.30}$$

and

$$\mathrm{V} = k_0\, d\sqrt{(\epsilon_g - \epsilon_l)/\epsilon_0} \tag{2.31}$$

This step ensures that the cut-off condition is preserved (i.e., that it occurs as b approaches zero) and that the asymmetry measure remains positive. The effect of these changes on the guidance condition in (2.24) can be elucidated by evaluating $b/(1-b)$, $[(b + a^{TE})/(1-b)]$ and $\mathrm{V}\sqrt{1-b}$ in terms of ϵ_{eff}, ϵ_l, ϵ_g and ϵ_s. We find that

$$\frac{b}{1-b} = \frac{\epsilon_{\mathrm{eff}} - \epsilon_l}{\epsilon_g - \epsilon_{\mathrm{eff}}} \tag{2.32}$$

$$\frac{b + a^{TE}}{1-b} = \frac{\epsilon_{\mathrm{eff}} - \epsilon_s}{\epsilon_g - \epsilon_{\mathrm{eff}}} \tag{2.33}$$

$$\mathrm{V}\sqrt{1-b} = d\omega\sqrt{\mu}\sqrt{\epsilon_g - \epsilon_{\mathrm{eff}}} \tag{2.34}$$

Substituting equations 2.32–2.34 into equation 2.23 yields an equation identical to guidance condition (2.24), which proves that the two regimes, $n_s > n_l$ and $n_s < n_l$, are equivalent when considering guided mode propagation.

By numerically evaluating the guidance equation for a waveguide of known thickness and refractive index profile, it is possible to calculate a value for the normalised waveguide index, b. This may subsequently be used to calculate the modal refractive index from equation 2.25.

Evanescent field penetration depth

As mentioned in Chapter 1, a wide variety of optical sensor platforms employ evanescent-wave interrogation of the cover layer as the basis for sensing. Fig. 2.7 is a generalised depiction of mode propagation within a planar waveguide.

As the mode propagates within the waveguide by total internal reflection, its exponentially decaying evanescent tail extends into both cover and substrate layers. The extent to which the evanescent field penetrates the cover layer is of vital importance to the operation of evanescent-wave-based sensors, as it can, in general, be stated that the sensitivity of such platforms is directly proportional

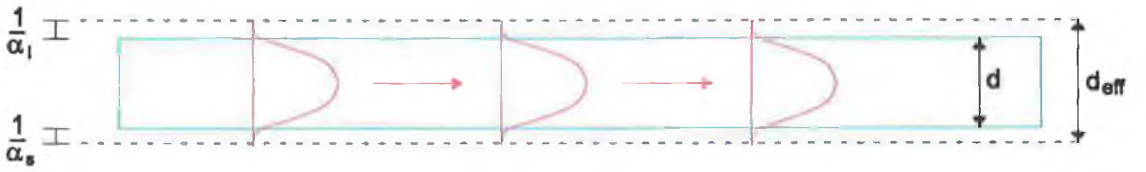

Figure 2.7: Mode propagation within a planar waveguide.

to the amount of power present within the sensing layer. The waveguide can be said to have an effective thickness

$$d_{\text{eff}} = d + \frac{1}{\alpha_l} + \frac{1}{\alpha_s} \tag{2.35}$$

where $1/\alpha_l$ and $1/\alpha_s$ correspond to the penetration depth of the evanescent field in the cover and substrate, respectively. It is clear from equations 2.14 and 2.15 that the penetration depth of a particular mode can, therefore, be calculated, once its effective index has been determined.

The quantities $1/\alpha_l$ and $1/\alpha_s$ can, alternatively, be explained in terms of a phenomenon known as the *Goos-Haenchen shift* [1]. This term refers to the fact that, as a guided mode undergoes total internal reflection at a dielectric interface, the reflected ray appears to be laterally shifted. Fig. 2.8 illustrates the propagation of a guided mode within a slab waveguide of thickness, d.

Figure 2.8: Origin of the Goos-Haenchen shift.

If, instead of being totally internally reflected at the physical waveguide boundary (i.e., $x = \pm d/2$), the mode is reflected at an imaginary boundary located at a distance, $1/\alpha$ from the physical boundary, this would explain the lateral shift in the reflected mode. In this case, $1/\alpha_l$ and $1/\alpha_s$ are the distances between the physical boundary and the imaginary Goos-Haenchen-related interface in the cover layer and substrate, respectively.

2.2.3 Radiation modes

The concept of radiation modes was introduced in Sec. 2.2.1, where it was shown that, for certain incident angles, light was free to escape to the cover medium or to both the cover and substrate media. In particular, the case of cover radiation modes was highlighted as being of interest for the sensitivity enhancement strategy presented in Chapter 5. Such modes are examined using a wave optics approach in this section. A complete analysis of the propagation conditions for cover radiation modes is beyond the scope of this work and this section serves merely to provide an intuitive understanding of the nature of such modes.

To recap, cover radiation modes are obtained for the range of incident angles, $\theta_c^s < \theta < \theta_c^l$ (recall that typically $n_l > n_s$ in the work reported here). This corresponds to a regime of propagation where light is totally internally reflected at the waveguide / substrate interface but is transmitted at the waveguide / cover interface. Consequently, we assume the propagating fields to be oscillatory in both the waveguide and cover regions and to be exponentially decaying in the substrate region. The fields can be written as follows

$$E_y(x,z) = \left\{ \begin{array}{l} E_l \sin[k_{lx}(x-d/2)-\psi_l] \\ E_g \cos(k_{gx}x-\psi) \\ E_s \exp[\alpha_s x] \end{array} \right\} \exp[-jk_z z] \qquad \begin{array}{l} \text{Cover} \\ \text{Waveguide} \\ \text{Substrate} \end{array} \qquad (2.36)$$

The subsequent analysis proceeds in a manner identical to that of guided modes. In order to establish the nature of the phase shift terms, ψ_l and ψ, the requirement of continuity of tangential components of the electromagnetic fields is utilised. The tangential component of $\tilde{H}$ is given by equation A.16 (see Appendix A), yielding

$$H_z(x,z) = \left\{ \begin{array}{l} \frac{jk_{lx}}{\omega\mu_l} E_l \cos[k_{lx}(x-d/2)-\psi_l] \\ -\frac{jk_{gx}}{\omega\mu_g} E_g \sin(k_{gx}x-\psi) \\ \frac{j\alpha_s}{\omega\mu_s} E_s \exp[\alpha_s x] \end{array} \right\} \exp[-jk_z z] \qquad \begin{array}{l} x > d/2 \\ |x| \leq d/2 \\ x < -d/2 \end{array} \qquad (2.37)$$

Matching boundary conditions at $x = d/2$ gives

$$E_{\tan}: \quad E_l \sin(-\psi_l) = E_g \cos(k_{gx} d/2 - \psi) \tag{2.38}$$

$$H_{\tan}: \quad E_l \cos(-\psi_l) = -\frac{\mu_l k_{gx}}{\mu_g k_{lx}} E_g \sin(k_{gx} d/2 - \psi) \tag{2.39}$$

Knowing $\sin(-A) = -\sin(A)$ and $\cos(-A) = cos(A)$ implies

$$E_{\tan}: \quad -E_l \sin(\psi_l) = E_g \cos(k_{gx} d/2 - \psi) \tag{2.40}$$

$$H_{\tan}: \quad E_l \cos(\psi_l) = -\frac{\mu_l k_{gx}}{\mu_g k_{lx}} E_g \sin(k_{gx} d/2 - \psi) \tag{2.41}$$

Taking the ratio of both equations leads to the following relation

$$\tan(\psi_l) = \frac{\mu_g k_{lx}}{\mu_l k_{gx}} \cot(k_{gx} d/2 - \psi) \tag{2.42}$$

In a similar fashion, applying boundary conditions at $x = -d/2$ yields

$$E_{\tan}: \quad E_s \exp[-\alpha_s d/2] = E_g \cos(k_{gx} d/2 + \psi) \tag{2.43}$$

$$H_{\tan}: \quad E_s \exp[-\alpha_s d/2] = -\frac{\mu_s k_{gx}}{\mu_g \alpha_s} E_g \sin(k_{gx} d/2 + \psi) \tag{2.44}$$

and again, taking the ratio of equations 2.43 and 2.44 gives us

$$\tan(k_{gx} d/2 + \psi) = \frac{\alpha_s \mu_g}{\mu_s k_{gx}} \tag{2.45}$$

The solutions to equations 2.42 and 2.45 can be shown to divide into two distinct sets. Specifically, for any solution with phase ψ, there exists a second having phase $\psi + \pi/2$, which correspond to "quasi-even" and "quasi-odd" modes, respectively [1]. A complete derivation of these modal solutions is beyond the scope of this work but, in brief, they can be described as those values required to fit an integral number of half-wavelengths between the upper boundary of the cover layer and the waveguide / substrate interface.

In Chapter 5, Sec. 5.3, a sensitivity enhancement strategy for absorption-based optical chemical sensors is presented. This strategy is based on an analysis of the sensitivity that is achievable by varying the mode of interrogation of the sensing layer. Maximum sensitivity is achieved for an incident angle, θ_{opt}, the value of which lies in the range, $\theta_c^s < \theta_{opt} < \theta_c^l$, which corresponds to a cover radiation mode.

2.3 Ridge Waveguide

A generalised schematic of a ridge waveguide is shown in Fig. 2.9. It consists of a strip of dielectric material with refractive index, n_g deposited on a substrate of lower refractive index, n_s and surrounded above and on both sides by a medium of yet lower refractive index, n_a (typically air).

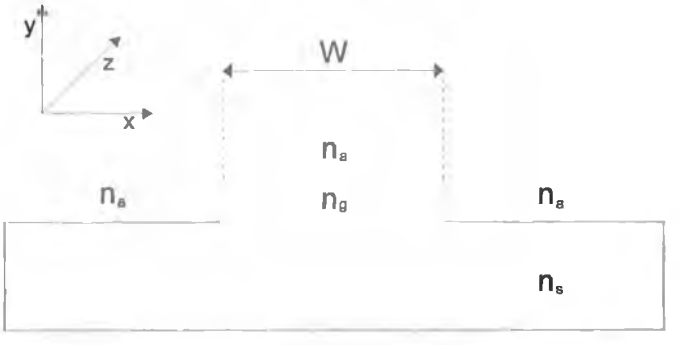

Figure 2.9: Schematic of a ridge waveguide structure.

Such a structure is referred to as a three-dimensional waveguide due to the fact that field variations in three directions must be considered when analysing its guiding properties. Guiding within a ridge waveguide is explained by transverse confinement of radiation in the x and y directions by total internal reflection at the $n_g - n_s$ and $n_g - n_a$ interfaces. This is represented schematically using a ray optics approach in Fig. 2.10.

Alternatively, propagation within such a structure can be analysed using the so-called effective index method. If the guide is viewed in the xz plane, it appears to be an asymmetric slab waveguide similar to the type discussed in Sec. 2.2.2. However, when viewed in the xy plane, it has the form of a symmetric slab waveguide. The subsequent analysis must therefore consider field variations in both x and y directions, as waveguiding occurs in these directions and is not independent of y as is the case for the asymmetric slab waveguide.

Assuming the width if the ridge waveguide (W) is very large, the guidance condition in the xz plane could be analysed as for an asymmetric slab waveguide structure consisting of a guiding region with high refractive index, n_g, deposited on a substrate of lower index, n_s with a cover layer of refractive index n_a above the guiding region. The propagation constants for the TE modes can be calculated from (2.24). Knowing values for ω, the waveguide dimensions and the various

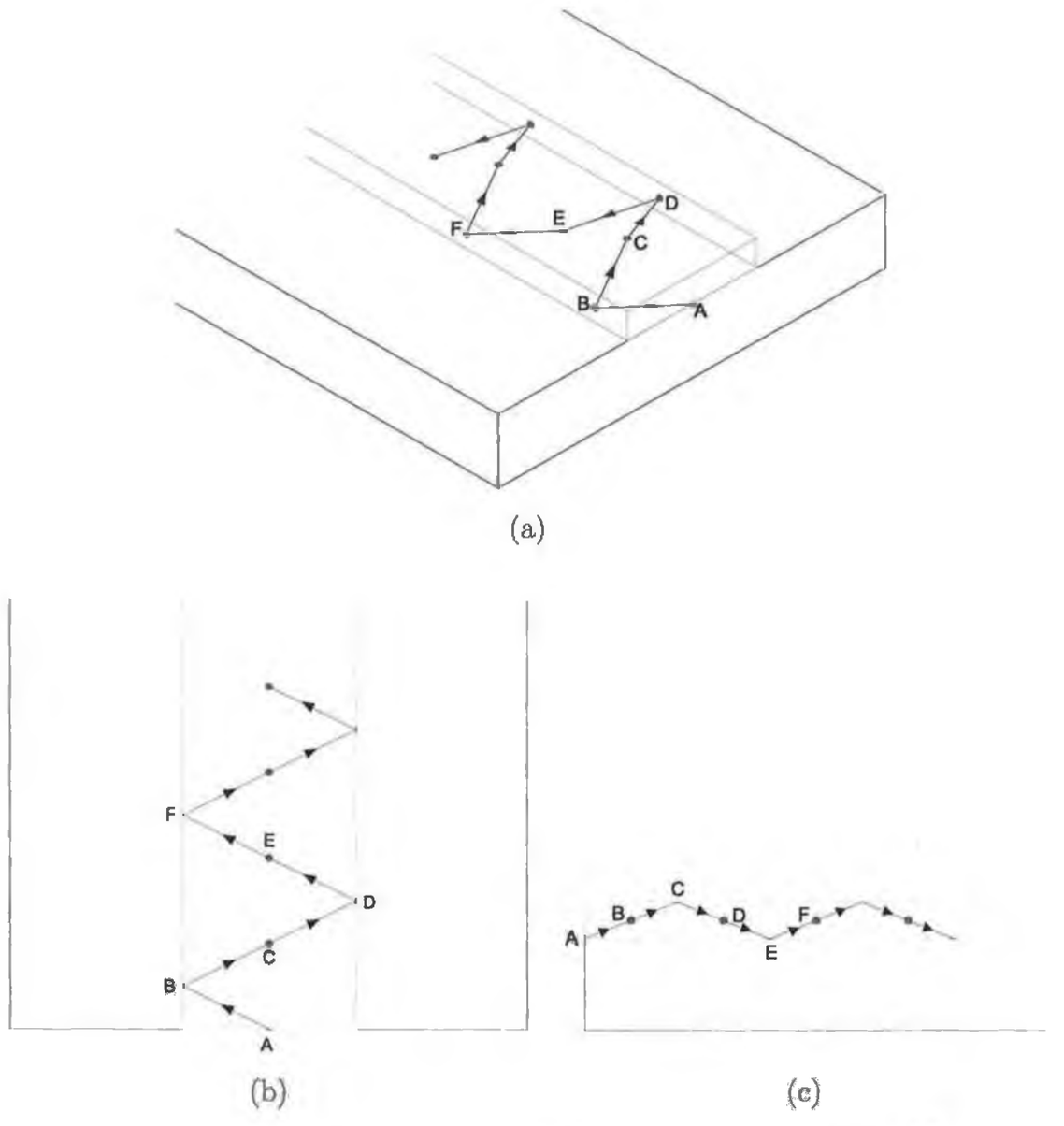

Figure 2.10: Light propagation within a ridge waveguide, adapted from [1].

permittivities, it is possible to obtain the V number and the asymmetry measure, a^{TE}, where the V number is defined as follows

$$\mathrm{V} = k_0\, d\sqrt{n_g^2 - n_s^2} \tag{2.46}$$

Note that $n_x = \sqrt{\epsilon_x/\epsilon_0}$, making equation 2.46 equivalent to equation 2.27. The parameter, b is defined for each mode, p as

$$b_p = \frac{(n_{\mathrm{eff}})_p^2 - n_s^2}{n_g^2 - n_s^2} \tag{2.47}$$

where $(n_{\mathrm{eff}})_p$ is the effective refractive index for each value of b_p. The propagation constant, $(k_z)_p$ is related to the effective index by equation 2.6, assuming W is infinite. The transverse wavenumbers in each region can again be obtained using the appropriate dispersion relationship, resulting in

$$(\alpha_a)_p = k_0\sqrt{(n_{\mathrm{eff}})_p^2 - n_a^2} \tag{2.48}$$

$$(k_x)_p = k_0\sqrt{n_g^2 - (n_{\mathrm{eff}})_p^2} \tag{2.49}$$

$$(\alpha_s)_p = k_0\sqrt{(n_{\mathrm{eff}})_p^2 - n_s^2} \tag{2.50}$$

It is clear that $(n_{\mathrm{eff}})_p$ contains all information regarding confinement in the xz plane. This term can now be used in the analysis of propagation in the yz plane by assuming the the symmetric slab waveguide (the structure presented by the ridge waveguide in this plane) consists of a central region of width, W with an effective permittivity, ϵ_{eff}, surrounded by a medium of permittivity, ϵ_a. A new parameter, V′ is defined as

$$\mathrm{V}' = k_0\,\mathrm{W}\sqrt{(n_{\mathrm{eff}})_p^2 - n_a^2} \tag{2.51}$$

A parameter $(b')_{pq}$ can be calculated from V′ using the normalised dispersion curve for TE modes

$$(b')_{pq} = \frac{(n'_{\mathrm{eff}})_{pq}^2 - n_a^2}{(n_{\mathrm{eff}})_p^2 - n_a^2} \tag{2.52}$$

It should be noted that, for each value of p (describing the modal variation in the xz plane), there are q solutions corresponding to modal variations in the yz plane, hence the need for these two subscripts when designating b' and n_{eff}. Using equations 2.47 and 2.52, the effective index can be written as

$$(n'_{\mathrm{eff}})_{pq} = \sqrt{n_a^2 + b_p(b')_{pq}(n_g^2 - n_s^2) + (b')_{pq}(n_s^2 - n_a^2)} \tag{2.53}$$

The associated propagation constant is $(k_z)_{pq}$, which is related to $(n'_{\text{eff}})_{pq}$ as shown in equation 2.6. The two transverse numbers in the y direction are α_y for $|y| >$ W/2 and k_y for $|y| <$ W/2. Using the appropriate dispersion relations, we have

$$(\alpha_y)_{pq} = k_0\sqrt{(n'_{\text{eff}})^2_{pq} - n_a^2} \tag{2.54}$$

$$(k_y)_{pq} = k_0\sqrt{(n_{\text{eff}})^2_{p} - (n'_{\text{eff}})^2_{pq}} \tag{2.55}$$

This technique accurately describes mode propagation when the mode is far from cut-off. If this is not the case, a computational solution is required.

2.4 Conclusions

Waveguide theory as it pertains to planar waveguide structures has been detailed in this chapter. In particular, the guidance conditions within an asymmetric slab waveguide were derived using a wave optics approach and the concept of evanescent field penetration depth was introduced. The nature of the propagation regime corresponding to cover radiation modes was also detailed, being of particular interest to the sensitivity enhancement strategy presented in Chapter 5. The analysis of guiding conditions was subsequently extended to a three-dimensional ridge waveguide structure using the effective index method, which provides an accurate description of propagating modes far from cut-off.

Bibliography

[1] D. L. Lee, *Electromagnetic Principles of Integrated Optics.* New York: John Wiley and Sons, 1986.

[2] A. W. Snyder and J. D. Love, *Optical Waveguide Theory.* London: Chapman and Hall, 1983.

[3] D. Marcuse, *Theory of Dielectric Optical Waveguides.* New York: Academic Press, 1974.

[4] T. Tamir, *Guided-Wave Optoelectronics, Second Edition.* New York: Springer-Verlag, 1990.

[5] C. Vassallo, *Optical Waveguide Concepts.* Amsterdam: Elsevier, 1991.

Chapter 3

The Sol-Gel Process

3.1 Introduction

The sol-gel process was first reported by Ebelman in 1846 [1] and is a material fabrication methodology that facilitates the production of high quality glasses and ceramics using metal alkoxide precursors [2]. These precursors undergo hydrolysis and condensation polymerisation reactions to form solid structures with characteristics that are determined by the conditions under which these reactions occur.

One of the most significant aspects of the sol-gel process is the low temperature range necessary for its completion. Temperatures are typically an order of magnitude lower than those required for conventional glass and ceramic fabrication techniques, which permits the incorporation of functional materials — that would otherwise be destroyed — into the finished structures. It will be shown that this characteristic of the sol-gel process is central to its success in the development of optical chemical sensors.

Another important advantage associated with the use of sol-gel materials is the mouldable nature of the liquid sol itself. This quality makes it possible to fabricate micropatterned optical structures in a single step using an appropriate lithographic method. In particular, soft lithographic techniques have been used in conjunction with sol-gel materials to fabricate a variety of optical structures with applications in sensing (see Chapter 8).

This chapter describes the various parameters associated with the sol-gel pro-

cess along with their effect on the characteristics of the sol-gel structure. It will also be shown that there are several methods in which the sol-gel process can be modified to produce materials with altered physical characteristics such as photosensitivity, modified refractive index and surface wettability. The encapsulation of analyte-sensitive, chemical reagents within the sol-gel matrix is also described, a step that is central to the development of the optical chemical sensors reported here. Finally, the thin film deposition techniques of dip-coating and spin-coating are outlined.

3.2 Fundamentals of the sol-gel process

Before explaining the process itself, it is instructive to define the nature of a sol-gel material. A sol is a colloidal suspension of solid particles in a liquid, with colloids being defined as solid particles with diameters of 1-100 nm. A gel is an interconnected, rigid network with pores of submicron dimensions and polymeric chains whose average length is greater than one micron. A typical sol-gel process employs a metal alkoxide precursor, a solvent, water and a catalyst to yield these materials. This is achieved by the simultaneous hydrolysis and polycondensation of the metal alkoxide precursor in the presence of the other ingredients. The most commonly employed sol-gel precursor in the work reported here was tetraethoxysilane (TEOS), a silicon alkoxide, where the central silicon atom is surrounded by four ethoxy groups. A second, commonly used precursor was methyltriethoxysilane (MTEOS), an organoalkoxysilane compound, which again consists of a central metal ion surrounded by ligands, one or more of which is organic.

A sol-gel material is fabricated by mixing the aforementioned ingredients together thoroughly and allowing hydrolysis and condensation to occur. This results in the formation of an interconnected solid network with low density known as a gel. This gel can then be subjected to a temperature programme which controls the densification process, thereby determining the physical characteristics of the end product. It is the intended application that dictates the curing regime to be employed, e.g., a low curing temperature ($< 100°C$) would be employed to produce the porous materials required to act as sensing layers. In order to produce the sol-gel-derived thin films used in the work reported here, the gel was

deposited on the desired substrate by dip-coating or spin-coating prior to curing.

3.2.1 Hydrolysis and condensation

The first stage in the formation of a typical sol-gel is hydrolysis, which is decribed in equation 3.1. This reaction replaces alkoxide groups, OR, with hydroxyl groups, OH, by the nucleophilic attack on silicon atoms by oxygen [2]. Here, R represents an alkyl group, C_xH_{2x+1}.

$$\equiv \mathrm{Si} - \mathrm{OR} + \mathrm{H_2O} \Leftrightarrow \equiv \mathrm{Si} - \mathrm{OH} + \mathrm{ROH} \tag{3.1}$$

$$\equiv \mathrm{Si} - \mathrm{OR} + \mathrm{HO} - \mathrm{Si} \equiv \Leftrightarrow \equiv \mathrm{Si} - \mathrm{O} - \mathrm{Si} \equiv + \mathrm{ROH} \tag{3.2}$$

$$\equiv \mathrm{Si} - \mathrm{OH} + \mathrm{HO} - \mathrm{Si} \equiv \Leftrightarrow \equiv \mathrm{Si} - \mathrm{O} - \mathrm{Si} \equiv + \mathrm{H_2O} \tag{3.3}$$

The condensation reactions shown in equations 3.2 and 3.3 occur via a nucleophilic condensation reaction and produce siloxane bonds, $\equiv \mathrm{Si} - \mathrm{O} - \mathrm{Si} \equiv$, together with the by-products alcohol or water. Usually condensation starts before hydrolysis is complete. Because water and alkoxysilanes are immiscible, a mutual solvent such as alcohol is used as a homogenising agent. It is important to note that the alcohol can also participate in the reverse reactions shown in equations 3.1 and 3.2. The water and alcohol condensation reactions proceed to build polymeric chains of $\equiv \mathrm{Si} - \mathrm{O} - \mathrm{Si} \equiv$ molecules, which interlink and form a three-dimensional network or gel. The physical characteristics of the gel are dictated by the hydrolysis and condensation rates, which are in turn dependent on a number of parameters. These are described in Sec. 3.3. The sol is said to have gelled when it can support a stress elastically. The time taken to reach this stage is known as the gelation time, t_g.

3.2.2 Aging and drying

Aging is the term used to describe the process that occurs after the ingredients have been mixed together to form a sol and prior to the film deposition stage. During this process, the sol is stored at either ambient or elevated temperatures

and the hydrolysis and condensation reactions continue (at an accelerated pace in the case of elevated temperatures). This increases the connectivity, hence the viscosity, of the gel, which is necessary when using the method of dip-coating for thin film deposition.

Drying is the removal of liquid from the interconnected pore network. The drying process may be divided into three distinct stages [3, 4]. The first stage is known as the constant rate drying period due to the fact that the evaporation rate per unit area is time-independent. It consists of a decrease in the volume of the gel, which is equal to the volume of the liquid lost by evaporation. The compliant gel network is deformed by the large capillary forces which cause the structure to shrink. The transition from stage one to stage two occurs when the "critical point" is reached. This is the point at which the strength of the network has increased due to the greater packing density of the solid phase, creating the highest capillary pressure. Unable to compress the gel any further, the pores begin to empty. This is termed "the first falling rate period" due to the decreased evaporation rate. The third stage of drying is reached when the pores have substantially emptied. During this stage, referred to as " the second falling rate period", there are no further dimensional changes. Instead, there is a slow progressive loss of weight until equilibrium is reached, a point that is determined by the ambient temperature and partial pressure of water.

3.3 Factors affecting the sol-gel process

3.3.1 Influence of water to precursor ratio (R value)

The R value of a sol is the molar ratio of water to silicon alkoxide precursor and it plays a significant role in the structural evolution of the sol-gel material. Both the size of the sol-gel particles and the amount of cross-linking within the sol-gel material are dependent on the R value. Theoretically, an R value of 2 is sufficient for complete hydrolysis and condensation to yield anhydrous silica as shown by the net reaction described in equation 3.4.

$$\mathrm{nSi(OR)_4 + 2nH_2O \rightarrow nSiO_2 + 4nROH} \tag{3.4}$$

However, this value has been shown to be insufficient for complete hydrolysis and condensation to occur. This is due to reverse reactions and the formation of intermediate species. Consequently, a R value greater than 2 is most commonly employed in the production of a sol in order to ensure completion of the hydrolysis and condensation reactions. Increasing the R value of the sol serves to promote hydrolysis, which in turn leads to a decrease in gel time. However, as the R value is further increased, the sol becomes more dilute, which increases the gel time due to the decrease in relative silica content. This relationship is illustrated in Fig. 3.1. From the graph, it is clear that gel time displays an initial decrease

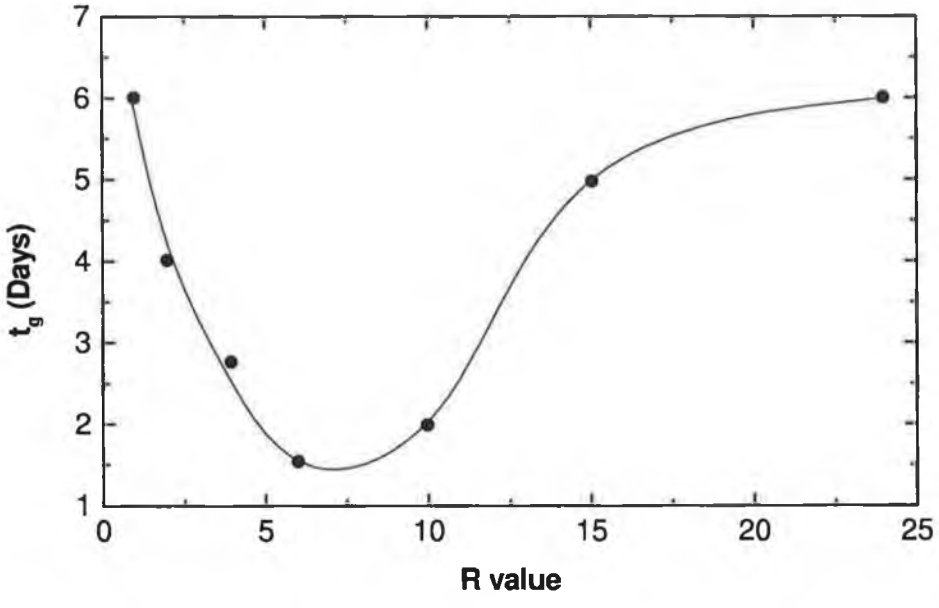

Figure 3.1: Variation of sol gelation time with R value [2].

with increasing R value until a minimum is reached and that, from this point on, gel time increases with increasing R value. The position of the minimum in this curve is dependent on the experimental conditions under which the sol is prepared, in particular the pH of the reaction.

3.3.2 Influence of sol pH

The pH value of a sol is dictated by the catalyst employed during its preparation. This value is an important parameter, as it determines the nature of the catalysis itself. Silica has its isoelectric point at a pH value of approximately 2. This point

corresponds to the situation where the electron mobility and surface charge of the silica are zero. Consequently, a sol of pH < 2 is said to be acid-catalysed, while those with pH values greater than 2 are base-catalysed. The characteristics of acid catalysis are fast hydrolysis and relatively long gel times, resulting in fine network structures of linear chains with pore sizes < 2nm. Conversely, base catalysis yields slow hydrolysis along with reduced gel times due to the increased condensation rates [2]. Such conditions result in the formation of more dense colloidal particles with larger interstices (pores). Fig. 3.2 illustrates the pH-dependence of gel time.

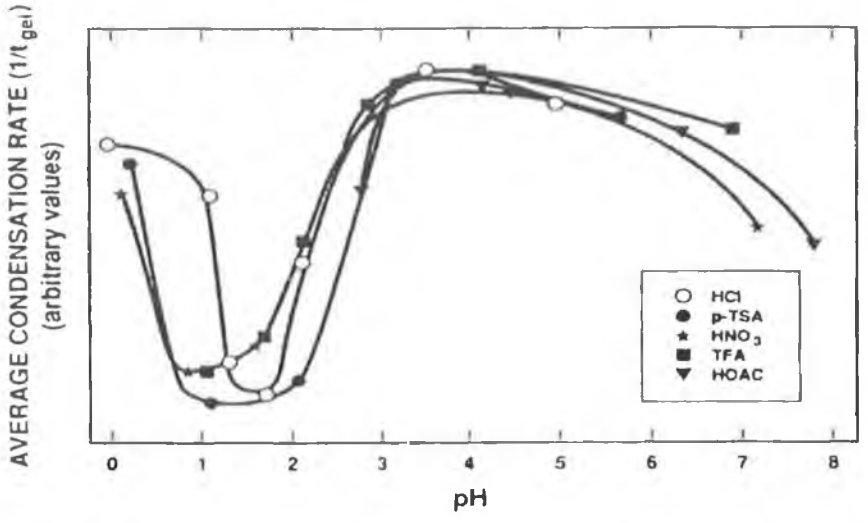

Figure 3.2: Average condensation rates (1/gel time) for TEOS hydrolysed with solutions of various acids [2]

The gel time is equal to 1/(average condensation rate). It can be seen from this plot that the overall condensation rate is minimised between pH values 1.5-2 and maximised at a pH value of approximately 4.

3.4 Ormosils

Standard alkoxide precursors such as TEOS yield sol-gel surfaces that are covered with hydroxyl groups. These surfaces are hydrophilic in nature and allow the adsorption of water molecules. However, for certain applications it is desirable that the film be hydrophobic, which necessitates the removal of hydroxyl groups from the surface. In the case of sol-gel thin films, chemical modification of the sol

is most commonly employed to achieve this effect. This route involves the use of precursors known as ORMOSILs (ORganically MOdified SILicates), which have one or more organic ligands replacing the ethoxy groups surrounding the central metal ion. Use of such precursors results in the replacement of surface hydroxyls with alkyl groups, giving rise to a hydrophobic surface. A typical example of an organically modified silicon alkoxide precursor is methyltriethoxysilane (MTEOS, $CH_3(C_2H_5O)_3Si$), in which a methyl group replaces one of the ethoxy groups. This methyl group is bonded to the silicon atom through a non-hydrolysable covalent bond and renders the resultant sol-gel film surface hydrophobic.

There are further advantages associated with the use of ORMOSILs compared with standard inorganic precursors. Leaching of entrapped dye compounds from sol-gel films has been shown to diminish significantly when using ORMOSIL-based thin films [5, 6] and film thicknesses of up to 6μm are achievable with little or no cracking [7]. This is approximately 10 times thicker than the maximum achievable thickness for TEOS-derived thin films but this value varies with the particular ORMOSIL used. It is also possible to prepare hybrid organic / inorganic sol-gels, which often offer advantages associated with both types of precursor. This lends a high degree of flexibility to the sol-gel process and was employed during the development of both the optical ammonia sensor and optical pH sensor described in Chapter 7.

3.5 Encapsulation of molecules within the sol-gel matrix

As mentioned in Sec. 3.1, the sol-gel process does not require high temperatures to go to completion. This permits the inclusion of compounds that would not survive high temperatures into the sol-gel matrix, thereby facilitating the encapsulation of analyte-sensitive reagents within the porous matrix by adding such reagents to the sol during the preparation stage. These reagents are most commonly fluorescent dyes or colorimetric indicator dyes. The encapsulated dye molecules are surrounded by the cage-like sol-gel network but the target analyte is free to diffuse through the pores of the sol-gel matrix and interact with the dye. It is also important to note that the sol-gel matrix is optically transparent, facil-

itating the optical excitation / interrogation of the encapsulated reagent. These characteristics form the basis of sol-gel-based optical sensors for a large variety of analytes including oxygen [8, 9, 10], carbon dioxide [11, 12, 13], ammonia [14], pH [15, 5, 16], and water vapour [17].

One possible issue associated with reagent encapsulation within sol-gel matrices is the ease with which polar organic reagents may be incorporated. This is a relatively simple process in the case of hydrophilic sol-gels such as TEOS. However, encapsulation of these compounds within less polar, ORMOSIL-derived sol-gels is hampered by the reduced solubility of the dye in such environments. This issue can be resolved by employing the technique of ion-pairing [18, 19, 13], which involves the use of a phase transfer reagent to render the dye soluble in the less polar environment, facilitating its encapsulation within the ORMOSIL-derived matrix.

Alternative methods for the inclusion of analyte-sensitive reagents into sensing membranes include post-doping and impregnation. However, these methods result in a weak attachment between the reagent molecules and the sensing matrix, reducing their shelf-life and making them unsuitable for use in environments where leaching is a potential issue. Encapsulation within a suitable sol-gel matrix successfully addresses these issues and provides a robust support for the desired sensing mechanism to occur.

3.6 Refractive index modification

For the purposes of optical sensing using sol-gel-derived planar waveguides, it is necessary that the sol-gel layer have a higher refractive index than the substrate on which it is deposited in order for total internal reflection to occur (i.e., for the sol-gel layer to function as a waveguide). This is equally true in the case of ridge waveguide structures. However, a completely densified silica thin film (as may be produced by high temperature annealing of a TEOS-derived sol-gel layer) has a refractive index of 1.46. This value is lower than that of most glasses or polymers, meaning that such a layer could not fulfill the role of waveguide when deposited on these substrates. It is, therefore, necessary to increase the refractive index of the sol-gel layer in order to achieve the conditions necessary for waveguiding.

The most commonly employed refractive index modification process is the inclusion of different, higher index, metal alkoxide precursors into the sol. Examples of such precursors include titania (TiO_2) and zirconia (ZrO_2). Titania has been incorporated into ORMOSIL-based sols for the fabrication of planar waveguides for optical sensing [20, 21], while zirconia was used during the fabrication of the integrated optical oxygen sensor presented in Chapter 8, Sec. 8.5. An important aspect of this process is the need to ensure homogeneous materials, a task which is made more difficult by the large difference in hydrolysis rates between the titania / zirconia and silica precursors. This issue can be addressed in the case of titania by ensuring anhydrous preparation conditions through the use of a catalyst such as silicon tetrachloride ($SiCl_4$) instead of aqueous hydrochloric acid (HCl). The method employed when using zirconia involves the use of a complexing agent to ensure comparable rates of hydrolysis, resulting in homogeneous materials (see Sec. 8.5). The amount of refractive index modifier dictates the final refractive index of the sol-gel layer, making it possible to tune the refractive index of the film to particular applications.

3.7 Photocurable sol-gels

Extensive work has been carried out in recent years on the use of photosensitive sol-gel materials for the fabrication of integrated optical components [22, 23, 24, 25]. These materials behave in a manner similar to commercial, negative-tone photoresists when exposed to light of the required wavelength, typically in the near ultra-violet range. Exposure causes polymerisation of photosensitive moieties within the matrix, causing densification of the material in these areas. In such a way, sol-gel films may be patterned by selectively exposing particular areas to UV light, typically through the use of a specially designed photomask. Those areas not exposed are subsequently removed during the development stage using a suitable solvent, leaving discrete structures on the substrate.

Photocurable sol-gel is used to fabricate the ridge waveguide structures described in Chapter 8. The sol is typically prepared by mixing a silicon alkoxide precursor (TEOS) with a second precursor containing an acrylate moiety and performing acid-catalysis of the two in the presence of water. Photoinitiator is then added to the sol in order to render the sol photosensitive. To produce sol-gel ma-

terials of sufficiently high refractive index to act as waveguides, a refractive index modifier complexed with methacrylic acid was added to the sol. The role of the complexing agent was described in the previous section. A complete description of the waveguide fabrication process is given in Sec. 8.4.

3.8 Dip-coating

Dip-coating is a simple way of depositing a sol onto a planar substrate, e.g., a glass microscope slide. The apparatus used in the work reported here consisted of a stationary sample holder positioned above a motorised, mobile platform carrying the coating solution. This platform was computer-controlled and could be translated vertically with precise velocity control, causing the sample to be immersed and withdrawn from the coating solution with a high degree of reproducibility.

The dip-coating process can be divided into five stages [2], namely immersion, start-up, deposition, drainage and evaporation (see Fig. 3.3). The first three are necessarily sequential, the third and fourth proceed simultaneously and the fifth, evaporation of solvent from the liquid, proceeds throughout the process.

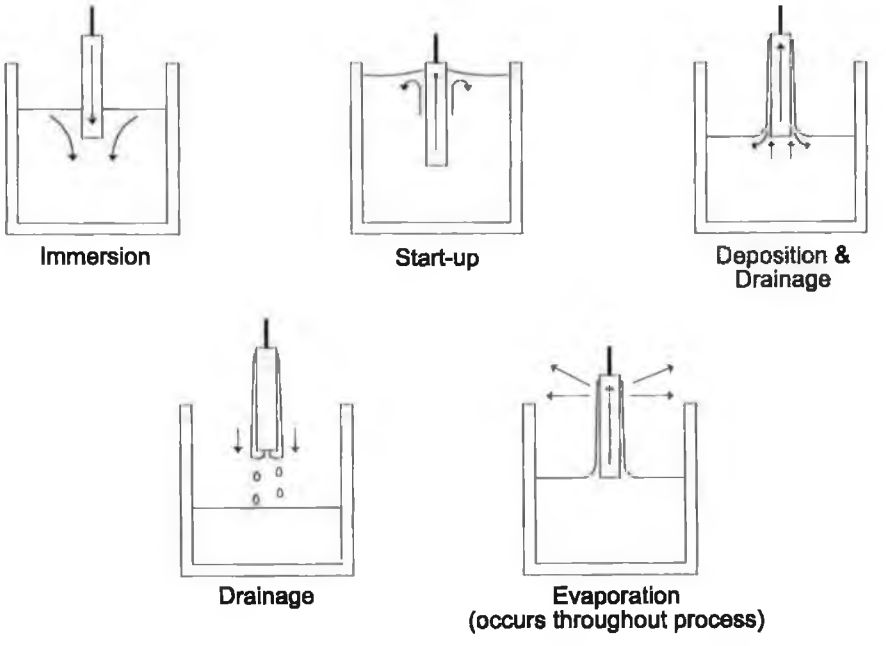

Figure 3.3: Stages in the dip coating process [2].

As the sample is immersed in the liquid and withdrawn, the inner layer of

deposited liquid moves in tandem with the substrate while the outer layer returns to the container. The film thickness is related to the position of the dividing border between the upward and the downward moving layers and is determined by a number of competing forces. These are:

1. Viscous drag upward on the solution due to the relative movement of the substrate and solution
2. Force of gravity
3. Resultant force of surface tension in the concavely-shaped meniscus
4. Inertial force of the boundary layer liquid arriving at the deposition region
5. Surface tension gradient
6. The disjoining or conjoining pressure.

Equation 3.5 describes the relationship between film thickness and dip speed.

$$t = 0.944(N_{\text{ca}})^{1/6} \left(\frac{\eta U}{\rho g}\right)^{1/2} \tag{3.5}$$

where t is the thickness, U is the dip speed, η is the liquid viscosity, g is acceleration due to gravity, N_{ca} is the capillary number ($N_{\text{ca}} = (\eta U)/\sigma$, where σ is the surface tension) and ρ is the density of the liquid. However, due to uncertainties in the value of the surface tension and the constantly evolving properties of sols, this equation is of limited use in predicting the thickness of a sol-gel thin film and thickness calibration is typically required from sol to sol and from one day to the next. For a given, unchanging set of values for solution viscosity and density, however, it is clear that film thickness increases with dip speed.

3.9 Spin-coating

The alternative film deposition process of spin-coating has been employed extensively throughout this work both for the fabrication of SU-8 templates on silicon wafers and the deposition of uniform sensing layers on the enhanced polymer waveguide platforms described in Chapter 7. Fig. 3.4 illustrates the typical spin-coating process. The substrate is held on a horizontal vacuum chuck and the

material to be deposited is dispensed on the centre of the substrate. The chuck is then programmed to rotate at a predefined acceleration, causing the material to spread over the surface of the substrate due to centrifugal force, until the final spin speed is reached. The chuck continues to rotate, resulting in the drainage of excess coating material from the sample and leaving a uniform film on the substrate. This technique offers several advantages over dip-coating including the ability to deposit films on a single side of a substrate without the need for masking, its compatibility with materials of a broader range of viscosities and, perhaps most importantly, improved film uniformity [26].

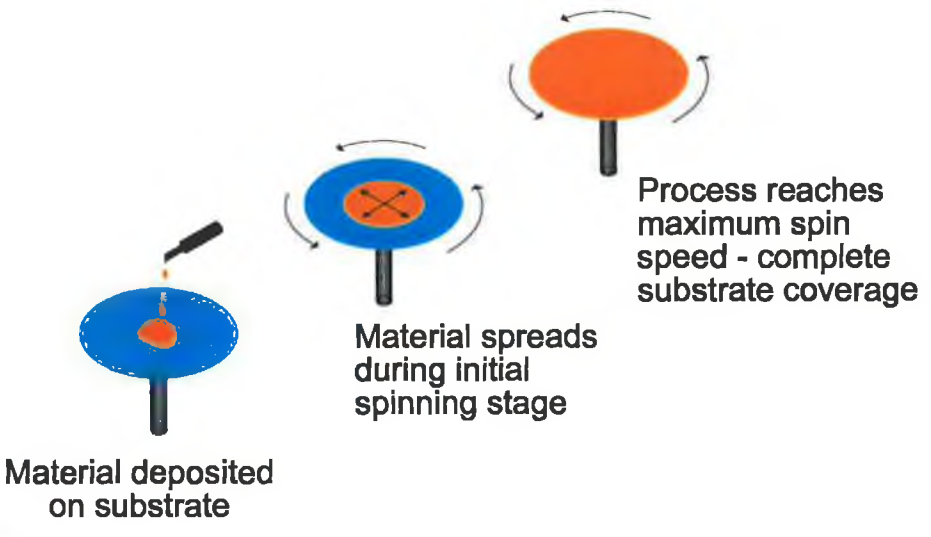

Figure 3.4: The spin-coating process.

The change of film thickness over time was first derived by Emslie *et al.* [27] by balancing the centrifugal and viscous drag forces and applying a conservation of mass condition. This yields equation 3.6

$$h = \frac{h_0}{[1 + (4\rho\omega^2 h_0^2 t/3\eta)]^{1/2}} \tag{3.6}$$

where h is the coating thickness, t is time, h_0 is the initial coating thickness before spinning, ω is the spin speed, η is the solution viscosity and ρ is its density. This equation highlights the reason for the exceptionally uniform coatings produced by spin-coating, i.e., the balancing of inward (viscous drag) and outward (centrifugal) forces in a manner that results in a complete lack of radial dependence in the

thickness.

After the first few seconds of spin-coating a sol-gel solution, the viscosity rises due to the concentration of the solution by evaporation. This continues up until the point where the centrifugal force is overwhelmed and evaporation becomes the driving force behind film thinning. This transition controls the final thickness obtained. Assuming a power law dependence of viscosity with concentration [28], the final film thickness can be derived as follows

$$h_f = c_0 \left[\frac{3\nu_0 \epsilon}{2(1 - c_0)\omega^2} \right]^{1/3} \tag{3.7}$$

where c_0 corresponds to the initial polymer concentration, ν_0 is the inital kinematic viscosity ($\nu = \eta/\rho$) and ϵ is the evaporation rate. It can, however, be shown that the thickness is inversely proportional to $\omega^{1/2}$ and not $\omega^{2/3}$ due to the fact that the rate of air flow onto a spinning disk is proportional to $\omega^{1/2}$, resulting in a similar spin-rate dependence for ϵ. Modifying equation 3.7 accordingly means that it can be used to predict the thickness of a spin-coated sol-gel thin film. It should be noted that this relation is valid only for solutions having a shear rate-independent viscosity, which is the case for dilute solutions. Consequently, for sols nearing gelation (with correspondingly increased viscosities), the outer regions will be less viscous than those near the centre, resulting in a thickness gradient. However, this was not normally the case for the sols deposited in the course of this work, as film deposition typically occurred within 24 hours of sol preparation.

3.10 Conclusions

This chapter provides an overview of sol-gel technology, its advantages and applications. In particular, the hydrolysis and condensation reactions that form the basis of the sol-gel process were described along with the influence of the most important process parameters on the physical properties of the final sol-gel structure. Several modified processing techniques that result in significant changes to the properties of the sol-gel material were also reported. Among the parameters that can be tailored using these methods are thin film refractive index and sur-

face wettability. The advantages of the sol-gel process as it applies to optical sensing have also been highlighted, specifically the ability to encapsulate analyte-sensitive reagents within the transparent sol-gel matrix. Sol-gel technology offers a viable route for the fabrication of both optically addressable sensing layers and integrated optical components such as planar waveguides, both of which can form the basis of robust optical sensor platforms.

Bibliography

[1] M. Ebelman, "Untersuchungen uber die Verbindung der Borsaure und Kieselsaure mit Aether.," *Annales de Chimie et de Physique*, vol. 57, no. 3, pp. 319–355, 1846.

[2] C. J. Brinker and G. W. Scherer, *Sol-Gel Science - The Physics and Chemistry of Sol-Gel Processing*. New York: Academic Press, 1990.

[3] L. L. Hench and J. K. West, "The Sol-Gel Process," *Chem. Rev.*, vol. 90, pp. 33–72, 1991.

[4] L. C. Klein, *Sol-Gel Optics - Processing and Applications*. Kluwer Academic Publishers, 1994.

[5] R. Makote and M. M. Collinson, "Organically modified silicate films for stable pH sensors," *Analytica Chimica Acta*, vol. 394, no. 2-3, pp. 195–200, 1999.

[6] F. Ismail, C. Malins, and N. J. Goddard, "Alkali treatment of dye-doped sol-gel glass films for rapid optical pH sensing," *Analyst*, vol. 127, no. 2, pp. 253–257, 2002.

[7] G. R. Atkins, R. M. Krolikowska, and A. Samoc, "Optical properties of an ormosil system comprising methyl- and phenyl-substituted silica," *Journal of Non-Crystalline Solids*, vol. 265, no. 3, pp. 210–220, 2000.

[8] C. McDonagh, A. McEvoy, and B. MacCraith, "Optimisation of sol-gel derived silica films for optical oxygen sensing," *Journal of Sol-Gel Science and Technology*, vol. 8, pp. 1121–1125, 1997.

[9] C. McDonagh, A. McEvoy, and B. MacCraith, "Dissolved oxygen sensor based on fluorescence quenching of oxygen-sensitive ruthenium complexes immobilized in sol-gel derived porous silica coatings," *The Analyst*, vol. 121, pp. 785–788, 1996.

[10] G. O'Keeffe, B. D. MacCraith, A. K. McEvoy, C. M. McDonagh, J. McGilp, B. O'Kelly, J. D. O'Mahony, and M. Cavanagh, "Light-emitting-diode-based

oxygen sensing using evanescent wave excitation of a dye-doped sol-gel coating," *Optical Engineering*, vol. 33, no. 12, pp. 3861–3866, 1994.

[11] C. von Bultzingslowen, A. K. McEvoy, C. McDonagh, and B. D. MacCraith, "Lifetime-based optical sensor for high-level pCO(2) detection employing fluorescence resonance energy transfer," *Analytica Chimica Acta*, vol. 480, no. 2, pp. 275–283, 2003.

[12] C. von Bultzingslowen, A. K. McEvoy, C. McDonagh, B. D. MacCraith, I. Klimant, C. Krause, and O. S. Wolfbeis, "Sol-gel based optical carbon dioxide sensor employing dual luminophore referencing for application in food packaging technology," *Analyst*, vol. 127, no. 11, pp. 1478–1483, 2002.

[13] C. Malins and B. D. MacCraith, "Dye-doped organically modified silica glass for fluorescence based carbon dioxide gas detection," *Analyst*, vol. 123, no. 11, pp. 2373–2376, 1998.

[14] C. Malins, T. M. Butler, and B. D. MacCraith, "Influence of the surface polarity of dye-doped sol-gel glass films on optical ammonia sensor response," *Thin Solid Films*, vol. 368, no. 1, pp. 105–110, 2000.

[15] C. Malins, H. G. Glever, T. E. Keyes, J. G. Vos, W. J. Dressick, and B. D. MacCraith, "Sol-gel immobilised ruthenium(II) polypyridyl complexes as chemical transducers for optical pH sensing," *Sensors and Actuators B-Chemical*, vol. 67, no. 1-2, pp. 89–95, 2000.

[16] C. S. Burke, L. Polerecky, and B. D. MacCraith, "Design and fabrication of enhanced polymer waveguide platforms for absorption-based optical chemical sensors," *Measurement Science and Technology*, vol. 15, no. 6, pp. 1140–1145, 2004.

[17] S. Saavedra, P. Skrdla, N. Armstrong, S. Mendes, and N. Peyghambarian, "Sol-gel based planar waveguide sensor for water vapour," *Analytical Chemistry*, vol. 71, no. 7, pp. 1332–1337, 1999.

[18] T. Werner, I. Klimant, and O. Wolfbeis, "Ammonia-sensitive polymer matrix employing immobilized indicator ion pairs," *Analyst*, vol. 120, pp. 1627–1631, 1995.

[19] A.Mills and Q. Chang, "Tuning colourimetric and fluorimetric gas sensors for carbon dioxide," *Analytica Chimica Acta*, vol. 285, pp. 113–123, 1994.

[20] C. Malins, A. Doyle, B. MacCraith, F. Kvasnik, M. Landl, P. Simon, L. Kalvoda, R. Lukas, K. Pufler, and I. Babusik, "Personal ammonia sensor for industrial environments," *Journal of Environmental Monitoring*, vol. 1, pp. 417–422, 1999.

[21] S. Saavedra, L. Yang, N. Armstrong, and J. Hayes, "Fabrication and characterization of low-loss, sol-gel planar waveguides," *Analytical Chemistry*, vol. 66, no. 8, pp. 1254–1263, 1994.

[22] M. Andrews, A. Fardad, G. Milova, A. Malek-Tabrizi, and S. Najafi, "Fabrication of ridge waveguides: a new sol-gel route," *Applied Optics*, vol. 37, no. 12, pp. 2429–2434, 1998.

[23] Y. Moreau, P. Coudray, P. Etienne, and J. Porque, "New developments in integrated optics using the sol-gel process," *Sol-Gel and Polymer Photonic Devices - Critical Reviews*, vol. CR68, pp. 286–303, 1998.

[24] P. Ayras, J. T. Rantala, S. Honkanen, S. B. Mendes, and N. Peyghambarian, "Diffraction gratings in sol-gel films by direct contact printing using a uv-mercury lamp," *Optics Communications*, vol. 162, no. 4-6, pp. 215–218, 1999.

[25] S. Aubonnet, H. F. Barry, C. von Bultzingslowen, J. M. Sabattie, and B. D. MacCraith, "Photo-patternable optical chemical sensors based on hybrid sol-gel materials," *Electronics Letters*, vol. 39, no. 12, pp. 913–914, 2003.

[26] J. B. Wachtman and R. A. H. (Editors), *Ceramic Films and Coatings.* New Jersey: Noyes Publications, 1993.

[27] A. G. Emslie, F. T. Bonner, and L. G. Peck, "Flow of a viscous liquid on a rotating disk," *Journal of Applied Physics*, vol. 29, no. 5, pp. 858–862, 1958.

[28] D. Meyerhofer, "Characteristics of resist films produced by spinning," *Journal of Applied Physics*, vol. 49, no. 7, pp. 3993–3997, 1978.

Chapter 4

Rapid Prototyping Techniques

The term "rapid prototyping" appears throughout this work and is used to encompass a range of different fabrication techniques that can be used either separately or in combination to facilitate the translation of a particular concept into a practical sensor platform in a matter of hours. The majority of these techniques involve polymer processing due to the ease with which polymers can be patterned, moulded and machined, thereby reducing the overall sensor platform development time. In this chapter, the various polymer processing technologies and template fabrication techniques that comprise the rapid prototyping technology used in this work are described.

4.1 Soft Lithography

Soft lithography is the name given to a set of techniques developed by the Whitesides Group at Harvard that make use of a rubber stamp as a patterning element [1]. The most commonly used material for such stamps is poly(dimethylsiloxane) (PDMS), a transparent silicone rubber that is commercially available as Sylgard 184 from Dow Corning. Soft lithographic techniques have found widespread application in recent years including the fabrication of ridge waveguides [2, 3, 4], Schottky diodes [5], organic smart pixels [6] and a wide variety of functional optical microstructures [7, 8, 9, 10]. PDMS moulds have also been used as flowcells in microfluidic applications [11, 12, 13, 14].

4.1.1 PDMS mould fabrication

PDMS is available as a 1.1kg kit consisting of a liquid prepolymer and a curing agent. These are normally mixed together in a 10:1 ratio by weight or volume and cured at an elevated temperature to solidify the material. The mixing ratio of 10:1 is that recommended by Dow Corning but the flexibility of the resultant mould can be tailored by adjusting this ratio (e.g., an increase in the amount of curing agent relative to prepolymer results in a more rigid mould). There are a number of possible curing regimes for PDMS, but in this work, all mixtures were cured for 1 hour at 70°C. Fig. 4.1 demonstrates the steps involved in the fabrication of a PDMS stamp.

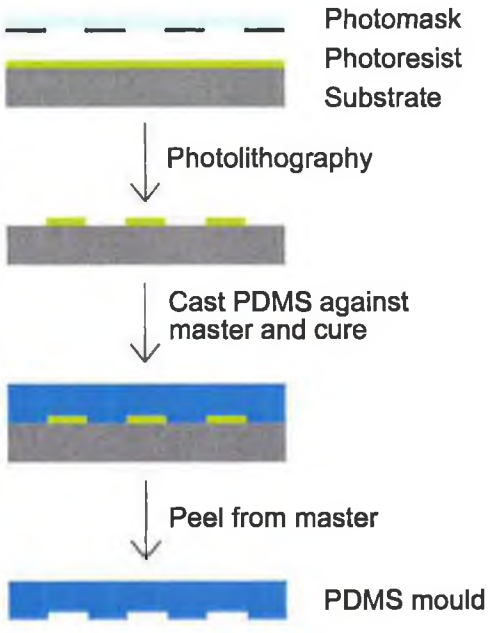

Figure 4.1: Fabrication of a PDMS stamp.

Liquid prepolymer is cast against a suitable master and allowed to degas in ambient conditions. Once all bubbles have risen out of the mixture, it is placed in the oven and cured. After curing, the crosslinked PDMS mould is allowed to cool down and is then peeled carefully from the template. A template silanisation step is often introduced prior to casting the liquid prepolymer in order to render the template "non-stick", thereby improving the ease with which the mould can be removed.

An important step in this process is the production of a master against which

the PDMS is moulded. Photolithographic techniques are by far the most popular although there are several alternatives. These master fabrication techniques will be explained in detail in Sec. 4.3. The physical properties of PDMS are what make it attractive as a patterning element. It is elastomeric, making it possible to pattern non-planar surfaces and it naturally makes conformal contact with the surface. It is optically transparent down to approximately 330nm, which both facilitates the patterning of photocurable materials whilst contained in the mould and also makes PDMS-based microfluidic chips optically addressable. It also has a low surface energy, meaning that materials will adhere preferentially to the substrate being patterned. PDMS is resistant to polar solvents such as methanol and ethanol, which makes it an ideal choice for patterning sol-gel-based structures as the liquid sols commonly employ ethanol to act as a co-solvent. These advantages, along with the ease of fabrication of the stamp, have been central to the development of soft lithography. In the following sections, the various soft lithographic techniques that have been developed over the past few years will be described. They are:

- Micromoulding in Capillaries (MIMIC)
- Microtransfer Moulding (μTM)
- Replica Moulding
- Microcontact Printing (μCP)
- Solvent-Assisted Micromoulding (SAMIM)

4.1.2 Micromoulding in capillaries (MIMIC)

Fig. 4.2 illustrates the principle of micromoulding in capillaries. A PDMS mould carrying a recessed network of channels is placed on the substrate and a drop of the material to be patterned is placed at the entrance to the mould. The material then fills the channels by capillary action and is cured (in most cases by UV-irradiation) once the mould has filled. For this method to work, it is necessary that the mould carry a continuous structure so that capillary action is facilitated. This method is ideally suited to patterning photocurable materials

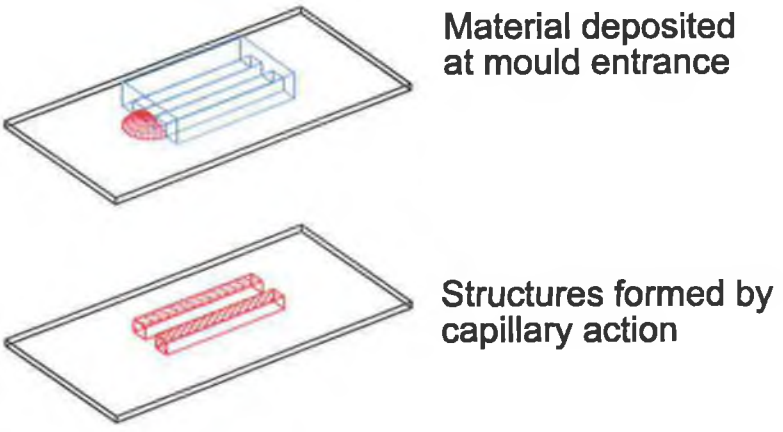

Figure 4.2: Micromoulding in capillaries using a PDMS mould.

due to the transparency of PDMS and it also eliminates the use of a photomask due to the spatial confinement of the material within the PDMS channels.

MIMIC has been used to pattern a variety of structures including half-wave rectifier circuits [15], ridge waveguides [4] and field effect transistors [16]. For a comprehensive review of this technique and its applications, see [17]. In this work, the most common application of MIMIC was the fabrication of ridge waveguides using UV-curable sol-gel (see Chapter 8, Sec. 8.5).

4.1.3 Microtransfer moulding (μTM)

This technique involves first filling a PDMS mould with the desired material and then bringing the mould into contact with the substrate, thus transferring the pattern carried by the mould onto the substrate. Fig. 4.3 illustrates the process. Unlike MIMIC, μTM is suitable for pattering both continuous and discrete structures and has been employed in various applications including the fabrication of waveguide couplers [18] and arrays of Schottky diodes [5].

The stamp-printing process described in Chapter 8, Sec. 8.5 is a modified version of μTM and was used to deposit discrete sensor spots for the detection of gaseous oxygen.

4.1.4 Replica moulding

This is a straightforward yet useful technique that is employed primarily as a means to avoid excessive wear and tear on expensive masters. This first step is

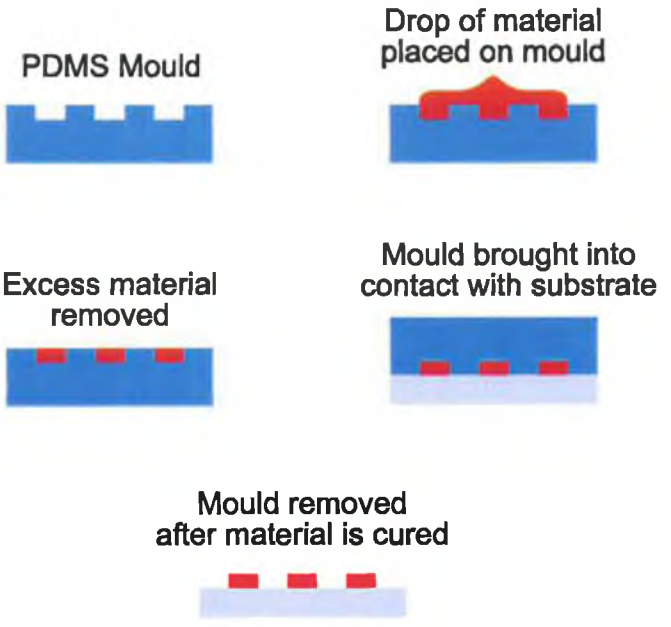

Figure 4.3: Microtransfer moulding

identical to that of the other soft lithographic techniques in that liquid PDMS is cast against the master and cured to form a mould. The next step involves casting another polymer, e.g., polyurethane, against the PDMS mould and curing it to form a replica of the master. This replica can then be used in place of the master for the relevant application, e.g, grating coupler fabrication. Another related application of replica moulding is the production of physically modified versions of the master template and it is the elastomeric nature of PDMS that makes this possible. The second polymer is simply cast against a compressed or otherwise deformed PDMS mould [7].

It is also possible to produce PDMS replicas from PDMS templates by first silanising the template. This step makes it possible to peel the replica from the template once cured. Without the silanisation procedure, both template and replica fuse together to form a solid block of PDMS. Throughout this work, the silane used to perform this function was trichloro(pefluorooctyl)silane and, in order to silanise a PDMS template, 1-2 drops were placed beside the template in a glass petri dish with the lid in place and placed in a fumehood for approximately 15 minutes. The template was then washed with acetone and dried in an oven at 70°C for 30mins, after which it was ready for use. This method was used to

fabricate the PDMS stamps described in Chapter 8, Sec. 8.3.

4.1.5 Microcontact printing (μCP)

Fig. 4.4 demonstrates the principle of μCP.

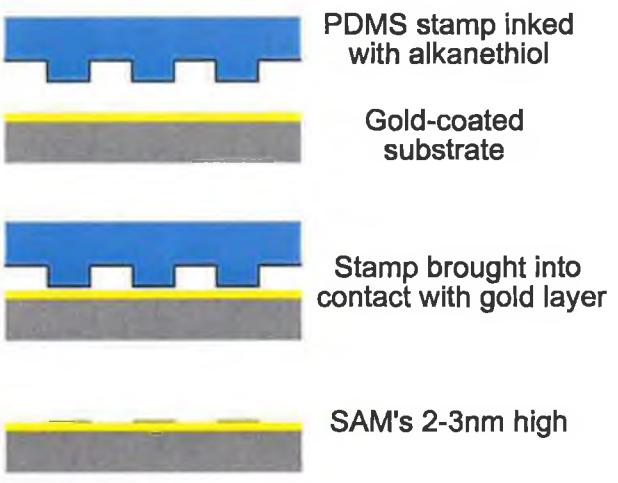

Figure 4.4: Microcontact printing.

A PDMS stamp having the desired features is "inked" with an alkanethiol and brought into contact with a gold surface. This results in the formation of self-assembled monolayers (SAM's) on the gold surface. These layers can then be exploited in a variety of ways. One of the main applications has been the use of SAM's as ultrathin resists in the fabrication of gold microstructures [19, 15, 6, 20], but they have also been used to tailor surface properties such as wettability [21, 22]. μCP has also found applications in biology including studies of cell shape [23] and the immobilisation of proteins and antibodies on solid substrates for biosensing applications [24, 25]. It is also worth noting that, while the gold/alkanethiol system is most popular in these applications, the printing of SAM's on silicon and various oxide layers has also been examined [26, 27].

4.1.6 Solvent-assisted micromoulding (SAMIM)

This process can be thought of as a low pressure embossing technique and is depicted in Fig. 4.5. The schematic illustrates the fabrication of surface corrugation grating couplers via SAMIM as this was the application for which this patterning

method was employed in this work. For details of the master used for mould fabrication, see Chapter 8, Sec. 8.1.

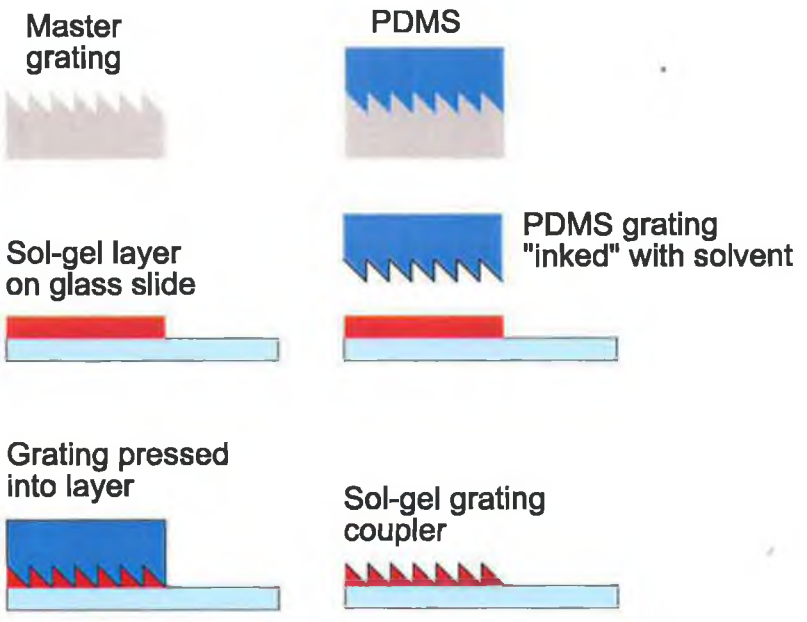

Figure 4.5: Sol-gel grating coupler fabrication by Solvent-Assisted Micromoulding

The PDMS mould is inked with a good solvent for the material to be patterned. The stamp is then pressed into the freshly deposited layer and the solvent causes the material to reflow and conform to the profile on the stamp. After curing, the stamp is removed, leaving a surface corrugation grating coupler on the substrate.

This process can be slightly modified by first diluting the material to be patterned with the required solvent. It is then possible to use an uncoated PDMS mould for the micromoulding step. This method is more efficient than the former as it ensures uniform solvent distribution within the patternable material, thereby improving the uniformity of the moulded structures. It is this latter technique that was employed for the grating coupler fabrication described in Chapter 8.

4.1.7 Microfluidic systems

While PDMS has found a niche application in soft lithography, it should be noted that it is one of the most popular materials used for the fabrication of microfluidic systems (μFS) for sensing applications. This is due in no small part to

its compatibility with rapid prototyping methods and the ease with which PDMS can form a seal with sufficiently smooth surfaces. It can also be plasma treated in order to render it hydrophilic, thus improving aqueous fluid flow. Oxygen or air plasmas are most commonly used to achieve this and, if brought into contact with a similarly treated substrate (e.g., glass), PDMS forms an irreversible bond with that surface, resulting in a securely encapsulated (and optically addressable) microfluidic chip [13].

μFS fabricated from PDMS have found widespread use in recent years including capillary electrophoresis [13], cell sorting [28], optical sensing using reconfigurable diffraction gratings [29], patterning of surfaces for biosensing applications [14, 30, 31] and 3-D problem solving [32].

In this work, PDMS flowcells have been used for sample delivery during the examination of the optical pH sensor described in Chapter 7, Sec. 7.3 and the SU-8 masters used to fabricate these flowcells are described in Appendix B.

4.2 Polymer processing technology

While soft lithography is, technically speaking, a set of polymer processing techniques itself, it was decided to present it separately due to the array of techniques encompassed by the term and the fact that it involves the use of a liquid prepolymer that is thermally cured to form a solid patterning element. This element can then be used to pattern *other* structures but does not generally form part of the finished platforms, with the exception of PDMS microfluidic systems.

The techniques described in this section all involve the processing of a solid polymer to produce the desired sensor platform, which then forms an integral part of the diagnostic system.

4.2.1 Why polymers?

Polymers are an extremely versatile range of materials that possess diverse physical and chemical properties that can be tailored to suit many different applications. A wide range of optical quality polymers are available with transmittances comparable to glass, yet these materials can be moulded and machined with relative ease to produce functional microstructures, a task that is far more

complicated for glass substrates. The surface properties of polymers can also be modified by a variety of processes including plasma treatment [33, 34] and UV/ozone cleaning [35, 36] in order to alter their wettability, thereby influencing thin film adhesion and quality. Surfaces can also be modified using these processes or alternative chemical treatments to provide suitable binding sites for biological target analytes [37, 38].

One of the main advantages of polymers is their low cost. These materials can be used for the fabrication if high-quality, mass producible optical platforms, the obvious examples being CD and DVD technology. Their low cost also means that they are suitable for the development of potentially disposable diagnostic platforms. The ability to develop high optical quality, mass producible sensor platforms makes polymer technology an ideal choice for development of optical sensor platforms based on rapid prototyping. What follows is a description of the polymer processing technologies employed at various stages throughout this work.

4.2.2 Micro-injection moulding

Micro-injection moulding is the polymer processing technique that has been most frequently employed during this work. A schematic of a micro-injection moulder is shown in Fig. 4.6. The sections of most relevance to the operation of the moulder are labelled in the schematic.

Polymer pellets are held in the hopper from which they are taken into the plastification chamber. This chamber is heated to a temperature sufficient to melt the pellets and the resultant liquid polymer is injected under high pressure into the mould / cavity by the injection piston via the nozzle, which is also heated to ensure the polymer remains liquid until it enters the mould.

The mould typically consists of two metal plates, one of which has been machined to act as the cavity, the other being flat in most cases. The cavity is mounted on the hydraulically controlled moving platen and the flat plate is mounted on the fixed platen directly opposite. Upon completion of the injection cycle, the polymer is allowed to cool and solidify, a step which takes typically less than 3 seconds. The mobile platen then retracts, separating the mould into its two constituent parts and the solidified polymer is ejected from the cavity by

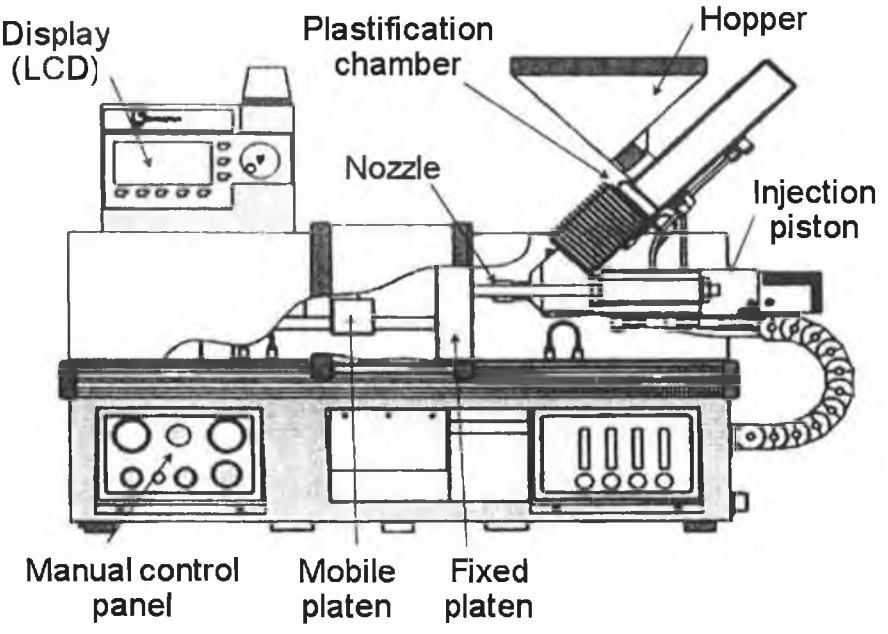

Figure 4.6: Schematic of micro-injection moulder (taken from [39]).

ejector pins that form part of the mounting. In the case of an automatic cycle, the platen moves forward again, closing the mould, and the injection step is repeated. In this manner it is possible to produce hundreds of polymer chips in a matter of minutes.

The injection moulding process is entirely dependent on the polymer used as this determines the range of melting temperatures that are required and also affects the injection pressure required to completely fill the cavity. The design of the mould itself is extremely important as it dictates the amount of material required per cycle, which is regulated by the injection piston. It also affects the nature of the fluid flow within the mould and an ineffective design can result in flow lines and weld lines (resulting from the confluence of separate polymer flows) being present in the ejected chip. For a particular polymer and mould, it is therefore necessary to determine the combination of parameters required to produce an optimum output and these parameters can be stored in an operating macro for future work.

For a description of the various moulding parameters employed during the fabrication of the polymer platforms used in this work, see Sec. 7.1.

4.2.3 Hot embossing

This technique differs significantly from micro-injection moulding as can be seen from Fig. 4.7. The polymer substrate to be embossed normally takes the form of a thin sheet of the required material. This is placed on a hotplate directly underneath the mount for the template to be used. The template can be made from a variety of materials including metals, silicon and certain photoresists (see Sec. 4.3 for a description of template fabrication techniques).

Figure 4.7: HEX 02 hot embossing system.

Once the template and substrate are in place, the template mount is brought into contact with a metallic ring surrounding the hotplate. These seal together, forming a chamber to which vacuum is applied. The polymer substrate is then heated to a temperature sufficient to soften the material and the template is embossed into the polymer using forces ranging from 10 - 200 kN. Once the embossing procedure is judged to have been completed, the template is retracted, opening the chamber and the sample is allowed to cool. As with injection moulding, the parameters required to produce the desired chip are stored in an operating macro which ensures reproducible results across all samples. This technique is ideal for the production of planar, polymer microfluidic platforms and was used for the fabrication of a microfluidic sensor chip for the detection of copper [40].

However, it is not a high throughput technique and is also unsuited to the fabrication of platforms with more complex 3-D topographies. The platform thickness is also dependent on the dimensions of the polymer substrate used and this detracts from the versatility of the process.

4.2.4 Laser micromachining

This process is ideal for the rapid fabrication of prototype polymer sensor chips. It involves the use of laser ablation to machine polymer substrates in a pre-defined pattern. This pattern can be created using the in-built positioning macros of the laser machining rig itself or it can be based on an imported CAD design. The laser micromachining setup at this laboratory consists of a CO_2 laser and a KrF excimer laser, the choice of laser being dependent on the nature of the substrate being machined.

This technique is relatively fast compared with hot embossing especially when being used to cut several chips from one substrate. However, microfluidic systems fabricated by ablating to a controlled depth in the substrate can contain a V-groove channel profile due to the beam profile of the laser. This can sometimes adversely affect fluid flow in these systems, making hot embossing the more attractive choice for chip fabrication.

Laser micromachining can also be used to fabricate polymer templates for PDMS mould fabrication.

4.3 Master fabrication techniques

Central to the success of the polymer rapid prototyping techniques described above has been the development of versatile template / master fabrication methods. These methods combine accuracy and ease of implementation when compared to those required to produce glass or semiconductor-based platforms. This section describes the master fabrication techniques that were employed during the various stages of this work.

4.3.1 CNC micromilling

Computer Numerically Controlled (CNC) micromilling was employed for the fabrication of several templates during the course of this work. It was most commonly employed to produce brass cavities or moulds for use in micro-injection moulding. There are three stages in the production of a mould using this method. They are:

1. Design of the desired mould using CAD/CAM software.

2. Production of the machining file that determines how the mould will be milled.

3. Transfer of the machining file to the CNC micromiller and the subsequent milling of the mould.

It should be noted that, while the term mould is being applied to the machined part, the items produced by CNC micromilling can be thought of as masters or templates depending on their application.

The CNC micromilling process involves the use of a machining file or macro to control the movements of a tower at the end of which, tool bits of various sizes and shapes are held in a pneumatically controlled mount referred to as the collet. The machining file specifies the coordinates to which the tower is to move along with the tool type, machining speed and rotation rate for the tool (measured in revolutions per minute). The rotation speed is dependent on the material to be machined and on the size of the tool, with metals typically requiring higher rpm's than polymers when being machined by this method.

In general, it is desirable to remove as much material as possible by using larger tools, thus reducing the amount of work to be done by the smaller, more delicate ones. At present, it is possible to use tools with diameters ranging from 0.1 mm to 3 mm and the smaller tools ($\phi < 1$ mm) are normally used to define those features too small to be machined fully using larger machining bits. The machining file instructs the micromiller to machine at certain coordinates with a particular tool and, once finished, to collect the next (smaller) tool from the integrated tool tray and to continue machining with this. In this way, the machined part is completed in stages progressing from the largest to the smallest structures defined by the machining file.

This method was used to produce the mould for the polymer waveguide platforms described in Chapter 7 (see Sec. 7.1 for figures illustrating the CAD/CAM design). Using the technique of CNC micromilling, templates can be produced within 24 hours of design conception, including the CAD/CAM design stage. It is possible to reliably manufacture feature sizes on the order of 100μm, however the tolerances of the micromiller make it impractical to attempt to mill features much smaller than that. The templates produced by micromilling also require a time-consuming polishing step depending on the application for which they are

intended. This is necessary to remove the tool paths left by the machining process and this step is described in more detail in Chapter 7, Sec. 7.1.

4.3.2 SU-8 Photolithography

SU-8 is a thick film, negative tone photoresist manufactured by Microchem (U.S.A.). It has seen extensive use in recent years for a variety of applications including the production of templates for PDMS moulds [41, 42, 9, 43, 10] and the fabrication of micro-electromechanical systems (MEMS) [44] and micro-optical systems [45, 46]. Its popularity arises from the fact that it is possible to deposit films with thicknesses ranging from 5μm to 500μm in a single step and the crosslinked photoresist has excellent mechanical and optical properties. Fig. 4.8 illustrates the principle behind photolithography using negative-tone photoresists such as SU-8.

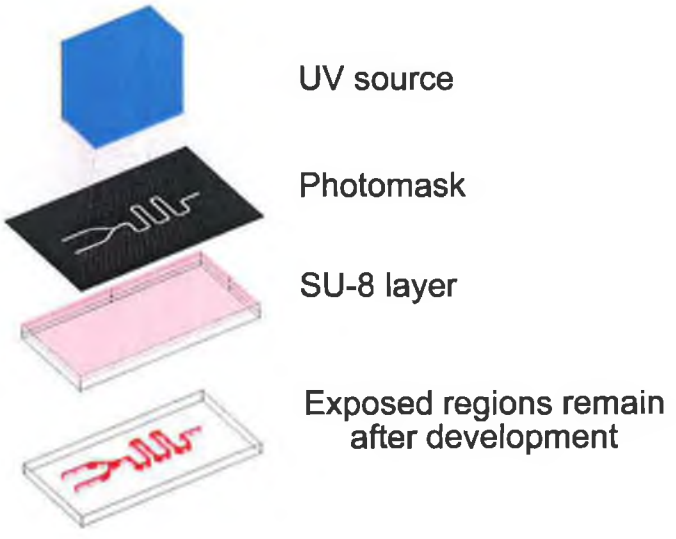

Figure 4.8: Principle of SU-8 photolithography.

Light from a suitable ultraviolet source is incident through the required photomask onto the sample, which normally consists of a rigid substrate such as silicon onto which a uniform layer of SU-8 has been deposited by the appropriate technique, e.g., spin-coating. In the areas that are exposed, the UV radiation initialises crosslinking that is completed after a thermal curing step normally referred to as the post-exposure bake. The sample is then developed using the required solvent and the area that has been crosslinked remains on the substrate, forming a positive relief structure that takes its form from the design carried on

the photomask. The thickness of the structure is defined by the thickness of the deposited SU-8 film and this property can be tailored through correct choice of deposition parameters.

The factors most affecting the quality of the final SU-8 structure are, arguably, the quality of the photomask and the uniformity of the photoresist layer, although the various process parameters such as exposure dose and post-exposure bake time also need to be optimised to provide viable structures. An inadequate exposure dose and / or post-bake time can result in the material being under-crosslinked, which causes it to crack or de-adhere entirely during the development stage. However, high quality structures will not be produced from low-precision photomasks or non-uniform photoresist layers. Film uniformity is dependent on adequate sample pre-treatment and on correct choice of deposition parameters. The latter can be controlled to a high degree depending on the coating apparatus used, while several options exist for the sample pre-treatment stage including plasma cleaning, a thorough solvent rinsing procedure or the use of a Piranha etch (see Chapter 8, Sec. 8.5.2 for a description of these protocols). In this work, spin-coating was the deposition method of choice and the coating process used for SU-8 is described in Sec. 8.5.2.

The following section describes the various techniques employed to produce photomasks for the fabrication of the SU-8 structures developed during this work.

4.3.3 Mask fabrication

High resolution printing

When deciding on a photomask fabrication technique, the application for which the SU-8 structure is intended is an important factor. In this work, one of the most common applications was for use as a template in the production of a PDMS flow-cell. These flowcells were then used in conjunction with the polymer waveguide-based sensor platforms described in Chapter 7. In this case, the surface roughness of the SU-8 structure did not need to be of optical quality, permitting the use of high-resolution printing as the photomask fabrication technique. This technique has been used for the rapid prototyping of microfluidic systems [13] and involves the production of the required design using CAD software and then printing it onto acetate. This method facilitates the rapid production of photomasks but

these masks are not suitable for the production of optical quality structures due to the limited resolution offered by office printers. Printer toner density is another important factor to be considered. If the toner density is not sufficiently high, manual blackening is required to ensure that the mask is opaque to the incident radiation where required.

Photographic reduction

This method is used in conjunction with high-resolution printing to produce miniaturised photomasks from CAD designs that have been printed onto A4 paper. A photograph of the printout is taken using high-resolution black and white 30mm photographic film and the negative then acts as the photomask for the photolithographic step. The primary advantage of this technique is that feature sizes on the order of 20μm [47] can be produced using the printout from a moderately high-resolution office printer due to the fact that the printer resolution does not have to produce the desired feature dimensions for the final mask. Instead, it is merely necessary to produce feature dimensions approximately an order of magnitude greater. This factor is of course dependent on the reduction provided by the photographic process and the efficiency of the negative-based photomask is highly dependent on the film quality and the contrast it provides between black and transparent regions. This technique was not employed in this work due to the added degree of complexity introduced by the photographic stage and the associated dark room protocols required to produce the negatives. The availability of alternative master fabrication techniques capable of producing the required feature sizes, e.g., CNC micromilling and UV laser writing (see Sec. 4.3.4) also meant that it was unnecessary to examine photographic reduction as a photomask fabrication technique. However, in the absence of these alternative processes, photographic reduction offers a viable route to the rapid fabrication of photomasks for microfluidic systems' development.

Commercial fabrication

This was the route chosen for the fabrication of the high-precision photomasks required for the production of the majority of the optical quality structures used during this work. The mask design was carried out in-house using BPM-CAD

software and the resultant file was processed by a commercial photomask fabrication facility (Compugraphics photomask solutions, U.K.) to produce a chrome-coated quartz glass plate that carried the desired structure layout. This process was used to produce the mask employed for the fabrication of the SU-8 ridge waveguide template described in Chapter 8, Sec. 8.5. The masks produced are of high quality but the cost is prohibitive and alternative fabrication techniques such as UV laser writing are currently being employed for the development of systems based on multimode ridge waveguides. However, for optical feature sizes smaller than 60μm in width, commercial fabrication is at present the most practical choice.

4.3.4 UV laser writing

This technique can be used to pattern SU-8 or UV-curable sol-gels and eliminates the need for a photomask. A schematic of the UV laser writing setup is shown in Fig. 4.9. UV light from a HeCd laser (λ=325nm) is incident on a mirror where it is then reflected through a UV lens onto the sample. The sample is mounted on a motorised XY-stage which is PC-controlled. The stage moves in a pattern that it reads from a user-defined data file, thus moving the sample across the beam spot where the photosensitive material is cured. This is quite a versatile setup in that the input file that controls the motion of the stage can be produced simply by importing the desired CAD design file. This makes it possible to design *and* fabricate a high-precision template within 24 hours.

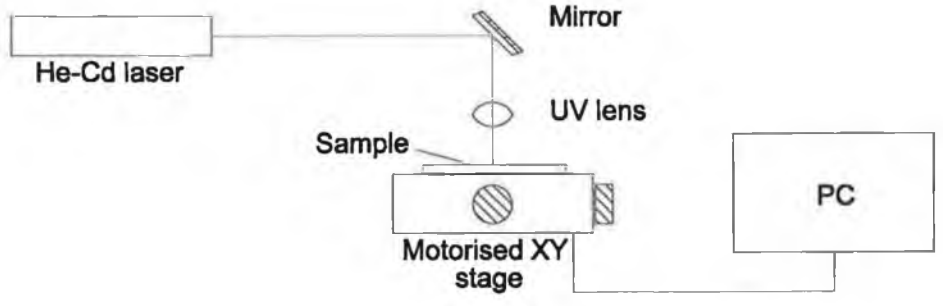

Figure 4.9: Schematic of UV laser writing setup.

4.4 Conclusions

This chapter has described the various rapid prototyping techniques that have been investigated during this work.

Soft lithography offers a range of patterning techniques that can be applied to the fabrication of sol-gel-based optical structures without the need for expensive master fabrication protocols. Chapter 8 describes some of the structures moulded using these techniques and compares their performance with systems requiring more complex processing methods.

Several polymer processing technologies have been detailed and the ability to create functional platforms for optical sensing applications quickly and efficiently has been highlighted. In particular, micro-injection moulding has proven to be a powerful tool for the high-throughput production of optical sensor platforms and its effectiveness is made evident in Chapter 7, which describes the development of enhanced polymer waveguide platforms for absorption-based optical chemical sensing.

The success of these techniques is dependent to a large degree on the quality of the master or mould used to produce the polymer platforms. The most commonly employed master fabrication techniques in this project have been described here. One element held in common between these techniques is the ability to transform a design into a physical template within 24 hours and it is this characteristic that makes them a vital element of any rapid prototyping process.

Bibliography

[1] G. Whitesides and Y. Xia, "Soft lithography," *Angewandte Chemie International Edition*, vol. 37, pp. 550–575, 1998.

[2] B. T. Lee, M. S. Kwon, J. B. Yoon, and S. Y. Shin, "Fabrication of polymeric large-core waveguides for optical interconnects using a rubber molding process," *IEEE Photonics Technology Letters*, vol. 12, no. 1, pp. 62–64, 2000.

[3] G. Whitesides, E. Kim, L. Lee, S. Smith, and M. Prentiss, "Fabrication of arrays of channel waveguides by self-assembly using patterned organic monolayers as templates," *Advanced Materials*, vol. 8, no. 2, pp. 139–142, 1996.

[4] A. Stoddart, X.-M. Zhao, S. Smith, E. Kim, Y. Xia, M. Prentiss, and G. Whitesides, "Fabrication of single-mode polymeric waveguides using micromolding in capillaries," *Advanced Materials*, vol. 8, no. 5, pp. 420–424, 1996.

[5] T. Deng, J. Hu, R. Beck, R. Westervelt, and G. Whitesides, "Fabrication of arrays of Schottky diodes using microtransfer molding," *Sensors and Actuators A*, vol. 75, pp. 65–69, 1999.

[6] J. A. Rogers, Z. N. Bao, A. Dodabalapur, and A. Makhija, "Organic smart pixels and complementary inverter circuits formed on plastic substrates by casting and rubber stamping," *IEEE Electron Device Letters*, vol. 21, no. 3, pp. 100–103, 2000.

[7] E. Kim, Y. Xia, X.-M. Zhao, J. Rogers, M. Prentiss, and G. Whitesides, "Complex optical surfaces formed by replica molding against elastomeric masters," *Science*, vol. 273, pp. 347–349, 1996.

[8] J. R. Lawrence, G. A. Turnbull, and I. D. W. Samuel, "Polymer laser fabricated by a simple micromolding process," *Applied Physics Letters*, vol. 82, no. 23, pp. 4023–4025, 2003.

[9] Y. Y. Huang, G. T. Paloczi, J. Scheuer, and A. Yariv, "Soft lithography replication of polymeric microring optical resonators," *Optics Express*, vol. 11, no. 20, pp. 2452–2458, 2003.

[10] K. Hosokawa, K. Hanada, and R. Maeda, "A polydimethylsiloxane (PDMS) deformable diffraction grating for monitoring of local pressure in microfluidic devices," *Journal of Micromechanics and Microengineering*, vol. 12, no. 1, pp. 1–6, 2002.

[11] M. L. Chabinyc, D. T. Chiu, J. C. McDonald, A. D. Stroock, J. F. Christian, A. M. Karger, and G. M. Whitesides, "An integrated fluorescence detection system in poly(dimethylsiloxane) for microfluidic applications," *Analytical Chemistry*, vol. 73, no. 18, pp. 4491–4498, 2001.

[12] J. R. Anderson, D. T. Chiu, R. J. Jackman, O. Cherniavskaya, J. C. McDonald, H. K. Wu, S. H. Whitesides, and G. M. Whitesides, "Fabrication of topologically complex three-dimensional microfluidic systems in PDMS by rapid prototyping," *Analytical Chemistry*, vol. 72, no. 14, pp. 3158–3164, 2000.

[13] D. C. Duffy, J. C. McDonald, O. J. A. Schueller, and G. M. Whitesides, "Rapid prototyping of microfluidic systems in poly(dimethylsiloxane)," *Analytical Chemistry*, vol. 70, no. 23, pp. 4974–4984, 1998.

[14] A. Bernard, E. Delamarche, H. Schmid, B. Michel, and H. Biebuyck, "Patterned delivery of immunoglobulins to surfaces using microfluidic networks," *Science*, vol. 276, pp. 779–781, 1997.

[15] T. Deng, L. Goetting, J. Hu, and G. Whitesides, "Microfabrication of half-wave rectifier circuits using soft lithography," *Sensors and Actuators A*, vol. 75, pp. 60–64, 1999.

[16] J. Hu, R. Beck, T. Deng, R. Westervelt, K. Maranowski, A. Gossard, and G. Whitesides, "Using soft lithography to fabricate GaAs/AlGaAs heterostructure field effect transistors," *Applied Physics Letters*, vol. 71, no. 14, pp. 2020–2022, 1997.

[17] Y. Xia, E. Kim, and G. Whitesides, "Micromolding in capillaries: Applications in materials science," *J. Am. Chem. Soc.*, vol. 118, pp. 5722–5731, 1996.

[18] S. Smith, X.-M. Zhao, S. Waldman, G. Whitesides, and M. Prentiss, "Demonstration of waveguide couplers fabricated using microtransfer molding," *Applied Physics Letters*, no. February 6, pp. 1–9, 1997.

[19] G. Whitesides and A. Kumar, "Features of gold having micrometer to centimeter dimensions can be formed thorugh a combinaton of stamping with an elastomeric stamp and an alkanethiol "ink" followed by chemical etching," *Applied Physics Letters*, vol. 63, no. 14, pp. 2002–2004, 1993.

[20] J. Wilbur, R. Jackman, and G. Whitesides, "Fabrication of submicrometer features on curved substrates by microcontact printing," *Science*, vol. 269, pp. 664–666, 1995.

[21] J. Folkers, N. Abbott, and G. Whitesides, "Manipulation of the wettability of surfaces on the 0.1- to1-micrometer scale through micromachining and molecular self-assembly," *Science*, vol. 257, pp. 1380–1382, 1992.

[22] A. Kumar and G. Whitesides, "Patterned condensation figures as optical diffraction gratings," *Science*, vol. 263, no. 7 January, pp. 60–62, 1994.

[23] A. Kumar, R. Singhvi, G. Lopez, G. Stephanopoulos, D. I. Wang, G. Whitesides, and D. Ingber, "Engineering cell shape and function," *Science*, vol. 264, pp. 696–698, 1994.

[24] S. Takayama, R. Kane, E. Ostuni, D. Ingber, and G. Whitesides, "Patterning proteins and cells using soft lithography," *Biomaterials*, vol. 20, pp. 2363–2376, 1999.

[25] R. Davis, P. S. John, N. Cady, J. Czajka, C. Batt, and H. Craighead, "Diffraction-based cell detection using a microcontact printed antibody grating," *Analytical Chemistry*, vol. 70, pp. 1108–1111, 1998.

[26] H. Craighead and P. S. John, "Microcontact printing and pattern transfer using trichlorosilanes on oxide substrates," *Applied Physics Letters*, vol. 68, no. 7, pp. 1022–1024, 1996.

[27] M. Mrksich, Y. Xia, and G. W. E. Kim, "Microcontact printing of octadecylsiloxane on the surface of silicon dioxide and its application in microfabrication," *J. Am. Chem. Soc.*, vol. 117, pp. 9576–9577, 1995.

[28] S. K. Sia and G. M. Whitesides, "Microfluidic devices fabricated in poly(dimethylsiloxane) for biological studies," *Electrophoresis*, vol. 24, no. 21, pp. 3563–3576, 2003.

[29] O. J. A. Schueller, D. C. Duffy, J. A. Rogers, S. T. Brittain, and G. M. Whitesides, "Reconfigurable diffraction gratings based on elastomeric microfluidic devices," *Sensors and Actuators A-Physical*, vol. 78, no. 2-3, pp. 149–159, 1999.

[30] C. A. Rowe-Taitt, J. P. Golden, M. J. Feldstein, J. J. Cras, K. E. Hoffman, and F. S. Ligler, "Array biosensor for detection of biohazards," *Biosensors and Bioelectronics*, vol. 14, no. 10-11, pp. 785–794, 2000.

[31] A. Bernard, E. Delamarche, H. Schmid, A. Bietsch, B. Michel, and H. Biebuyck, "Microfluidic networks for chemical patterning of substrates: Design and application to bioassays," *J. Am. Chem. Soc.*, vol. 120, pp. 500–508, 1998.

[32] D. T. Chiu, E. Pezzoli, H. K. Wu, A. D. Stroock, and G. M. Whitesides, "Using three-dimensional microfluidic networks for solving computationally hard problems," *Proceedings of the National Academy of Sciences of the United States of America*, vol. 98, no. 6, pp. 2961–2966, 2001.

[33] Y. M. Chung, M. J. Jung, J. G. Han, M. W. Lee, and Y. M. Kim, "Atmospheric rf plasma effects on the film adhesion property," *Thin Solid Films*, vol. 447, pp. 354–358, 2004.

[34] J. Tyczkowski, "Plasma surface modification of polymer materials," *Przemysl Chemiczny*, vol. 82, no. 8-9, pp. 1262–1264, 2003.

[35] K. Efimenko, W. E. Wallace, and J. Genzer, "Surface modification of sylgard-184 poly(dimethyl siloxane) networks by ultraviolet and ultraviolet/ozone treatment," *Journal of Colloid and Interface Science*, vol. 254, no. 2, pp. 306–315, 2002.

[36] L. J. Matienzo and S. K. Winnacker, "Dry processes for surface modification of a biopolymer: Chitosan," *Macromolecular Materials and Engineering*, vol. 287, no. 12, pp. 871–880, 2002.

[37] T. G. van Kooten, H. T. Spijker, and H. J. Busscher, "Plasma-treated polystyrene surfaces: model surfaces for studying cell-biomaterial interactions," *Biomaterials*, vol. 25, no. 10, pp. 1735–1747, 2004.

[38] M. R. Davidson, S. A. Mitchell, and R. H. Bradley, "Uv-ozone modification of plasma-polymerised acetonitrile films for enhanced cell attachment," *Colloids and Surfaces B-Biointerfaces*, vol. 34, no. 4, pp. 213–219, 2004.

[39] *Babyplast 6/10 Instruction Manual.* Cronoplast S.L.: Barcelona.

[40] E. Tyrrell, C. Gibson, B. D. MacCraith, D. Gray, P. Byrne, N. Kent, C. Burke, and B. Paull, "Development of a micro-fluidic manifold for copper monitoring utilising chemiluminescence detection," *Lab on a Chip*, vol. 4, 2004.

[41] T. Yamamoto, T. Nojima, and T. Fujii, "PDMS-glass hybrid microreactor array with embedded temperature control device. application to cell-free protein synthesis," *Lab On a Chip*, vol. 2, no. 4, pp. 197–202, 2002.

[42] J. Tien, C. M. Nelson, and C. S. Chen, "Fabrication of aligned microstructures with a single elastomeric stamp," *Proceedings of the National Academy of Sciences of the United States of America*, vol. 99, no. 4, pp. 1758–1762, 2002.

[43] N. Chronis, G. L. Liu, K. H. Jeong, and L. P. Lee, "Tunable liquid-filled microlens array integrated with microfluidic network," *Optics Express*, vol. 11, no. 19, pp. 2370–2378, 2003.

[44] J. Zhang, K. L. Tan, and H. Q. Gong, "Characterization of the polymerization of SU-8 photoresist and its applications in micro-electro-mechanical systems (mems)," *Polymer Testing*, vol. 20, no. 6, pp. 693–701, 2001.

[45] G.-B. Lee, C.-H. Lin, and G.-L. Chang, "Micro flow cytometers with buried SU-8/SOG optical waveguides," *Sensors and Actuators A: Physical*, vol. 103, no. 1-2, pp. 165–170, 2003.

[46] D. A. Chang-Yen and B. K. Gale, "An integrated optical oxygen sensor fabricated using rapid-prototyping techniques," *Lab on a Chip*, vol. 3, pp. 297–301, 2003.

[47] T. Deng, H. K. Wu, S. T. Brittain, and G. M. Whitesides, "Prototyping of masks, masters, and stamps/molds for soft lithography using an office printer and photographic reduction," *Analytical Chemistry*, vol. 72, no. 14, pp. 3176–3180, 2000.

Chapter 5

Absorption-based optical chemical sensors

5.1 Background

Absorption-based optical chemical sensors based on the colour change of a thin sensor film have been applied to the detection of various analytes including NH_3 [1, 2, 3, 4], CO_2 [5, 6, 7], chlorine [8], water vapour [9, 10, 11] and pH [12, 13, 14, 15]. The use of a thin film is attractive as it reduces sensor response time, can be more easily incorporated into miniaturized sensor systems via a variety of coating procedures, and requires less material for its fabrication when compared to bulk systems. This latter feature is important when dealing with expensive reagents or dyes for which synthesis is complicated or lengthy. Various optical configurations employing thin sensor films have been reported, including reflectance [16, 17], transmittance [3, 11, 18] and both fibre and planar waveguide-based devices employing evanescent-wave interrogation of the sensing layer [8, 9, 12, 19, 20]. Planar waveguides offer several advantages over fibre-based systems, including, for example, a more robust geometry and their compatibility with a wide variety of thin film coating procedures. These advantages have been detailed in Chapter 1 and make planar waveguide-based sensor platforms an ideal choice for the work reported here.

5.2 Planar platforms for absorption-based optical sensing

Fig. 5.1 depicts a generalised schematic of an optical absorption-based sensor platform in a planar configuration. A typical platform consists of a planar substrate, e.g., a glass microscope slide, coated with a thin, porous film that acts as the sensing layer. The porous nature of the film is critical to the operation of the sensor as changes in the optical absorption properties of the sensing layer are brought about by diffusion of the analyte into the layer. The resultant change in the optical absorption properties of the sensing layer is due to an analyte-sensitive indicator dye encapsulated within the layer. Such sensors are referred to as colorimetric in nature and are the primary focus of the optical absorption-based sensors studied here. However, the sensitivity enhancement strategy presented here (see Sec. 5.3) is also applicable to those sensors employing direct spectroscopy but only in the case where a thin analyte-permeable layer, coated onto a planar waveguide, is employed as an enrichment layer.

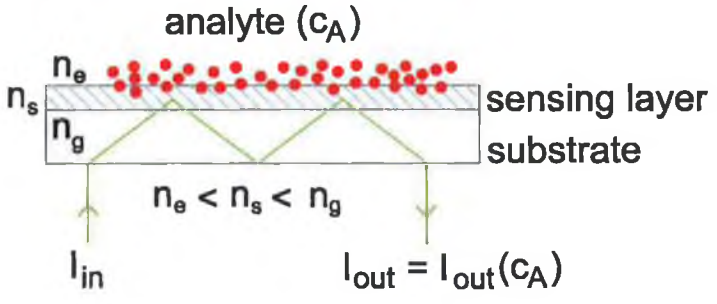

Figure 5.1: Generalised schematic of a planar optical absorption-based sensor platform employing a thin film sensing layer.

The sensing layer is interrogated by light of a suitable wavelength, i.e, from a source that is spectrally matched to the absorption band of the sensing layer. Therefore, changes in the optical absorption of the layer result in a modulation of the detected light intensity which is related to the analyte concentration, thereby providing the basis for the sensor.

It should be noted that, while Fig. 5.1 illustrates a waveguide based device where the interrogating light propagates along the platform, there are several other commonly employed optical configurations for absorption-based sensing and

these are described in the following section.

5.2.1 Commonly employed modes of interrogation

Transmittance

An example of a transmittance-based configuration is shown in Fig. 5.2. Light from a suitable source (depicted as a light emitting diode) is incident on the sensing layer from directly above, is transmitted through the sensing layer and substrate and is detected beneath the platform by a suitable detector, e.g., a photodiode.

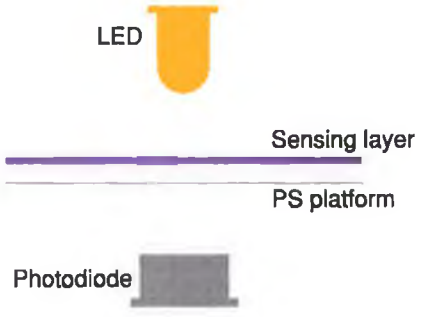

Figure 5.2: A typical transmittance-based configuration

It should be pointed out that the light source and photodetector illustrated here serve merely as examples and that any configuration employing a light source and photodetector positioned on opposite sides of the sample can be viewed as transmittance-based.

Transmittance-based configurations have been employed by several groups in the development of optical absorption-based sensors [3, 11, 18], their main advantage being the simplicity of the setup.

Reflectance

Another commonly employed configuration for colorimetric sensing platforms is reflectance-based, sometimes referred to as diffuse reflectance. A typical setup is illustrated in Fig. 5.3 where the light source and photodetector are again represented by a LED and photodiode, respectively.

In this case, both the light source and photodetector are positioned on the same side of the sample but at angles to one another so that light reflected from

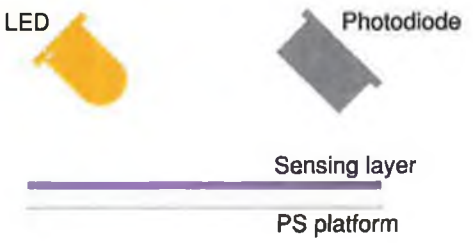

Figure 5.3: A typical reflectance-based configuration

the sensing layer is incident on the detector. This configuration is typically employed with the source and detector positioned directly above the sample. One major advantage of this setup is its potential to provide a relatively compact device due to the fact that all optoelectronic components are located on one side of the sample, something which is not possible when employing a transmittance-based configuration. It is, of course, desirable that the substrate be highly reflective at the interrogating wavelength, otherwise a significant fraction of the incident light will be transmitted through the sample, reducing the maximum detectable intensity, hence sensitivity. It is also worth noting that not all light detected interrogates the sensing layer to the same extent, some being reflected from its upper surface, thus reducing the sensitivity of the device.

A major disadvantage of both transmittance- and reflectance-based configurations is the fact that the interrogating light must propagate through the medium being analysed in order to interrogate the sensing layer. This results in the attenuation of the optical signal, which causes a reduction in the signal to noise ratio and, as a consequence, impacts adversely on sensor performance.

Evanescent wave-based optical sensing

The principle behind evanescent-wave-based optical sensing has been explained in detail in Chapter 2, Sec. 2.2.2. However, for completeness, a typical planar, evanescent-wave-based sensor platform is illustrated in Fig. 5.4

A planar waveguide acts as the substrate and is coated with a porous thin film that acts as the sensing layer. Here, the substrate is depicted as a multimode waveguide platform but the configuration is similar for a single mode waveguide. Light propagates along the waveguide by total internal reflection with an incident angle greater than the critical angle determined by the refractive indices of the

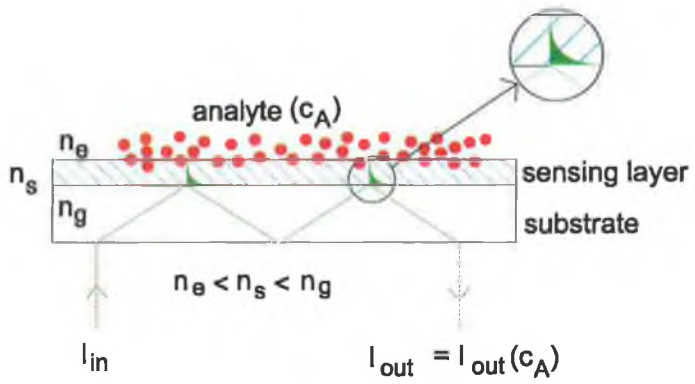

Figure 5.4: A typical evanescent-wave-based sensing platform in a planar configuration.

waveguide and sensing layer. The exponentially decaying evanescent field of the propagating light interrogates the sensing layer to a penetration depth that can be calculated from equation 2.35 assuming the refractive index of the waveguide is known (see Chapter 2, Sec. 2.2.2 for further details). This configuration has been extensively utilised in optical sensor development as it offers much improved sensitivity compared with transmittance and reflectance-based configurations while still employing a thin film as a sensing layer, thus reducing sensor response time.

Given that the penetration depth for a typical sol-gel thin film is on the order of $\sim 100\,\text{nm}$, it is clear that the evanescent wave may interrogate only a fraction of the sensing layer (depending on its thickness) and that its enhanced sensitivity is provided by means of multiple reflections from the sensing layer as the light is guided along the platform. This means that sensitivity is proportional to the length of the waveguide. However, this places restrictions on the size of the sensor platform as miniaturisation of the system results in decreased sensitivity. Simply scaling the platform down to retain the desired number of reflections (i.e., reducing the number of modes supported by the waveguide) is not an ideal solution either as this introduces the issue of coupling to smaller waveguides, which can impair the robustness of the system. This option also reduces the maximum input power of the sensor, thus reducing the signal to noise ratio (SNR).

There is clearly a need for sensor platforms that can form the basis of a robust, portable system without loss in sensitivity. The following section describes a strategy for the design of such a platform.

5.3 Sensitivity enhancement strategy

As shown in the previous sections, several optical configurations can be employed for the development of an absorption-based sensor. In each case, the sample comprises a thin sensing layer coated onto a planar substrate and this type of platform has formed the basis of an optical absorption-based sensor for a large variety of applications. However, little attention has been paid to the optimisation of platform sensitivity through analysis of the optical configuration.

Previous work involving an analysis of sensitivity optimisation for evanescent-wave sensors has been reported by Parriaux *et al.* [21]. Although a general formalism enabling the evaluation of optimum sensing conditions was presented, the subsequent analysis focused on monomode platforms employing evanescent-wave sensing. However, the complexity of such systems – arising from their restrictive coupling / alignment requirements – does not make them an attractive option for the development of low-cost, robust sensors.

The platforms developed by Suzuki *et al.* [22], Puyol *et al.* [23] and Qi *et al.* [24] (see Sec. 1.7.1), while demonstrating much improved sensitivity compared with conventional systems, employ complex fabrication protocols involving processes such as sputtering, LPCVD and RIE. Both the prism- and fibre-coupling strategies that are employed are incompatible with the development of mass-producible, robust sensors, further detracting from the versatility of these systems.

A sensitivity enhancement strategy for optical absorption-based sensors based on planar, multimode waveguides was developed by Lubos Polerecky, a former graduate student of the Optical Sensors Laboratory [25]. The objective was to apply this theory to the development of low-cost, robust and potentially mass-producible sensor platforms and the following section outlines the assumptions and predictions of this theoretical model. It should be noted that a complete description of this theoretical analysis is not within the scope of this work and readers should refer to [26] for further details as it forms a significant portion of Dr. Polerecky's doctoral work.

5.3.1 Theoretical model

Fig. 5.5 is a generalised representation of the sort of platform considered in this optimization procedure.

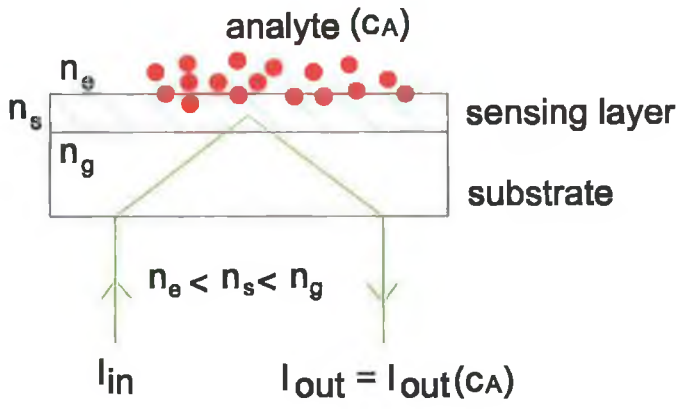

Figure 5.5: Schematic of sensor configuration under consideration.

It consists of an analyte-sensitive, colorimetric thin film of refractive index n_s coated on a planar substrate with refractive index n_g. The analyte under investigation is present in the superstrate environment (refractive index n_e) and diffuses into the sensing layer where it causes a change in the absorption coefficient, α_s, of the layer. The magnitude of the change in α_s is dependent on analyte concentration. Light from a source that is spectrally matched to the absorption maximum of the sensing layer is coupled into the substrate and interrogates the layer, after which it is outcoupled to an appropriate detector where its intensity is measured.

For the purposes of the theoretical analysis, the following refractive index condition is assumed:

$$n_e < n_s < n_g \tag{5.1}$$

The sensitivity of the device is defined as

$$S(c_A) = \mathrm{d}V/\mathrm{d}c_A \tag{5.2}$$

where V is the output signal measured by the detector and c_A is the analyte concentration. It is possible to quantify the variation of output signal with respect to the different optical parameters of the system by analysing the dependence of reflectivity (R) on these same parameters, and in particular on the angle θ at which the light interrogates the sensing layer. As mentioned previously, the

absorption coefficient of the layer (α_s) is dependent on analyte concentration. For these reasons, it is possible to examine the sensitivity in terms of the reflectivity and extinction coefficient of the sensing layer, R and γ_s,

$$\tilde{S}(\gamma_s) \equiv \mathrm{d}R/\mathrm{d}\gamma_s \tag{5.3}$$

where γ_s is related to α_s by the equation $\alpha_s = 4\pi\gamma_s/\lambda$, and λ is the wavelength of the interrogating light. The results of this theoretical analysis are represented by the solid line shown in Fig. 5.6 where the sensitivity is plotted against angle of incidence on the sensing layer with all other optical parameters remaining constant. The squares represent the data points acquired experimentally using a single reflection configuration in order to verify the theoretical predictions. This work is detailed in Chapter 6. In order to generate the solid curve, the optical parameters were assumed to be those of a typical sol-gel-derived sensing layer ($t \simeq 400\,\mathrm{nm}$, $n_s = 1.43$) coated on a planar glass substrate ($n_g = 1.515$) with air as the sensing environment ($n_e = 1.00$).

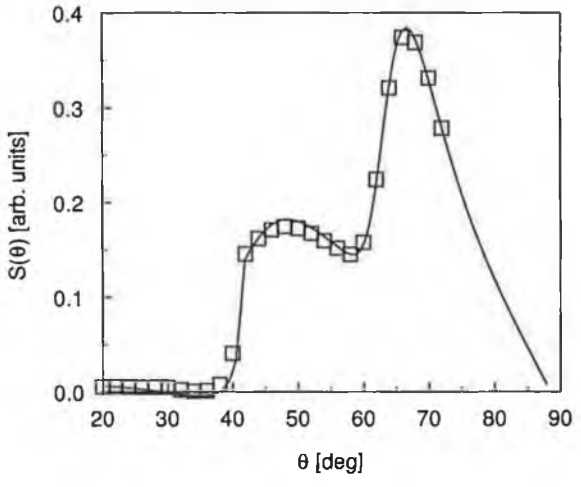

Figure 5.6: Dependence of sensitivity on angle of interrogation in a single reflection configuration.

There is clearly an optimum angle, θ_{opt}, at which sensitivity is maximum and, furthermore, this angle *does not* correspond to the region where the light is evanescent in the sensing layer ($\theta > 71°$). Rather, optimum sensitivity is achieved when the interrogating light is *propagating* in both the sensing layer and the substrate. This analysis was carried out under the assumption that the light source was monochromatic as in the case of a laser. For practical applications,

however, it is desirable to be able to use low-cost light sources, e.g., light emitting diodes (LED's), which have a broader bandwidth than lasers. A LED has an emission spectrum typically 50 nm wide but it can be shown that the function $\tilde{S}(\theta)$ (plotted in Fig. 5.6), when calculated for such a source is virtually unchanged from that calculated for a monochromatic source. This means that the analysis can be applied to the development of potentially low-cost sensing platforms.

The next stage in the development of this theoretical model was an investigation of the effect of multiple reflections, i.e., a waveguide-based configuration, on platform sensitivity when employing this enhanced mode of interrogation. Waveguide-based configurations commonly employ evanescent-wave interrogation of the sensing layer and generally exhibit a linear relationship between platform length (i.e., number of reflections) and sensitivity. It was decided to examine this relationship for an enhanced waveguide-based platform and, in the event of a non-linear sensitivity dependence, identify optimum sensing conditions. An outline of this analysis is presented in the following section.

5.3.2 Effect of multiple reflections on sensitivity

As mentioned in equation 5.2, the sensitivity can be defined as the change in output signal with respect to analyte concentration. In order to predict the effect of multiple reflections, i.e., platform interaction length, on sensitivity one must examine the nature of the the output signal, V. This signal is dependent on several parameters including the input power of the light source, coupling efficiencies of the sensor head (i.e., the fraction of light coupled into and out of the platform) and the efficiency with which the optical signal is converted to an electronic signal by the sensor electronics. It is assumed here that none of these parameters are influenced by changes in α_s, hence analyte concentration (c_A), as they are not dependent on the properties of the sensing layer. The output signal can, therefore, be written as:

$$V = \Gamma \mathcal{T}\left(c_A, L_{int}\right) + V_0 \tag{5.4}$$

where Γ represents those parameters that are independent of c_A, V_0 is a signal offset introduced by the electronics and $\mathcal{T}$ is the *attenuation factor* of the sensor platform, this quantity being dependent on both c_A and the interaction length,

L_{int}. Substituting Equation 5.4 into Equation 5.2, we can define the platform sensitivity as follows:

$$S(c_A) = \Gamma \frac{\mathrm{d}\mathcal{T}\left(c_A, L_{int}\right)}{\mathrm{d}c_A} \tag{5.5}$$

It is, therefore, the nature of $\mathcal{T}$ that dictates the dependence of sensitivity on L_{int}. It can be shown [26] that:

$$\mathcal{T} = \exp[-\gamma\left(c_A\right) L_{int}] \tag{5.6}$$

where the attenuation coefficient, $\gamma(c_A)$, is directly proportional to the absorption coefficient of the sensing layer, α_s. It is, therefore, possible to define sensitivity as:

$$S(c_A) = -\Gamma \xi L_{int} \tilde{S}_{(\alpha_s)} \exp\left[-\xi L_{int}\right] \tag{5.7}$$

where the relative sensitivity, $\tilde{S}_{\alpha_S}$, of the sensing layer is given by Equation 5.8

$$\tilde{S}_{\alpha_s} = \frac{1}{\alpha} \frac{\partial \alpha}{\partial c_A} \tag{5.8}$$

and the parameter ξ is directly proportional to α_s. An explanation of the exact nature of ξ is not within the scope of this thesis and readers should refer to [26] for its complete derivation.

From the presence of the term ξL_{int} in equation 5.7 it is clear that the sensitivity of the platform increases with interaction length provided the argument of the exponential term remains sufficiently small. This is due to the fact that, for low values of ξL_{int}, the exponential term is approximately equal to 1. However, the model summarized in equation 5.7 also shows that sensitivity will begin to decrease exponentially given a sufficiently long interaction length or sufficiently high absorption coefficient. These findings are illustrated in figure 5.7, which shows the relationship between sensitivity and interaction length for various extinction coefficients of the sensing layer when the interrogating light is incident on the layer at the optimum angle of incidence, θ_{opt}, determined from the theoretical analysis [26]. In this case, $t_s = 800\,\mathrm{nm}$ and the values of all other optical parameters remain unchanged from those used to generate the results shown in figure 5.6.

The graph shows sensitivity increasing with interaction length up to a critical interaction length, L_c, after which it decreases exponentially. The value of L_c is dependent on the absorption coefficient of the sensing layer, with highly absorbing

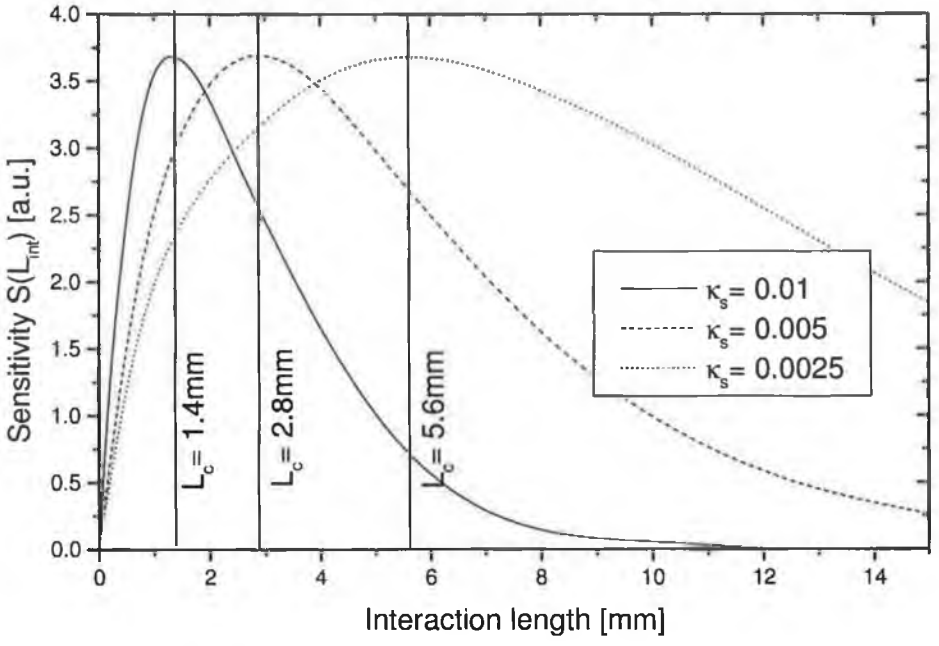

Figure 5.7: Predictions of theoretical model

layers having the shortest L_c. The obvious implication of this theory is that a higher number of reflections (i.e., a longer waveguide) does not guarantee greater sensitivity when employing this optimized mode of interrogation. It was the aim of this work to investigate experimentally the trade-off between α_s and L_{int} in order to determine an optimized combination of the two, thus fully exploiting the sensitivity enhancement offered by this mode of interrogation and highlighting the required platform design for optimum sensitivity. The results of this investigation and their agreement with theoretical predictions are detailed in Chapter 7, Sec. 7.3 which describes the performance of an optical pH sensor employing a colorimetric sol-gel-derived thin film.

5.4 Conclusions

Optical absorption-based sensors have been used for the detection of a variety of chemical species by employing any one of several different optical configurations. The focus of this work is on reagent-based sensors employing planar substrates that have been coated with a dye-doped thin film that acts as the sensing layer.

Certain recently developed platforms [22, 23, 24] have demonstrated enhanced

sensitivity over those employing more conventional optical configurations but the complex nature of these devices along with their lengthy, complicated fabrication makes them unsuitable for mass production or field use.

A theoretical analysis has been developed that highlights the possibility of enhanced sensitivity through careful choice of the relevant optical parameters including the angle of incidence on the sensing layer, the absorption-coefficient of the layer and the interaction length of the interrogating light with the layer. Furthermore, this analysis can be applied to the development of low-cost, robust and potentially disposable sensor platforms whose fabrication is potentially far less time consuming and complex than those mentioned previously. This analysis has major implications for the design of mass-producible, yet highly sensitive sensor platforms for optical absorption-based sensing applications.

Bibliography

[1] R. Klein and E. Voges, "Integrated-optic ammonia sensor," *Sensors and Actuators B-Chemical*, vol. 11, no. 1-3, pp. 221–225, 1993.

[2] T. Butler, T. Grady, B. D. MacCraith, D. Diamond, and M. A. McKervey, "Optical sensor for gaseous ammonia with tuneable sensitivity," *The Analyst*, vol. 008, pp. 803–806, 1997.

[3] M. Trinkel, W. Trettnak, F. Reininger, R. Benes, P. Oleary, and O. S. Wolfbeis, "Study of the performance of an optochemical sensor for ammonia," *Analytica Chimica Acta*, vol. 320, no. 2-3, pp. 235–243, 1996.

[4] T. Werner, I. Klimant, and O. Wolfbeis, "Ammonia-sensitive polymer matrix employing immobilized indicator ion pairs," *Analyst*, vol. 120, pp. 1627–1631, 1995.

[5] H. N. McMurray, "Novel thin optical film sensors for the detection of carbon dioxide," *J. Mater. Chem.*, vol. 2, no. 4, pp. 401–406, 1992.

[6] B. Weigl, A. Holobar, N. Rodriguez, and O. Wolfbeis, "Chemically and mechanically resistant carbon dioxide optrode based on a covalently immobilized pH indicator," *Analytica Chimica Acta*, vol. 282, pp. 335–343, 1993.

[7] A.Mills and Q. Chang, "Tuning colourimetric and fluorimetric gas sensors for carbon dioxide," *Analytica Chimica Acta*, vol. 285, pp. 113–123, 1994.

[8] C. Piraud, E. Mwarania, G. Wylangowski, J. Wilkinson, K. Odwyer, and D. J. Schiffrin, "Optoelectrochemical thin-film chlorine sensor employing evanescent fields on planar optical wave-guides," *Analytical Chemistry*, vol. 64, no. 6, pp. 651–655, 1992.

[9] S. Saavedra, P. Skrdla, N. Armstrong, S. Mendes, and N. Peyghambarian, "Sol-gel based planar waveguide sensor for water vapour," *Analytical Chemistry*, vol. 71, no. 7, pp. 1332–1337, 1999.

[10] P. J. Skrdla, N. R. Armstrong, and S. S. Saavedra, "Starch-iodine films respond to water vapor," *Analytica Chimica Acta*, vol. 455, no. 1, pp. 49–52, 2002.

[11] P. R. Somani, A. K. Viswanath, R. C. Aiyer, and S. Radhakrishnan, "Novel dye+solid polymer electrolyte material for optical humidity sensing," *Organic Electronics*, vol. 2, no. 2, pp. 83–88, 2001.

[12] S. Saavedra and L. Yang, "Chemical sensing using sol-gel derived planar waveguides and indicator phases," *Analytical Chemistry*, vol. 67, no. 8, pp. 1307–1314, 1995.

[13] Z. Jin., Y. Su., and Y. Duan., "An improved optical pH sensor based on polyaniline," *Sensors and Actuators B*, vol. 71, no. 1-2, pp. 118–122, 2000.

[14] J. Lin and D. Liu, "An optical pH sensor with a linear response over a broad range," *Anal. Chim. Acta.*, vol. 408, pp. 49–55, 2000.

[15] L. Pascual and M. Villegas, "Sol-gel silica coatings doped with a pH-sensitive chromophore," *Thin Solid Films*, vol. 351, pp. 103–108, 1999.

[16] Y. Sadaoka, M. Matsuguchi, Y. Sakai, and Y. uki Murata, "Optical humidity sensing characteristics of nafion–dyes composite thin films," *Sensors and Actuators B: Chemical*, vol. 7, no. 1-3, pp. 443–446, 1992.

[17] F. A., A. Matias, M. M. D. C. Vila, and M. Tubino, "A simple device for quantitative colorimetric diffuse reflectance measurements," *Sensors and Actuators B: Chemical*, vol. 88, no. 1, pp. 60–66, 2003.

[18] A. S. Jeevarajan, S. Vani, T. D. Taylor, and M. M. Anderson, "Continuous pH monitoring in a perfused bioreactor system using an optical pH sensor," *Biotechnology and Bioengineering*, vol. 78, no. 4, pp. 467–472, 2002.

[19] C. R. Lavers, K. Itoh, S. C. Wu, M. Murabayashi, I. Mauchline, G. Stewart, and T. Stout, "Planar optical waveguides for sensing applications," *Sensors and Actuators B-Chemical*, vol. 69, no. 1-2, pp. 85–95, 2000.

[20] E. Scorsone, S. Christie, K. C. Persaud, P. Simon, and F. Kvasnik, "Fibre-optic evanescent sensing of gaseous ammonia with two forms of a new near-infrared dye in comparison to phenol red," *Sensors and Actuators B-Chemical*, vol. 90, no. 1-3, pp. 37–45, 2003.

[21] G. Veldhuis and O. Parriaux, "Normalized analysis for the sensitivity optimization of integrated optical evanescent-wave sensors," *Journal of Lightwave Technology*, vol. 16, no. 4, pp. 573–582, 1998.

[22] K. Suzuki and H. Hisamoto, "Ion–selective optodes: current developments and future prospects," *Trends in Analytical Chemistry*, vol. 18, no. 8, pp. 513–524, 1999.

[23] M. D. Valle, M. Puyol, I. Garces, F., Villuendas, C. Dominguez, and J. Alonso, "Integrated waveguide absorbance optode for chemical sensing," *Analytical Chemistry*, vol. 71, no. 22, pp. 5037–5044, 1999.

[24] Z. M. Qi, A. Yimit, K. Itoh, M. Murabayashi, N. Matsuda, A. Takatsu, and K. Kato, "Composite optical waveguide composed of a tapered film of bromothymol blue evaporated onto a potassium ion-exchanged waveguide and its application as a guided wave absorption-based ammonia-gas sensor," *Optics Letters*, vol. 26, no. 9, pp. 629–631, 2001.

[25] L. Polerecky, C. S. Burke, and B. D. MacCraith, "Optimization of absorption-based optical chemical sensors that employ a single-reflection configuration," *Applied Optics*, vol. 41, no. 15, pp. 2879–2887, 2002.

[26] L. Polerecky, *Optimisation of multimode waveguide platforms for optical chemical sensors and biosensors.* Ph.D. Thesis, Dublin City University, 2002.

Chapter 6

Development of enhanced platforms for absorption-based optical chemical sensors

The enhancement principles described in Chapter 5 provide a clear design strategy for the development of absorption-based optical chemical sensors, providing interrogation of the sensing layer at the optimum angle of incidence predicted by the theoretical model. This chapter describes the experimental verification of this model along with the subsequent development of an enhanced prototype sensor unit.

6.1 Experimental verification of theoretical model

6.1.1 Experimental setup

A schematic of the experimental setup employed to verify the theoretical predictions of Chapter 5 is shown in Fig. 6.1.

The objective of this setup was to enable the angular dependence of the reflectivity of a thin sensing layer to be recorded. From this it would then be possible to calculate the angular profile of the sensitivity. In order to acquire data over the angular range specified in Fig. 5.6, a BK7 glass slide ($n_g = 1.515$) was attached to a semi-cylindrical prism of the same material using a commercially available immersion liquid. Glass slides were obtained from SI Cell International Ltd., U.K..

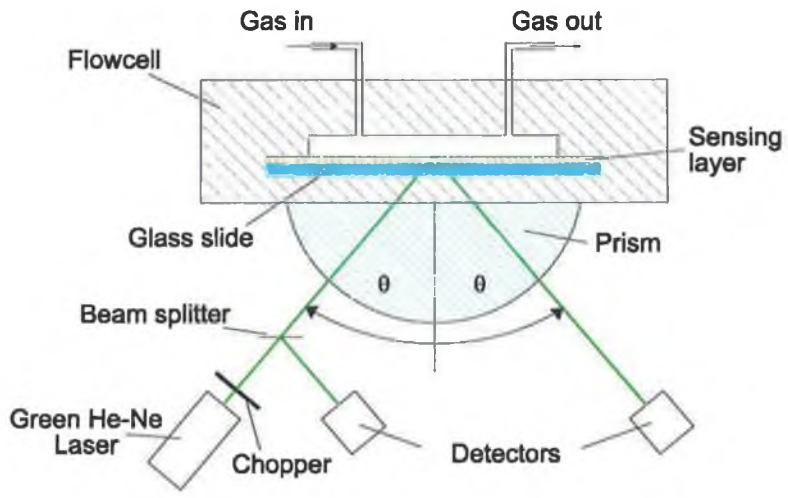

Figure 6.1: Experimental setup for verification of theoretical model.

The dimensions of the prism were such that the addition of the glass slide resulted in a perfect semi-cylinder. The glass slide was coated with a thin sol-gel-derived sensing layer, the preparation of which is described in Sec. 6.1.2. This element was then incorporated into a flowcell which enabled a controlled flow of gaseous test analyte to be passed above the sensing layer.

Gas delivery was achieved using mass flow controllers (UFC-1100 series, Celerity, Dublin) which facilitated precise regulation of analyte and carrier gas concentrations. In this case, it was decided to employ ammonia as the analyte gas with nitrogen as the carrier. The gas delivery setup consisted of two separate lines, one connected to a cylinder containing pure nitrogen, the other connected to a supply of 1% ammonia in nitrogen. These two lines were mixed prior to their delivery to the flowcell. Ammonia was chosen due to the fact that it is a common target analyte for optical absorption-based sensing applications and is easily detected using an appropriate colorimetric pH indicator dye. The flowcell and sensor element assembly was attached to a motorised rotary stage (Physik Instrumente, M-038, unidirectional repeatability 20μrad) permitting the variation of the incident angle within the region of $\theta \in \langle 20°, 75° \rangle$. This rotary stage was controlled by LabVIEW software.

The light source used was a green He-Ne laser ($\lambda = 543.5\,\text{nm}$), the emission wavelength of which lies within the absorption band of the indicator dye in its deprotonated state as shown in Fig. 6.2. Light from the laser was incident on the

sensing layer at the selected angle and the reflected beam was detected by a Si-photodiode. To compensate for laser intensity fluctuations, a beam splitter was used to send a reference beam to another photodiode. This reference signal was then used to eliminate the effect of laser intensity fluctuations on sensor output by employing a ratiometric analysis of the output and reference signals. The detection circuit contained a lock-in amplifier referenced by a mechanical light-chopper. Consequently, the detected output intensity I_{out} was independent of the ambient light level. The primary photodiode was mounted on a custom-made arm that was in turn attached to a stepper motor. This motor was also controlled by LabVIEW software so that for every angle of incidence, θ_i, determined by the motion of the rotary stage, the detector was automatically positioned to measure the intensity of the reflected beam at an angle equal to $2\theta_i$.

6.1.2 Preparation of sensing layer

The layer used was a sol-gel-derived thin film doped with Bromocresol Purple (BCP) [1]. BCP is a pH indicator dye with an absorption band displaying a maximum at $\approx 590\,\text{nm}$ corresponding to its deprotonated state. A typical sol was prepared by dissolving 30 mg BCP in 4 g of ethanol and then adding 2 g pH 1 HCl and 6 g tetraethoxysilane (TEOS) whilst stirring. This results in an R-value of 3.86. The sol was allowed to stir for 1 hour and then aged at room temperature for 24 hours before deposition. The thin film was deposited by dip-coating the sol on one side of the glass slide at a speed of 1 mm/s, which produced a uniform layer of thickness $t_s \approx 0.4\,\mu\text{m}$ as measured by profilometry. Following this, the film was oven-dried at 70°C for 17 hours. All samples were stored under ambient conditions for three weeks before use. The UV-Vis absorption spectra of a typical sensing layer in its protonated and deprotonated forms are shown in Fig. 6.2.

The setup described above was used to record the angular dependence of the reflectivity of a typical sensor platform when exposed to 100% N_2 (corresponding to a protonated sensing layer) and a mixture of 1%NH_3 in N_2 with N_2 (corresponding to a deprotonated sensing layer, see Sec. 6.3.2). The results are described in the following section.

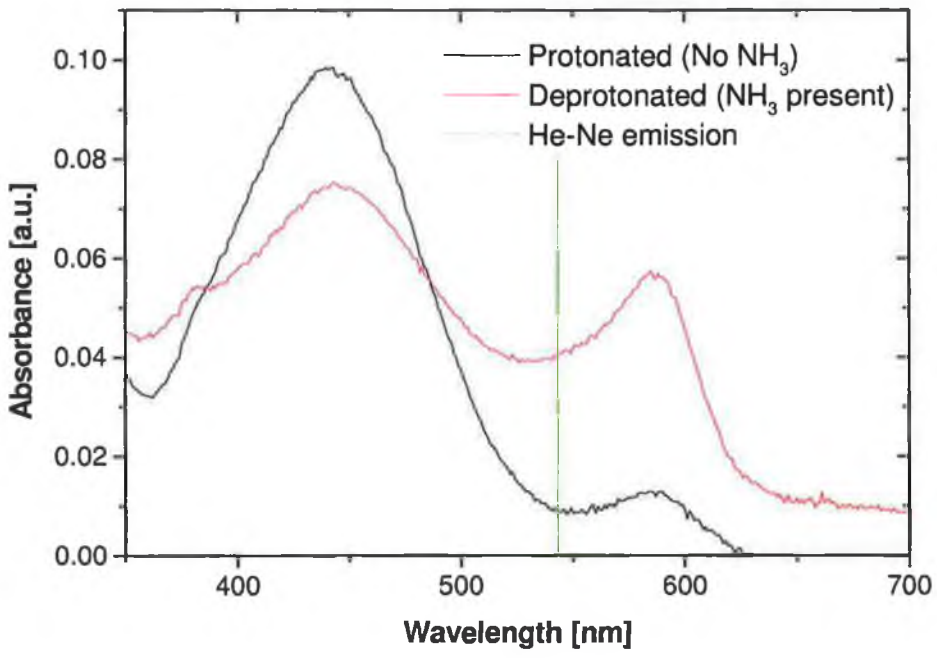

Figure 6.2: Absorption spectra of a typical sensing layer.

6.2 Results

Fig. 6.3(a) shows the angular distribution of the reflectivity $R(\theta)$ of the sensing element specified above for two concentrations of NH_3 in N_2, $c_{A1} = 0\,\text{ppm}$ ($\times$) and $c_{A2} = 2\,\text{ppm}$ ($\circ$). Fig. 6.3(b) shows the corresponding sensitivity S calculated as $S = (R[c_{A1}] - R[c_{A2}])$. Solid lines in both graphs correspond to the theoretical curves which were obtained from the model described in Chapter 5, Sec. 5.3.1. Both the experimental data and the theoretical curves were obtained for TE polarised light.

Clearly, the agreement between the experimental data and the theoretical curves was very good. In accordance with the predictions of the theoretical analysis, the experimental data demonstrated the existence of a significant peak in the sensor sensitivity at the incident angle $\theta \approx 65°$. At this angle, which corresponds to the mode of operation where the electromagnetic field is propagating in both the sensing layer and substrate (ie., propagating as a cover radiation mode), the sensitivity (shown in Fig. 6.3(b)) is significantly greater than in the region corresponding to the evanescent mode of the sensor operation (i.e., for $\theta > \theta_c^{sg} \approx 70.7°$).

Having established the validity of the theoretical analysis it was decided to

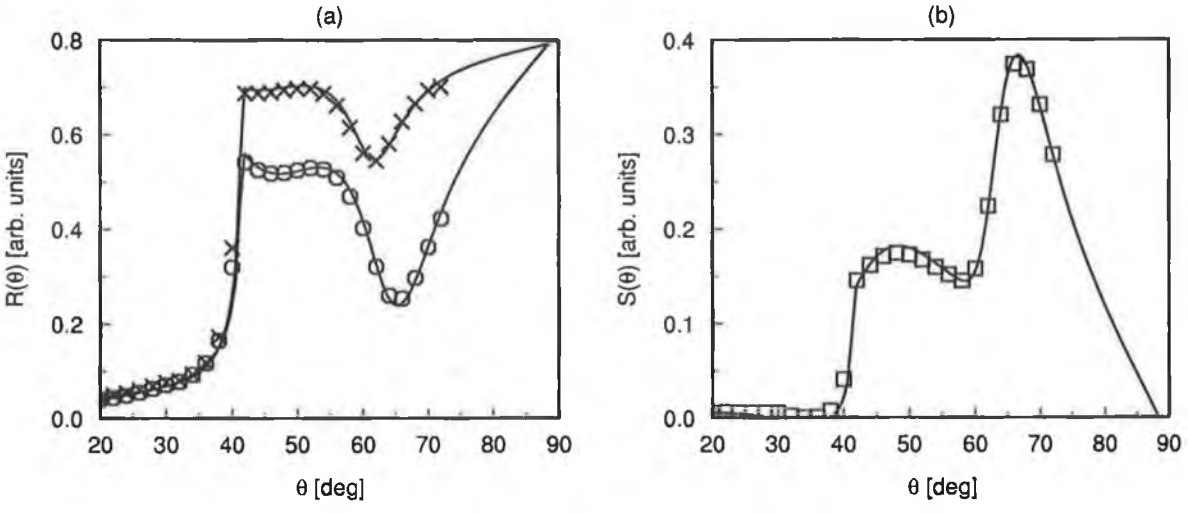

Figure 6.3: (a) Angular distributions of reflectivity obtained by the experimental set-up shown in Fig. 6.1. The experimental data correspond to the ammonia concentrations of 0 ppm (×) and 2 ppm (○), respectively. The sensitivity shown in graph (b) was calculated as a difference $R[c_{A1}] - R[c_{A2}]$. In both graphs, solid lines correspond to the fits of the experimental points by the theoretical model.

progress to the development of a more compact and cost-effective laboratory prototype.

6.3 Development of LED-based prototype sensor

6.3.1 Setup

The results presented in Sec. 6.2 demonstrated that, for the sensing configuration used, it was possible to achieve a significant optimisation of sensor response in a single reflection configuration. Furthermore, as mentioned in Chapter 5, Sec. 5.3.1, the function $\tilde{S}(\theta)$ does not change significantly if a LED is used as a light source. Consequently, a prototype sensor unit incorporating these features was designed, as shown in Fig. 6.4.

The core feature of the unit was a metal head which provided a rigid support for the LED and Si-photodiode. The orientations of the LED and detector were selected to ensure that the light interacted with the sensing layer at the optimum

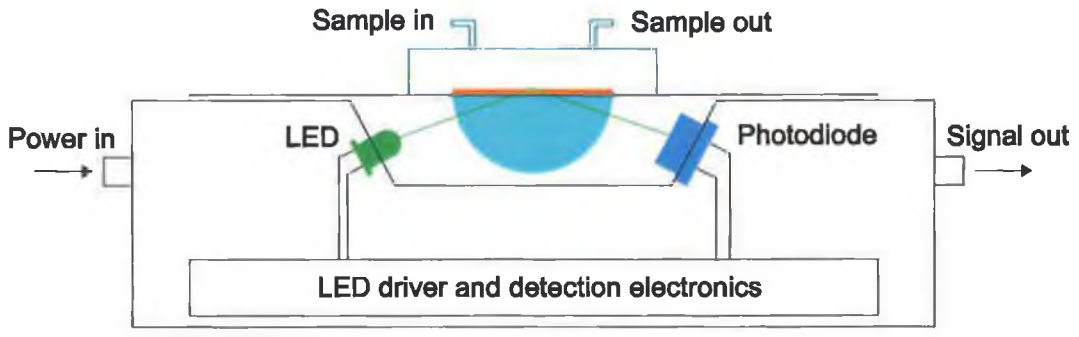

Figure 6.4: Schematic of single-reflection LED-based prototype sensor.

incident angle. Furthermore, the dimensions of the LED and detector apertures (see Fig. 6.4) were designed so as to allow only light within a narrow angular emission range (approximately 8°) to interrogate the sensing layer and be detected by the detector. The orientations of both the LED and the detector were chosen so as to ensure that the peak angle of interrogation corresponded to the point of maximum sensitivity obtained from Fig. 6.3(b), i.e., $\theta_{max} = 65°$. It can be seen from this graph that, due to the angular output of the LED, light is not incident solely in the region of optimum sensitivity but also in a region where sensitivity decreases to approximately half of its maximum value. This results in a reduction of the maximum achievable sensitivity, but further optimisation is possible by reducing the diameter of the LED aperture so as to decrease this angular breadth (see Chapter 7, Sec. 7.2.2).

The optoelectronic components were connected to a circuit which modulated the signal of the LED using an ICM555 timer chip. The modulation frequency served as the reference for an AD630 chip operating in lock-in mode which facilitated lock-in detection of the outcoupled light intensity by the photodiode (see appendix D an illustration of the circuit diagram). This signal was then recorded on a PC using LabVIEW software which plotted the signal intensity as a function of time (the LabVIEW VI is included in appendix C).

The sensor unit was assembled by attaching the box containing the electronic circuit, the metal holder containing the LED and photodiode, and a flow cell containing the sensing element and gas inlet and outlet. In the case of aqueous environments, a PDMS flow cell replaced the aluminium cell used for gas sensing applications. The flowcell was fabricated by casting PDMS against a metal disc

1 mm thick, with a diameter of 1 cm (see Chapter 4, Sec. 4.1.1 for a description of PDMS casting). The power was supplied externally by a standard, commercially available power source (SN16a, B&O power supplies, Denmark).

6.3.2 Performance of prototype sensor

The response of the sensor unit in both aqueous and gaseous environments was investigated. The sensing layer was identical for both sets of experiments.

Response to gaseous ammonia

The NH_3 sensing mechanism is outlined below. Equation 6.1 illustrates the first stage, i.e., the diffusion of gaseous NH_3 into the sensing layer and the solvation of NH_3 by water to form ammonium hydroxide.

$$NH_3(gas) + H_2O \leftrightarrow NH_4^+OH^- \tag{6.1}$$

The indicator dye is then deprotonated by ammonium hydroxide, producing a modified (deprotonated) form of the dye with water as a by-product.

$$NH_4^+OH^- + H^+Dye^- \leftrightarrow NH_4^+Dye^- + H_2O \tag{6.2}$$

This sensing mechanism is reversible with the modified dye compound regenerating the primary dye and ammonia.

$$NH_4^+Dye^- \leftrightarrow H^+Dye^- + NH_3(gas) \tag{6.3}$$

Fig. 6.5 shows the absorption spectrum of the BCP-doped sol-gel layer in its deprotonated state along with the emission spectrum of the green LED (Radionics) employed in the sensor head. The absorption band of the layer displays maximum absorbance at $\lambda_{abs} = 587$nm which matches up well with the LED emission ($\lambda_{max} = 570$nm). The large overlap between the two spectra demonstrates the suitability of the LED as a light source for this application.

The response of the sensor to varying concentrations of NH_3 in nitrogen is illustrated in Fig. 6.6. Gas delivery was achieved using a setup identical to that described in Sec. 6.1. The concentration was varied from 0 ppm NH_3 to 12 ppm NH_3 and the sensitivity of the device to lower concentrations is evident.

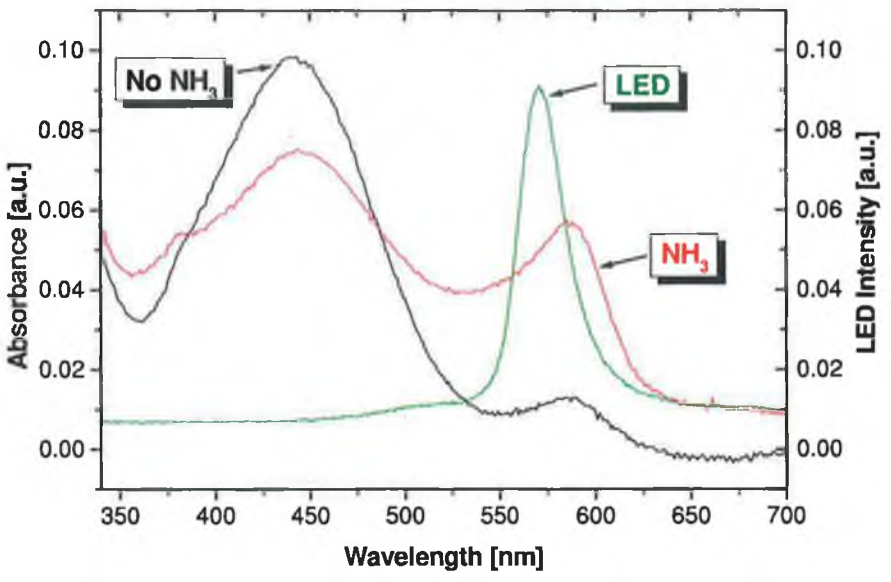

Figure 6.5: Absorption spectrum of sensing layer and LED emission spectrum.

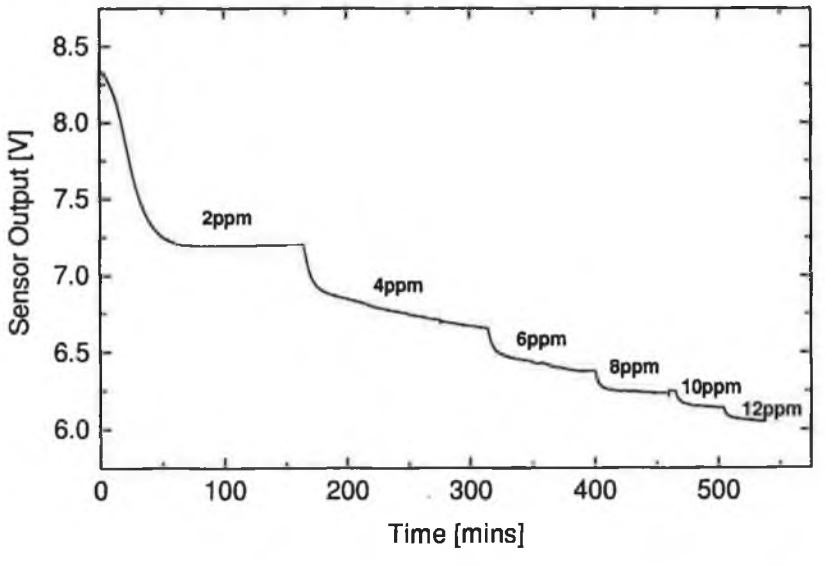

Figure 6.6: Sensor response to various NH_3 concentrations.

The response time of the system is clearly longer than desirable and this is thought to be due to the complex nature of the chemical kinetics involved in the sensing reaction. This aspect of sensor performance is examined in greater detail in Chapter 7, Sec. 7.2.3. The sensitivity provided by the optimised configuration was of greater interest at this point.

Fig. 6.7 shows a calibration curve based on the sensor response, with the inset illustrating sensor resolution. With this typical non-linear response, the greatest resolution is achieved at low ammonia concentrations (< 2 ppm). The calibration curve yields a LOD of 10 ppb, with a 3σ noise level of $= 0.0045$ V. At higher concentrations (6–12 ppm) the sensor resolution increases by a factor of approximately 30 due to the fall-off in sensitivity.

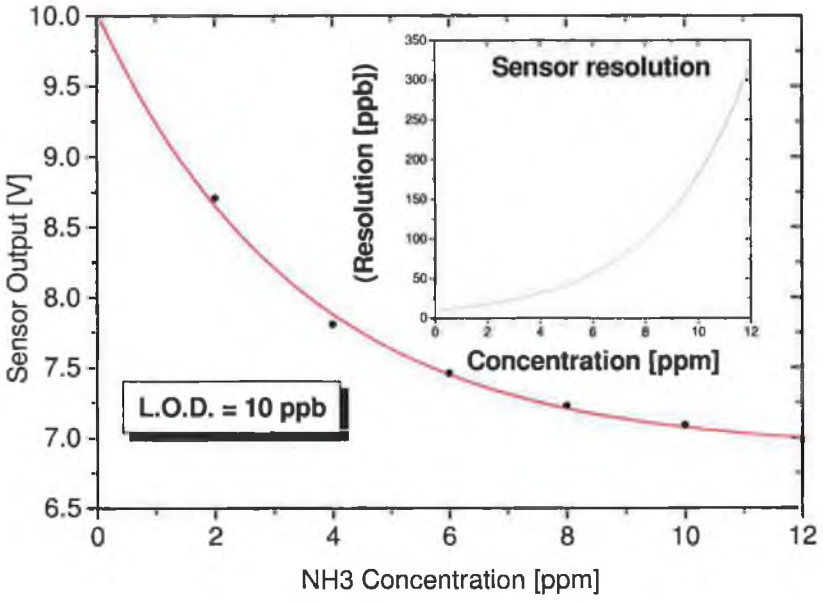

Figure 6.7: Sensor calibration curve.

The significance of these data becomes apparent when compared with published results [2] where a more complex, multiple-reflection fibre-based system is employed. A LOD in the ppb range is inferred in this work and this corresponds to the value obtained with the optimised, single-reflection system presented here. The sensor developed by Qi *et al.* [3] which is based on a tapered film of bromothymol blue deposited on a PIE waveguide does yield a lower LOD than the single-reflection configuration presented here. However, as stated in Sec. 6.3.1, a reduction in the angular divergence of the LED would further improve the sen-

sitivity of this configuration and, in terms of ease of fabrication and coupling strategy, the single reflection configuration is an improvement on that work.

Response to pH buffer solutions

pH buffer solutions were prepared by dissolving a sachet of the desired buffer powder (Hydrion Buffer, Aldrich) in 500 ml of de-ionised water and stirring until dissolved. These solutions were then passed over the sensing layer using a PDMS flowcell connected to a peristaltic pump.

Fig. 6.8 shows the response of the sensor unit to various buffer solutions with pH values ranging from pH5 to pH11.

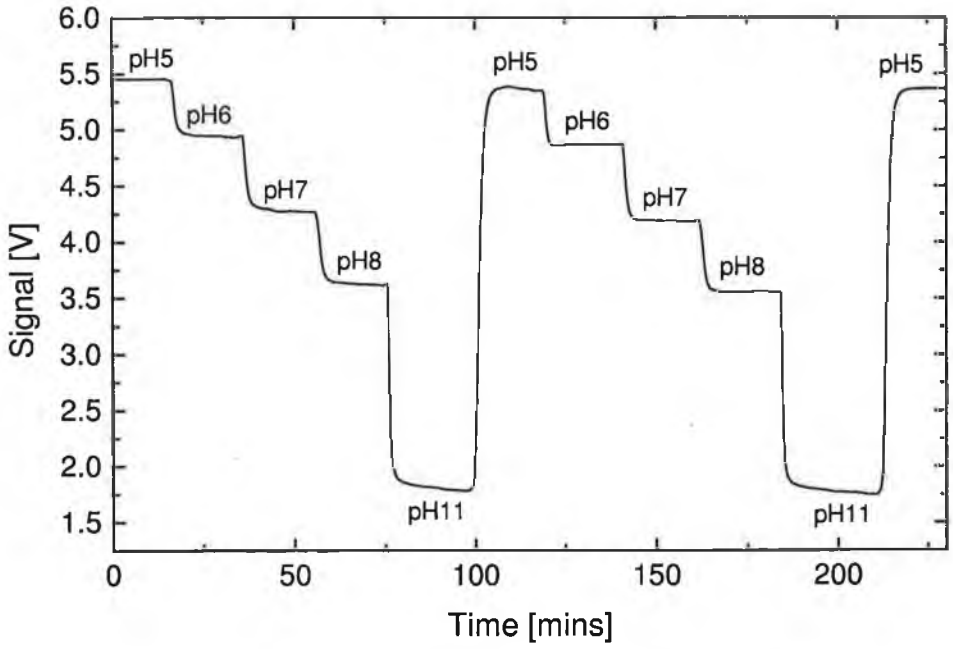

Figure 6.8: pH response of sensor platform.

The sensor output voltage varied from approximately 5.45 V (for pH5) to 1.80 V (for pH11). This is quite a broad pH range for an indicator dye of the sulfonephthalein family. The dynamic range of such a dye would typically be 3-4 pH units. However, past work [4] has shown that Bromocresol purple has an extended range compared with other dyes of its family, e.g. Bromocresol green or Bromothymol blue. However, pH 11 is at the limit of the dynamic range of BCP so, for the purposes of calculating sensor resolution, the response from pH5 to pH8 was examined. Taking into account the device sensitivity and a 3σ noise

level of = 0.0045 V yields a resolution of approximately 0.007 pH units over this range.

This result, which was achieved with a LED-based single-reflection prototype sensor system, compares favourably with the performance of a previously published optical fibre-based sensor system employing evanescent wave absorption [5]. In that case, a resolution of 0.025 pH units was achieved with an evanescent wave interaction length of approximately 5 cm.

6.4 Conclusions

In this chapter, the theoretical predictions that form the basis of the sensitivity enhancement strategy presented in Chapter 5, Sec. 5.3.1 were verified experimentally using a laser-based system employing a sol-gel derived layer deposited on a glass-slide.

The excellent agreement between theory and experimental data prompted the design and fabrication of a compact LED-based prototype sensor system. Its performance was tested in both aqueous and gaseous environments. Although the sensor system employed only a single-reflection configuration, its performance compared favourably with previously reported more complex sensor systems. For example, a resolution of approximately 0.007 pH units in the range of pH5–pH8, and a 10 ppb limit of detection of gaseous ammonia in N_2 were achieved.

It is also important to note that the approach to optimisation discussed in this article is only relevant to situations where surface-fouling and variations in the thickness of the sensing layer are not of significance. Otherwise, the spatial confinement of the evanescent wave within the sensing layer offers a clear advantage. Nevertheless, the theoretical analysis along with the experimental results obtained clearly provide a basis for the development of a low cost yet very sensitive absorption-based optical sensor system.

The following chapter describes the progression from a glass-based sensing element to a potentially disposable, mass-producible polymer sensor platform, while continuing to exploit the optimisation strategy that was verified in this chapter.

Bibliography

[1] F. J. Green, *The Sigma Aldrich Handbook of Stains, Dyes and Indicators.* Milwaukee, Wisconsin: Aldrich Chemical Company, Inc., 1990.

[2] R. Klein and E. Voges, "Integrated-optic ammonia sensor," *Sensors and Actuators B-Chemical*, vol. 11, no. 1-3, pp. 221–225, 1993.

[3] Z. M. Qi, A. Yimit, K. Itoh, M. Murabayashi, N. Matsuda, A. Takatsu, and K. Kato, "Composite optical waveguide composed of a tapered film of bromothymol blue evaporated onto a potassium ion-exchanged waveguide and its application as a guided wave absorption-based ammonia-gas sensor," *Optics Letters*, vol. 26, no. 9, pp. 629–631, 2001.

[4] T. Butler, *Development of evanescent wave pH sensors based on coated optical fibres.* Ph.D. Thesis, Dublin City University, 1996.

[5] T. Butler, B. MacCraith, and C. McDonagh, "Development of an extended range fiber optic pH sensor using evanescent wave absorption of sol-gel entrapped pH indicators," in *Chemical, Biochemical, and Environmental Fiber Sensors VII* (A. V. Scheggi, ed.), vol. 2508, pp. 168–178, Proc. of SPIE, 1995.

Chapter 7

Development of enhanced polymer waveguide platforms for absorption-based optical chemical sensing

The results presented in the previous chapter clearly demonstrate the feasibility of developing highly sensitive platforms for absorption-based optical chemical sensing applications by implementing the findings of the theoretical model presented in Chapter 5 in the design of the sensor platform. However, the use of the single reflection configuration described in Chapter 6 was intended merely as a proof of principle system that demonstrated the sensitivity enhancement predicted by theory. It was not the aim of the work at that point to develop mass-producible sensor platforms (as evidenced by the use of a glass slide and semi-cylindrical prism as the sensing element).

The subsequent stage in this work and one of its primary goals was the development of mass-producible, disposable sensor platforms that demonstrated enhanced sensitivity. It was also decided to extend the interrogation of the sensing layer from a single reflection to multiple reflections in order to examine the performance enhancement provided by an increased number of reflections. The identification of optimised conditions when employing a multiple reflection configuration for which sensitivity is maximised is also a crucial element of this

implementation and the theoretical analysis outlined in Chapter 5, Sec. 5.3.2 provided a starting point for this work.

This chapter describes the design and fabrication of polymer waveguide platforms according to the enhancement strategy described in Chapter 5. Initially, these platforms were coated with an ammonia-sensitive sol-gel layer and the resultant sensor response was examined and compared with previously developed systems. It was then decided to investigate the accuracy of the theoretical predictions made concerning the effect of sensor interaction length on device sensitivity. The model system chosen for this stage was that of optical pH sensing.

7.1 Design and fabrication of enhanced polymer waveguide platforms

One of the primary aims of this work was to develop mass-producible, disposable platforms that exploit the sensitivity enhancement provided by a multiple reflection configuration. It was decided to produce the sensing platforms with polymer processing technology, because of the wide range of low-cost, optical polymers available along with several manufacturing technologies which could be employed to produce the desired chips.

A schematic of the design developed by us for waveguide platforms that facilitate the enhanced interrogation of a thin sensing layer is shown in Fig. 7.1. The most important features of this design are the two refractive optic elements at either end which facilitate coupling of the light into and out of the waveguide at the appropriate angle. These couplers ensure that light incident perpendicularly on their angled faces interrogates the sensing layer at the desired optimum angle, the value of which is dependent on several parameters including the refractive indices of the waveguide, sensing layer and environment. It is important to note that the waveguide chip is a *single unit* and the integrated refractive elements should not be confused with prism couplers. It is evident from the schematic that only the region of the platform between the refractive couplers is involved in sensor operation. The portions at either end of the platform are included for ease of handling and incorporation into a custom made sensor head (see Sec. 7.2.2).

Injection moulding was the fabrication method chosen as it is a well estab-

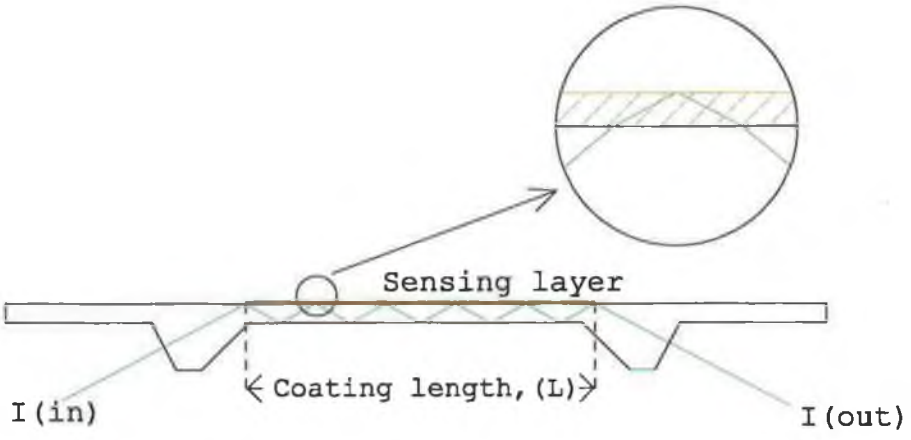

Figure 7.1: Schematic of polymer waveguide platform.

lished, high throughput technique for which there are a wide range of optical quality polymers available. For the purposes of injection moulding it is necessary to fabricate a mould of the required dimensions in order to produce the polymer waveguide chips. This mould was designed using a commercially available CAD/CAM software package (XCAD, X-NC, U.K.). Fig. 7.2(a) illustrates the completed design for the waveguide mould, while Fig 7.2(b) is a 3D preview of the machined part.

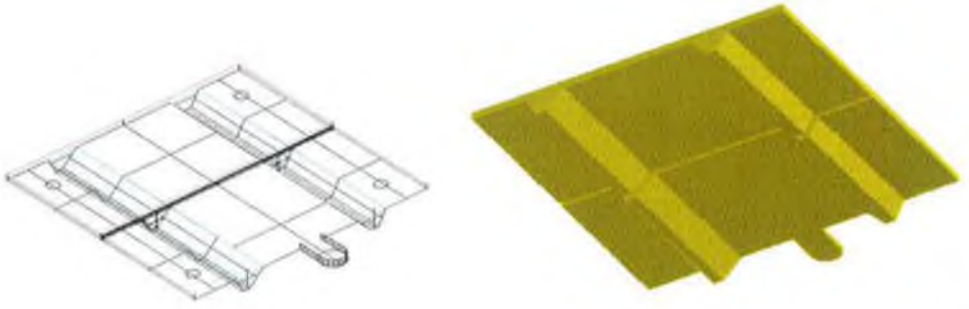

Figure 7.2: (a) CAD design of mould for enhanced waveguide platforms. (b) 3D preview of machined part produced by CAM software.

The mould was fabricated from brass using a CNC micromiller (CAT3D, Datron, U.K.) and then polished to produce surfaces having a high quality optical finish. This step is essential for the production of low loss waveguide platforms as it determines the surface roughness of the moulded waveguides. The polishing protocol involves manually abrading the relevant surfaces of the brass mould

with progressively finer grades of diamond paste (Hyprez, U.K.) until the desired surface finish was achieved. The polished brass mould is depicted in Fig. 7.3.

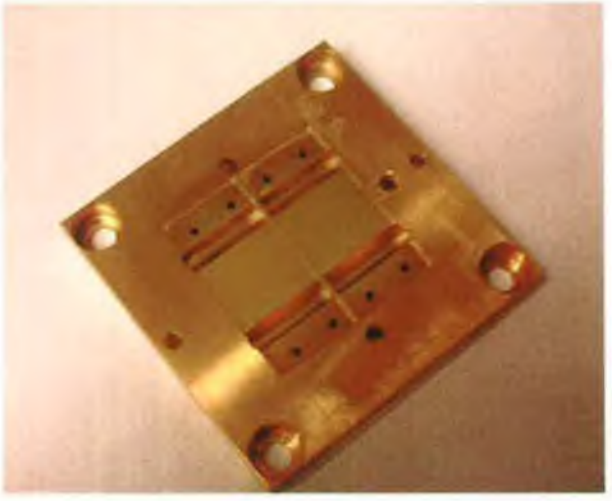

Figure 7.3: Image of polished brass waveguide mould.

The polymer platforms were fabricated using a Babyplast micro-injection moulder (JET Industrial Services, U.K.). Molten polymer — in this case, polystyrene (PS) — was injected into the polished mould where it was allowed to cool and solidify before being ejected in the form of plastic waveguide chips. Injection moulding is a high throughput technique and it was possible to produce 100 chips in approximately 5 minutes. A typical set of moulding parameters is shown in Table 7.1. It should be noted that these parameters are highly dependent on the polymer being injection moulded and that those shown here are representative of a moulding cycle using PS.

As shown in Fig. 7.3, the brass mould used was manufactured to contain two identical cavities that corresponded to two PS waveguide platforms, which were ejected from the mould at the end of each cycle. The waveguides were then separated for incorporation into the sensor head and did not require any further surface treatment prior to the deposition of the ammonia-sensitive layer, the preparation of which is described in the following section.

Moulding parameter	Value
Plastification chamber temp. (°C)	225
Injection chamber temp. (°C)	215
Nozzle temp. (°C)	205
Injection pressure (bar)	100
Injection time (s)	1
Load material (mm)	23
Cooling time (s)	2
Ejection time (s)	0.2
Number of strokes	2

Table 7.1: Parameters for a typical injection moulding cycle for the production of PS waveguide platforms.

7.2 Development of an optical sensor for gaseous NH_3

It was decided to apply the polymer waveguide platforms to the development of an optical NH_3 sensor as this was the analyte chosen to demonstrate the proof of principle device based upon the enhanced single-reflection configuration presented in the previous chapter. Ammonia detection is also an area of much research due to the toxic, corrosive nature of the gas and its presence in both industrial and agricultural environments. The maximum permissible exposure limit (P.E.L.) for NH_3 is 25ppm per 8 hour day per 40 hour working week and the levels present in wastewater can range from 1-20 ppm. It was hoped to demonstrate the effectiveness of the enhanced polymer platforms presented here in forming the basis of a potentially disposable sensor chip for the detection of NH_3 in the ranges mentioned above, as the applications of such a device are wide-ranging.

The following section describes the preparation of the sol-gel layer that was intended to act as the NH_3-sensitive colorimetric thin film in this application.

7.2.1 Preparation of sensing layer

The NH_3 sensitive layer consisted of a sol-gel-derived thin film doped with bromocresol purple, the pH indicator dye used previously for the development of the single-

reflection-based NH_3 sensor. A typical sol was prepared by dissolving the required amount of BCP in ethanol and then adding pH 1 HCl and a 50:50 molar ratio of tetraethoxysilane (TEOS) and methyltriethoxysilane (MTEOS) whilst stirring. The inclusion of MTEOS, a hydrophobic ORganically MOdified SILicate (ORMOSIL), was necessary to improve adhesion of the sensing layer to the hydrophobic surface of the polymer waveguide chip as 100% TEOS-derived films tended to de-adhere from the PS platforms. The resultant sol was allowed to stir for 1 hour and then aged at room temperature for 24 hours before deposition. Sensing layers were deposited on the chips by dip-coating after which the platforms were dried at 70°C. All samples were stored under ambient conditions for three weeks before use.

Fig. 7.4 shows the absorption spectrum of the BCP-doped sol-gel layer in its deprotonated state along with the emission spectrum of the amber LED (Marl Optosource, Cumbria) employed in the sensor head. The absorption band of the layer displays maximum absorbance at λ_{abs} = 593nm which overlaps well with the LED emission spectrum (λ_{max} = 601nm). The large overlap between the two spectra demonstrates the suitability of the LED as a light source for this application.

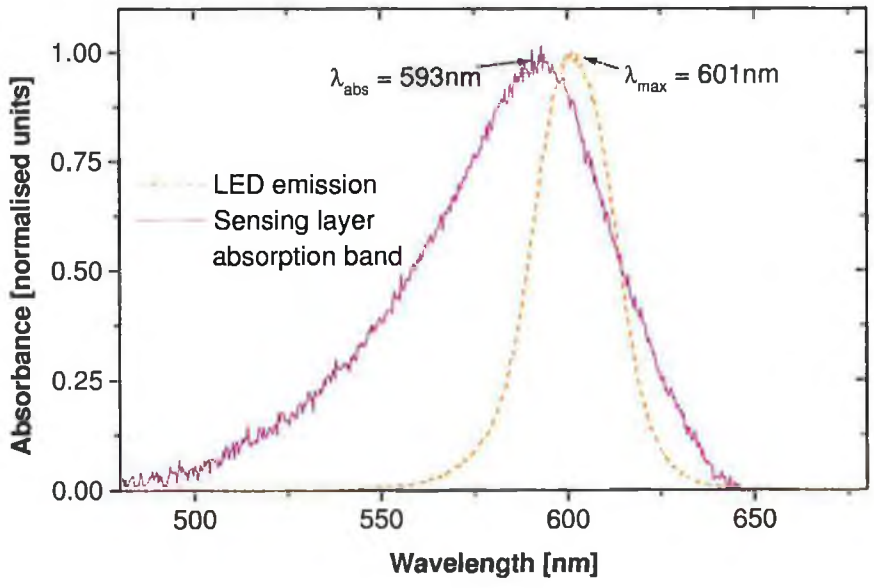

Figure 7.4: Absorption spectrum of sensing layer and LED emission spectrum.

7.2.2 Experimental setup

The coated platforms were placed in a custom-made metal head which facilitated the coupling of the light from the LED source into the waveguide at the desired angle of incidence. A diagram of the sensor head is shown in Fig. 7.5.

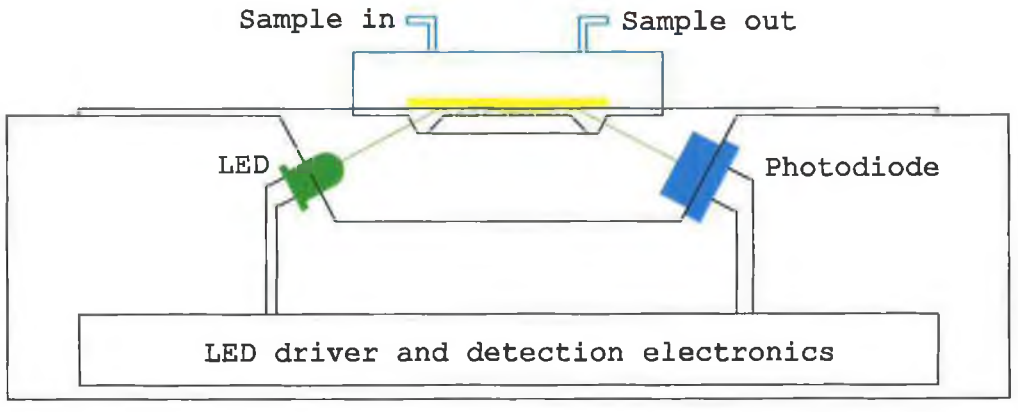

Figure 7.5: Sensor head design.

The light was outcoupled via the second refractive element to a silicon photodiode detector (S1223, Hamamatsu Photonics UK Ltd.). It is important to note that both the LED and photodiode were held in fixed positions relative to the polymer platform and this position was dictated by the theoretical model. Due to the fact that the model defines a specific relationship between the angle of interrogation and the sensitivity of the platform, the angular divergence of the LED was limited to approximately 6° through the use of an aperture. This ensured that the interrogating light was incident on the sensing layer at a narrow range of angles lying within the region of optimum sensitivity defined by the model. The sensor head also included a detachable flowcell, with which it was possible to flow mixtures of nitrogen and NH_3 over the sensing layer. Gas delivery was achieved using mass flow controllers (MFC's – UFC-1100 series, Celerity Ltd., Dublin), which facilitated precise regulation of analyte and carrier gas concentrations. In this case, the carrier gas was pure N_2, delivered via a MFC with a maximum flow rate of 500 ml per minute and the analyte gas was a mixture of 1% NH_3 in N_2 delivered using an MFC with a maximum flowrate of 5 ml per minute.

7.2.3 Results

Effect of modifying gas delivery setup.

The gas delivery setup was modified from that described in Chapter 6 for the initial NH_3 sensor employing the single reflection configuration. In that case, both gas flows were dry when delivered to the flowcell and the resultant response was extremely protracted. Due to the importance of water in the NH_3 sensing mechanism (see Chapter 6, Sec. 6.3.2), it was decided to humidify the gas flows in an attempt to improve sensor response time by ensuring an adequate supply of moisture for the sensing mechanism to occur. To this end, two gas washbottles containing de-ionised water were included in the nitrogen line. Initially, the NH_3 flow was also humidified but this resulted in long response and recovery times thought to be due to the solvation of NH_3 in the washbottle to form ammonium hydroxide ($NH_4^+OH^-$). A fraction of the $NH_4^+OH^-$ would then dissociate into the gas phase to be delivered to the flowcell. This dissociation resulted in a lengthy response time and also affected the recovery time due to the fact that NH_3 would still be filling the gas line even when the MFC channel was closed. It was, therefore, decided to humidify the nitrogen line only and to mix this flow with a dry flow of $1\%NH_3$ in N_2. The improvement in sensor response time for this setup is evident when the response curves in the following section are compared with those presented in Chapter 6, Sec. 6.3.2. What follows is an examination of the sensor response to gaseous NH_3 and its dependence on conditioning.

Effect of conditioning on sensor repsonse.

A sensor response curve is shown in Fig. 7.6. The film was exposed to 100ppm NH_3 and its response is clearly two-phase in nature, with an initial rapid drop in signal followed by a slow transition phase illustrated by a "shoulder" in the response curve.

The initial response is clearly more rapid in nature than that obtained using dry gas flows presented in Chapter 6, which indicates the success of humidifying the carrier gas flow in facilitating the NH_3 sensing mechanism. However, the presence of the shoulder in the response curve suggests a two-stage nature in the sensing process.

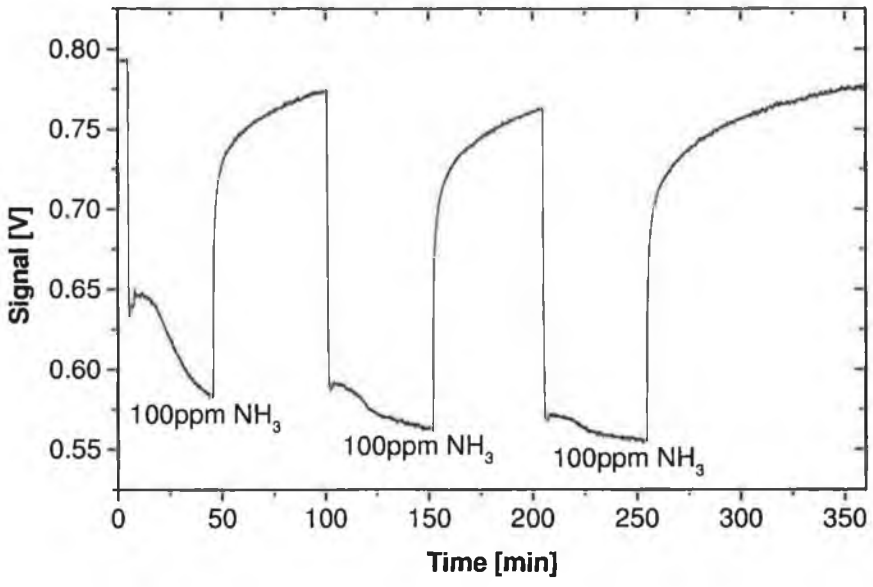

Figure 7.6: Conditioning of sensing layer at 100ppm NH_3.

This effect has been reported elsewhere where it was attributed to the influence of the surface polarity of the film and the stability of the indicator dye used [1]. It was stated that BCP, a sulfonephthalein pH indicator dye, can exist in two forms, a closed form and a zwitterion form and it is only the in the latter form that it is free to react with basic species. Furthermore, the stability of the zwitterion is believed to be improved through deprotonation of the dye. It is clear from Fig. 7.6 that the "shoulder" effect lessens on subsequent exposures to the same concentrations of NH_3 which points to an increase in the proportion of the zwitterion dye form relative to the closed form. This would appear to corroborate the belief that zwitterion stability is positively influenced by dye deprotonation.

In a related work by Ismail *et al.* [2], it was reported that a post-fabrication treatment of sol-gel-derived sensing layers (doped with bromomcresol green) using a mildly alkaline solution resulted in a rapid pH response due to the reduction of silanol groups that react with the polar dye within the pores of the layer, allowing the dye to react more rapidly with protons in the analyte solution. This would suggest that the slow response times noticed previously were due to the "active" nature of the sol-gel matrix itself.

However, in collaboration with members of the School of Chemical Sciences at Dublin City University, an alternative sensing matrix based on cellulose ac-

etate doped with BCP was examined. It was believed that this matrix would yield faster response times due to the absence of silanol groups in the pores of the sensing layer. Sensing layers were deposited on glass and examined in the enhanced single-reflection configuration. It was not possible to deposit the cellulose acetate-based layers onto the PS waveguides due to the presence of acetone and cyclohexanone (necessary to dissolve cellulose acetate) in the liquid sensor cocktail. These solvents also dissolve PS, making this sensing layer incompatible with the current waveguide platforms. Fig. 7.7 illustrates the response of a BCP-doped cellulose acetate sensing layer to 100 ppm NH_3 and the presence of the characteristic shoulder in the response profile is clear. Successive exposures to the same concentration of NH_3 result in a reduction of this feature, as with the response of the sol-gel-based layer shown in Fig. 7.6. This would appear to suggest that the protracted response is not related solely to the sensing matrix but that it is to a large extent dependent on the state of the indicator dye itself.

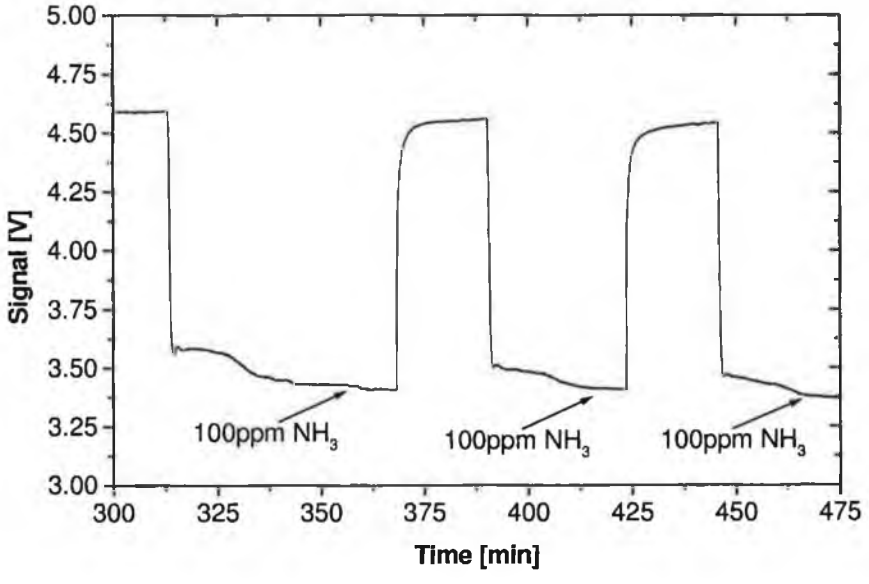

Figure 7.7: Response of cellulose acetate-based sensing layer to 100ppm NH_3.

Fig. 7.8 shows the response of the sol-gel-based sensing layer (deposited on a PS waveguide) to 10ppm NH_3 before and after exposure to 100ppm NH_3. There is clearly an improvement in response after exposure to the higher concentration (which caused increased dye deprotonation). Indeed, the sensitivity at 10ppm increased by over 50% while the response time was virtually unchanged as shown in Table 7.2.

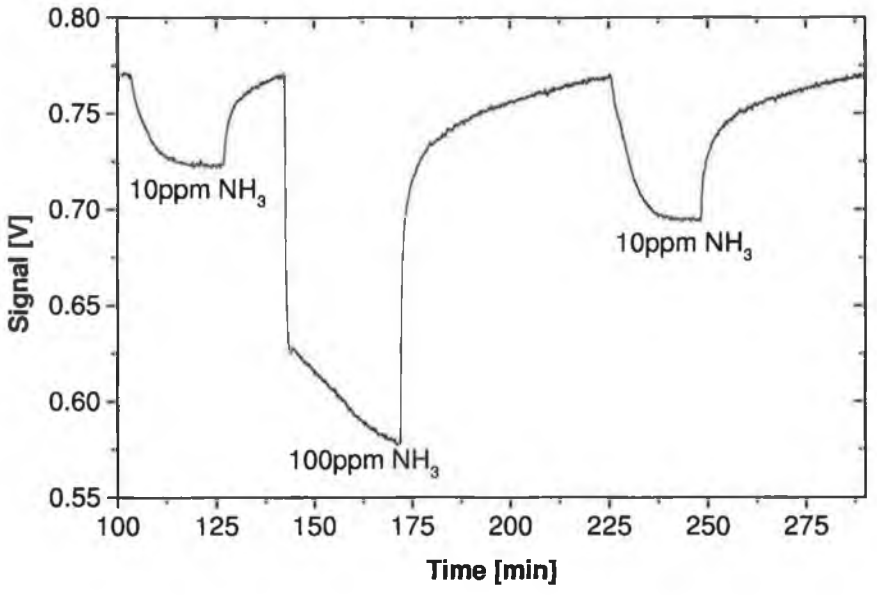

Figure 7.8: Conditioning of sensor response to 10ppm NH_3.

	t_{90}[min]	ΔV[mV]
Before exposure	9	48
After exposure	9.5	75

Table 7.2: Sensitivity and response times before and after exposure to 100ppm NH_3

These results clearly illustrate the need to condition the BCP-doped sensing layers in order to achieve optimum sensitivity. Therefore, all samples were exposed to 100ppm NH_3 until the shoulder was no longer evident in the signal profile before any attempt was made to record a response curve. Fig. 7.9 shows the response of the sensing platform to NH_3 concentrations varying between 0ppm and 20ppm. The sample has clearly undergone adequate conditioning as evidenced by the classical nature of the response curves. Sensitivity is greatest at lower concentrations, which is characteristic of the pH indicator dye used but the platform is clearly sensitive to changes in NH_3 concentration over the entire range.

The resultant calibration curve is shown in Fig. 7.10 which demonstrates the sensitivity of the sensor system, yielding a limit of detection (L.O.D.) of 400ppb. This is an improvement on previous work that employed evanescent-wave interrogation of a sensing layer coated onto a planar waveguide [5]. In that work,

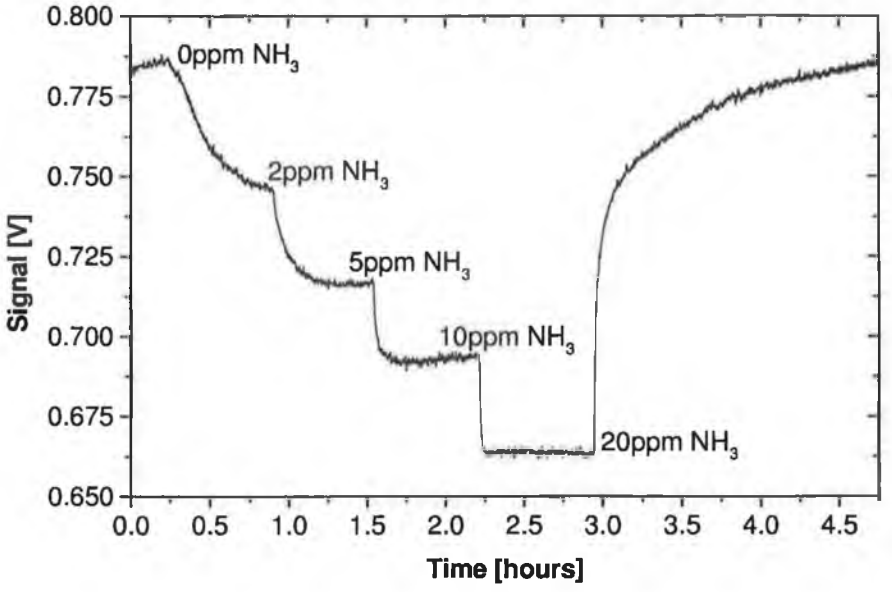

Figure 7.9: Sensor response to varying NH_3 concentrations.

light was coupled to the waveguide via integrated sol-gel grating couplers and the sensor achieved a L.O.D. of 5ppm NH_3.

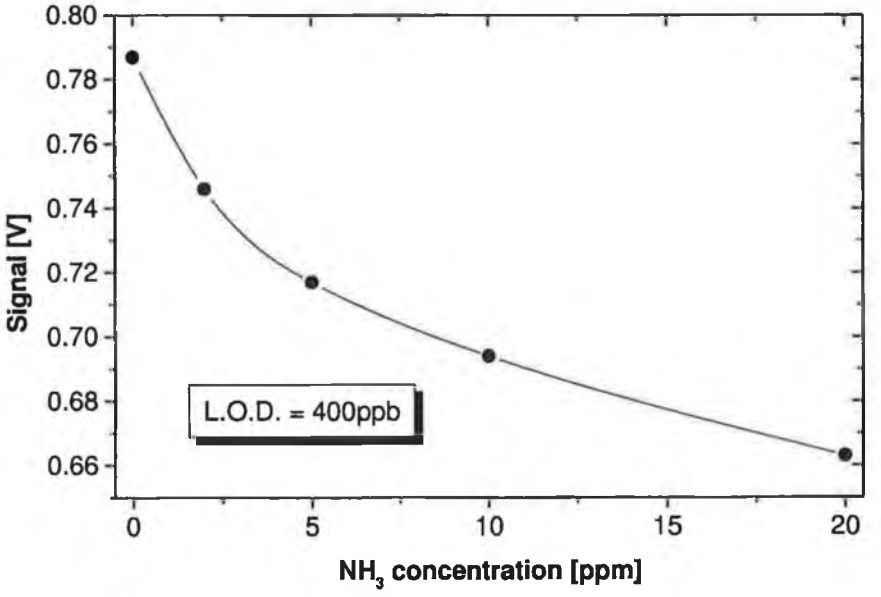

Figure 7.10: Sensor calibration curve.

Sensor response and recovery times are also an issue. Table 7.3 summarises the response times of the sensor for varying changes in NH_3 concentration.

Similar times have been reported elsewhere employing a silicone matrix doped

Change in NH_3 concentration	Response times	
	t_{90}[min]	t_{100}[min]
0ppm → 2ppm	26.8	38.5
2ppm → 5ppm	12.1	21.4
5ppm → 10ppm	2.3	10.9
10ppm → 20ppm	1.9	4.3

Table 7.3: Sensor response times for varying changes in ammonia concentration

with bromophenol blue by an ion-pairing approach [3, 4]. However, the NH_3 concentrations were much lower than those examined here and it is likely that response times would be shorter at higher concentrations. The problem does not appear to be related solely to diffusion of the analyte into the sensing layer as the response times obtained for the cellulose acetate-based sensor were also quite protracted.

However, the current results still compare favourably with others published previously where more complex sensor configurations were employed [5, 6] and serve to illustrate the viability of the design and fabrication protocol used to produce the polymer waveguide platforms.

The next stage in this work was to investigate the validity of the theoretical predictions outlined in Chapter 5, Sec. 5.3.2 relating to the dependence of platform sensitivity on interaction length.

7.3 Investigation of sensitivity profile of enhanced polymer waveguide platforms

At this point, it is instructive to summarise the theoretical findings outlined in Sec. 5.3.2 relating to the sensitivity dependence of platforms employing an enhanced mode, multiple-reflection configuration. The findings were illustrated in Fig. 5.7, which is a plot of the relationship between sensitivity and interaction length for various absorption coefficients, α_s, of the sensing layer when the interrogating light is incident on the sensing layer at the optimum angle of incidence, θ_{opt}, corresponding to the enhanced mode of interrogation predicted by the model

and verified in the single reflection configuration (see Chapter 6, Sec. 6.2).

The graph shows sensitivity increasing with interaction length up to a critical interaction length, L_c, after which it decreases exponentially. The obvious implication of this model is that a longer interaction length, or a higher number of reflections, does not guarantee improved sensor performance when employing this optimised mode of interrogation.

The goal of the work reported here was to verify the existence of a critical interaction length, L_c, for which sensor performance was optimum and to determine if the sensitivity profile of the enhanced polymer platforms was similar to that predicted by the theoretical model. To this end, it was decided to investigate the performance of an optical pH sensor consisting of a BCP-doped sol-gel layer deposited on the polymer waveguides. The choice of analyte was changed from NH_3 due to the unstable response associated with these sensors that was highlighted in the previous section. It was believed that, by switching to pH sensing, the instabilities associated with the NH_3 sensing mechanism could be eliminated through use of the post-fabrication sample treatment described in [2]. This could then facilitate an investigation of the sensitivity profile of the platforms that was free from the influence of an unstable sensing chemistry.

7.3.1 Sample preparation

The sol-gel formulation employed was similar to that described for the development of the NH_3 sensor. The only difference was an increase in the amount of TEOS used. The ratio of TEOS:MTEOS was increased from 50:50 to 90:10 for the development of the pH sensor. A reduction in the MTEOS content was desirable due to the poor proton-permeability associated with such hydrophobic matrices, resulting in lengthy sensor response times. The inclusion of MTEOS was, however, necessary to prevent leaching of the indicator dye from the sol-gel matrix upon exposure to the pH buffer solutions.

PS waveguide platforms were fabricated as described in Sec. 7.1. An additional step, in the form of plasma cleaning, was then introduced in order to improve the adhesion of the sol-gel-based sensing layer to the polymer surface. Platforms were placed in a benchtop plasma cleaner (Harrick Scientific, U.S.A.) and exposed to a RF air plasma for 1 minute after which they were removed, masked and the

sensing layers deposited by spin-coating. The plasma treatment was necessary in this case due to the increased TEOS content of the sol-gel sensing layers. It was, therefore, necessary to increase the wettability of the PS waveguides in order to facilitate the adhesion of the predominantly hydrophilic sol-gel layers to the waveguide surface. The use of RF plasma cleaning to increase the wettability of PS substrates has been reported previously [7]. The masking step involved covering the upper surface of the platforms with tape to define specific lengths that were to be coated with the sensing layer, a step that was central to the investigation of the sensitivity dependence on interaction length. Samples were subsequently dried at 70°C for 2 hours and then immersed in a 2×10^{-5}M solution of NaOH prior to use, this being the post-fabrication treatment mentioned earlier [2]. A description of the effect of this sample conditioning step on sensor response is given in Sec. 7.3.3.

All sensing layers were examined by profilometry to ensure that their thicknesses were approximately 800 nm ($\pm$ 50 nm). This is an important aspect of sensor design due to the fact that the angle of optimum interrogation is dependent not only on the relevant refractive indices but also on the thickness of the sensing layer. In this case, the optimum angle of incidence was calculated for a layer thickness of 800 nm. A variation in thickness of 100 nm results in a difference of less than 1° in θ_{max}. Taking into account the limited angular divergence of the LED (as described in Sec. 7.2.2) a variation of 1° in optimum angle would not unduly affect sensor performance.

7.3.2 Experimental setup

The experimental setup was similar to that described for the NH_3 detection system in Sec. 7.2.2. However, the gas delivery setup was replaced by a peristaltic pump which facilitated delivery of pH buffer solutions to a PDMS flowcell that formed a seal with the upper surface of the polymer waveguide. This flowcell was fabricated by moulding against a photolithographically defined rectangular SU-8 template (see Chapter 4, Sec. 4.1.1 for a description of the PDMS moulding procedure). The template was produced using an acetate photomask as described in Chapter 4, Sec. 4.3.3, the design of which can be found in appendix B. The inlet and outlet of the flowcell were defined by puncturing the PDMS with syringe

needles and connecting these to the peristaltic pump tubing.

7.3.3 Results and discussion

Effect of sample conditioning on sensor response

In the work presented here, samples were immersed in a 2 x 10^{-5}M solution of NaOH for 2 days prior to use. In the work done by Ismail *et al.*, it was stated that a 24 hour immersion in a 0.2 x 10^{-7}M solution was sufficient to condition the layer but this did not appear to be the case for the films used here. It is possible that the increased alkalinity was required due to the fact that BCP has a higher pK_a in sol-gel than Bromocresol Green (the dye used by Ismail *et al.*) and would not, therefore, become deprotonated at such a relatively low pH. This would suggest, however, that the sample treatment serves to condition the dye (by improving zwitterion stability) and not the layer itself.

The treatment had a pronounced effect on sensor response which is illustrated in Fig. 7.11. In the first case, the response is clearly two phase with an initial fast

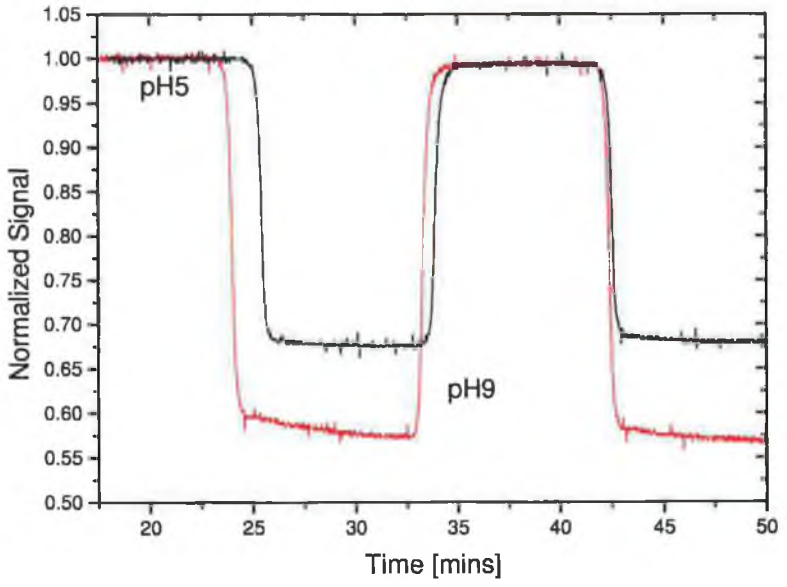

Figure 7.11: pH response of sensor platform before and after conditioning.

drop in signal followed by a slow reduction without reaching a stable signal level. The response of the fully conditioned sample is, on the other hand, extremely fast, stabilizing in less than 1 minute. It is worth noting that the sensitivity

of the conditioned sample is less than that of the partially conditioned one and this same effect was reported by Ismail *et al.*, who noted a reduction in the pH range of the sensors studied. For the purposes of comparing samples of different interaction length, it was ensured that all layers were fully conditioned in order to accurately measure their relative sensitivities.

Dependence of sensitivity on interaction length

Fig. 7.12 illustrates the response of sensing platforms with a range of coating lengths to buffer solutions of pH5 and pH9, respectively. The higher voltage is the value obtained at pH 5. The maximum voltage was offset to 1 V when plotting the data to aid in the comparison of signal change for each sample. The coating lengths for these platforms varied over the range 2mm to 12mm. It should be noted that the response profiles have been offset with respect to one another on the X-axis in order to aid in their visualisation and that the sample injection and response times did not vary significantly from sample to sample. Table 7.4 shows the signal change in volts for each of the coating lengths

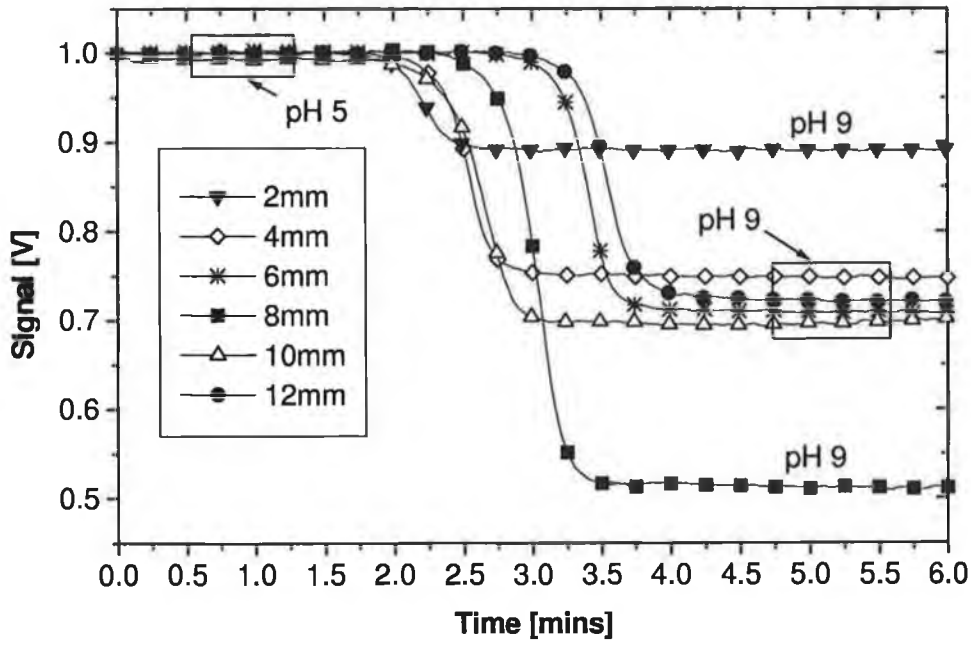

Figure 7.12: Sensor response for various coating lengths.

studied. The maximum signal change — and hence maximum sensitivity — was observed for a coating length of 8mm with greater lengths resulting in a reduction

in signal change. These findings are in qualitative agreement with theoretical predictions and clearly demonstrate the existence of an optimum length, L_c, for which sensitivity is maximum and, furthermore, indicate that this length *does not* correspond to the maximum coating length studied.

Coating length [mm]	Signal change [V]
2	0.109
4	0.252
6	0.291
*8	0.487
10	0.298
12	0.277

Table 7.4: Recorded signal change for each coating length.

It is important here to distinguish between coating length and optical interaction length. The theoretical predictions are based on the assumption that the incident light interrogates the entire length of the sensing layer for each interaction length investigated. However, the multimode nature of the waveguide platforms employed in this work results in the light interrogating the sensing layer in the form of discrete reflections as it propagates along the waveguide. The actual optical interaction length is directly proportional to the number of reflections from the sensing layer. With this in mind, the number of such discrete reflections was calculated for each coating length used. The results of this analysis are shown in Fig. 7.13 where the existence of a clear peak in sensitivity is evident. This is entirely in keeping with the predictions of the theoretical model as described in Chapter 5, Sec. 5.3.2. It must be noted that this approach is empirical in nature as it is not possible to ascertain the actual interaction length of each sample due to difficulties in determining the extent of each reflection in the sensing layer. For this reason, although the results cannot be compared directly to theoretical predictions, they do serve to highlight the existence of the peak in sensitivity that is predicted by the model.

This peak in sensitivity has major implications for sensor design as it enables selection of the optimum platform dimensions. The platform can therefore be tailored to specific applications as the concentration ranges of interest, together

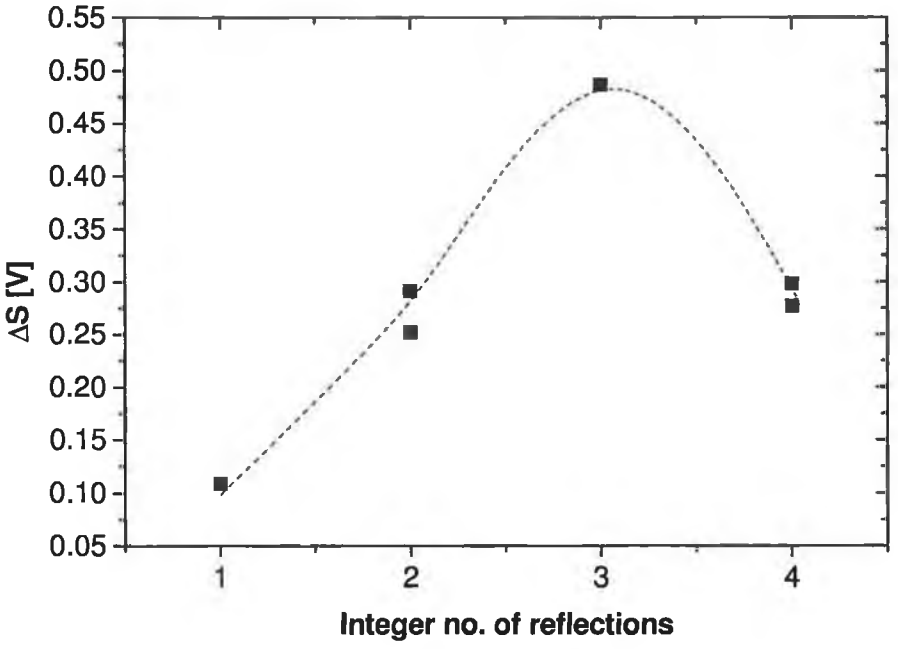

Figure 7.13: Dependence of signal change (related to sensor sensitivity) on integer number of reflections.

with the specific dye used, determine the values of α_s and hence the optimum interaction length required. The semi-empirical optimisation strategy therefore consists initially of identification of the optimum number of reflections on a platform designed to operate at θ_{opt}. For example, in the data presented in Fig. 7.13, the optimum number of reflections is 3 and the platform dimensions and coating length can then be adjusted accordingly.

Comparison of platform performance with other optical configurations

Fig. 7.14 illustrates the response of reflectance-based, transmittance-based and optimised configurations, all of which employed the same light source and detection electronics as well as a sensing element consisting of a BCP-doped sol-gel layer coated onto a PS waveguide platform.

Table 7.5 displays the pH resolution obtained using the configurations mentioned above along with that of a fibre-based system developed previously which employed evanescent wave interrogation of the sensing layer [8].

The difference in pH resolution for the three samples is clear, with the optimised configuration outperforming the transmittance-based by a factor of 3.25

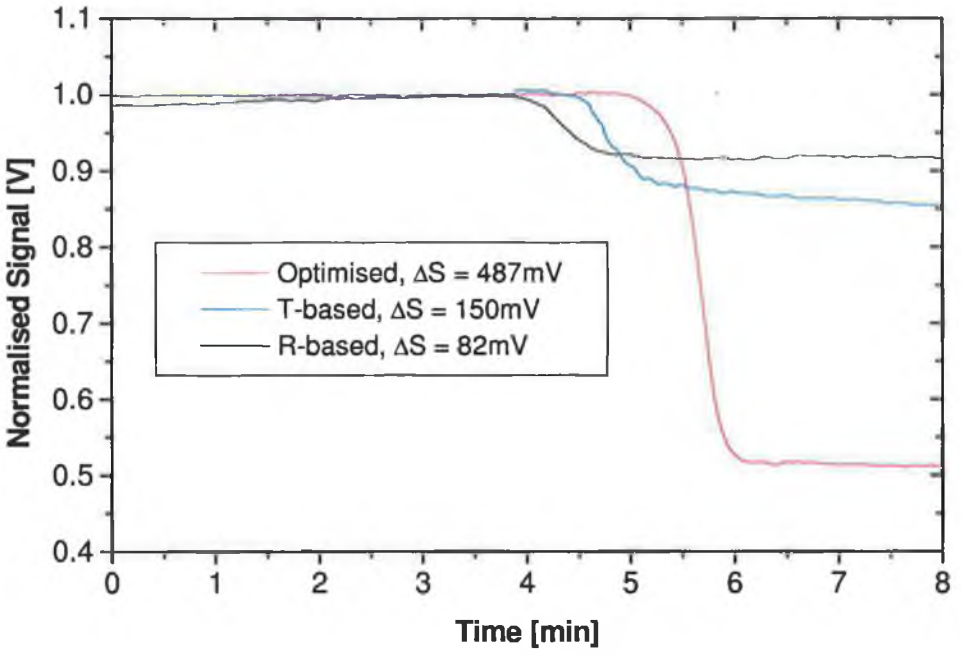

Figure 7.14: Comparison of sensor response for transmittance-based, reflectance-based and optimised configurations.

and the reflectance-based by a factor of almost 6. The enhanced platforms discussed here offer a clear improvement in sensitivity over these other commonly employed configurations and, furthermore, do so with an interaction length of only 8mm as opposed to the much greater lengths required in order to achieve this performance employing evanescent wave interrogation. Indeed, the platforms studied here achieve comparable sensitivity to the fibre-based system, which employed an interaction length 7.5 times that of the platforms.

Configuration	Resolution[pH units]
Transmittance	0.12
Reflectance	0.22
Evanescent-wave	0.025
Optimised (waveguide)	0.036

Table 7.5: Comparison of sensor resolution for various configurations.

It is interesting to note that the optimised system presented here does not compare favourably to the single-reflection-based system reported in Chapter 6 where a pH resolution of 0.007 pH units was achieved. It is worth noting however,

that the optical quality of the sensor platform influences performance parameters such as resolution as does the coupling efficiency of the setup. These characteristics are highly dependent on the quality of the polished mould and the success of the injection moulding process. Work is currently under way to optimise these steps in the fabrication of the sensor platform.

7.4 Conclusions

This work has described the development of mass-producible, enhanced polymer waveguide platforms. These platforms were fabricated by micro-injection moulding and coated with sol-gel-derived sensing layers by both dip-coating and spin-coating. They were first applied to the detection of gaseous NH_3 and the unstable nature of the sensing mechanism was highlighted along with the conditioning process required to yield a stable sensor response. The results obtained using a cellulose acetate-based sensing layer appear to indicate that the non-classical sensor response profile is a feature of the dye used and is not due solely to the sensing matrix itself.

The sensor platforms displayed a L.O.D. of less than 400 ppb for gaseous NH_3, which is a ten-fold improvement on previously published work employing a planar waveguide platform with integrated grating couplers [5].

The following stage in this work was the experimental investigation of the theoretical model's predictions pertaining to an enhanced multiple reflection configuration. The model predicted that, for a given absorption coefficient of the sensing layer, there existed a peak in sensitivity that was achieved for a certain critical interaction length. In order to verify this, waveguide platforms were coated with pH-sensitive sol-gel layers of different lengths and their response was investigated experimentally. Signal change was plotted as a function of number of reflections interacting with each sensor platform and a peak in sensitivity for a critical number of reflections was evident. While this analysis was empirical in nature it confirmed the existence of optimum sensing conditions in a multiple reflection configuration as predicted by the model.

These results have significant implications for the design of miniaturised, yet highly sensitive polymer sensor platforms. As a figure of merit, the pH resolution yielded by these chips (0.036 pH units) was comparable to that of a previously

developed fibre-based system with an interaction length of over 7 times that of the coating length of the waveguides presented here [8]. The dependence of sensitivity on interaction length can also be exploited to tune the sensitivity of the platform to certain concentration ranges (i.e. certain absorption coefficients) in particular applications.

This strategy shows great potential for the fabrication of low-cost, disposable optical absorption-based sensor platforms that exhibit enhanced sensitivity compared to current commonly employed configurations.

Bibliography

[1] C. Malins, T. M. Butler, and B. D. MacCraith, "Influence of the surface polarity of dye-doped sol-gel glass films on optical ammonia sensor response," *Thin Solid Films*, vol. 368, no. 1, pp. 105–110, 2000.

[2] F. Ismail, C. Malins, and N. J. Goddard, "Alkali treatment of dye-doped sol-gel glass films for rapid optical ph sensing," *Analyst*, vol. 127, no. 2, pp. 253–257, 2002.

[3] T. Werner, I. Klimant, and O. Wolfbeis, "Ammonia-sensitive polymer matrix employing immobilized indicator ion pairs," *Analyst*, vol. 120, pp. 1627–1631, 1995.

[4] M. Trinkel, W. Trettnak, F. Reininger, R. Benes, P. Oleary, and O. S. Wolfbeis, "Study of the performance of an optochemical sensor for ammonia," *Analytica Chimica Acta*, vol. 320, no. 2-3, pp. 235–243, 1996.

[5] A. Doyle, C. Malins, B. MacCraith, F. Kvasnik, M. Landl, P. Simon, L. Kalvoda, R. Lukas, K. Pufler, and I. Babusik, "Personal ammonia sensor for industrial environments," *Journal of Environmental Monitoring*, vol. 1, pp. 417–422, 1999.

[6] A. Lobnik and O. S. Wolfbeis, "Sol-gel based optical sensor for dissolved ammonia," *Sensors and Actuators B-Chemical*, vol. 51, no. 1-3, pp. 203–207, 1998.

[7] T. G. van Kooten, H. T. Spijker, and H. J. Busscher, "Plasma-treated polystyrene surfaces: model surfaces for studying cell-biomaterial interactions," *Biomaterials*, vol. 25, no. 10, pp. 1735–1747, 2004.

[8] T. Butler, B. MacCraith, and C. McDonagh, "Development of an extended range fiber optic pH sensor using evanescent wave absorption of sol-gel entrapped pH indicators," in *Chemical, Biochemical, and Environmental Fiber Sensors VII* (A. V. Scheggi, ed.), vol. 2508, pp. 168–178, Proc. of SPIE, 1995.

[9] L. Polerecky, C. S. Burke, and B. D. MacCraith, "Optimization of absorption-based optical chemical sensors that employ a single-reflection configuration," *Applied Optics*, vol. 41, no. 15, pp. 2879–2887, 2002.

Chapter 8

Applications of soft lithography in optical sensing

The previous chapter has shown how polymer processing technology can be effectively combined with a dedicated sensor optimisation strategy to produce sensor platforms that either outperform or match the performance of more complex sensor configurations. Furthermore, this can be achieved by employing a more flexible and efficient fabrication protocol.

This chapter describes the use of soft lithographic techniques to achieve similar goals. The applications presented are intended to highlight the effectiveness of these techniques both in demonstrating proof of principle systems and in producing improved sensors more efficiently (as described in Sec. 8.5).

8.1 Fabrication of sol-gel grating couplers using SAMIM

Surface corrugation gratings provide a means of coupling incident radiation into the waveguides on which they are patterned. A detailed theoretical analysis of coupling using such gratings is beyond the scope of this thesis but readers should refer to [1, 2, 3] for a description of this process. In short, coupling is achieved due to phase matching between diffracted orders and waveguide modes. The use of grating couplers is attractive from the point of view of sensor geometry as these couplers do not detract from the planarity of such waveguide-based sensors, as is

the case with prism couplers. Previous work at the Optical Sensors Laboratory involved the fabrication of sol-gel grating couplers on planar waveguides and such platforms were applied to the detection of gaseous ammonia [4]. The method by which the gratings were fabricated was embossing of a thin sol-gel layer (see next section) but there were some disadvantages associated with this technique. For this reason SAMIM (described in Chapter 4, Sec. 4.1.6) was examined as an alternative fabrication technique.

8.1.1 Experimental

The existing technique for embossing [5] involved the use of a custom-made embossing rig, shown in Fig. 8.1, to press a commercially available master grating into a thin sol-gel layer in order to transfer the grating profile into the layer. The sol-gel formulation was prepared by adding 4g of MTEOS to 4g of ethanol whilst stirring. 2g of titanium tetra-butoxide, a refractive index modifier was then added to this mixture followed by the immeditate addition of 0.4ml of silicon tetrachloride ($SiCl_4$), which acted as the catalyst. The sol was stirred for 1 hour then aged at room temperature for 24 hours prior to use. Thin films were deposited by dip-coating, directly after which the embossing step was carried out. This technique, while effective, required the application of a high force for the production of viable gratings. The relatively large force involved, coupled with the subsequent organic solvent cleaning procedure, resulted in the degradation of the aluminium-coated master gratings, rendering them unusable after approximately 50 procedures. This method also suffered from a lack of reproducibility due to the absence of any automation in the embossing process.

SAMIM does not require a high force for effective pattern transfer. In brief, the technique involves "inking" a PDMS grating (fabricated by casting against the commercially available master grating) with an appropriate solvent and pressing into a layer of the material to be patterned. The presence of the solvent causes the material to conform to the shape of the features carried on the PDMS grating. In the work reported here, the technique was modified slightly and the material to be patterned (in this case sol-gel) was itself diluted with methanol prior to its deposition on the substrate. The sol-gel formulation employed was identical to that used for the embossing procedure. The sol was diluted with methanol in

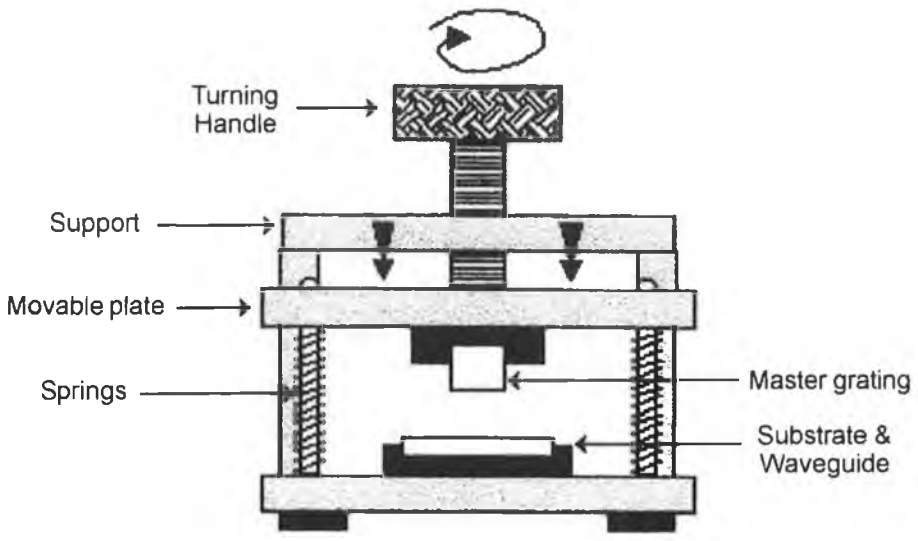

Figure 8.1: Embossing apparatus used for the fabrication of sol-gel grating couplers.

a 1:1 ratio by volume prior to deposition. This was achieved by pipetting a drop onto the glass microscope slide used as the substrate. An uncoated PDMS grating was then pressed into the drop and held there overnight using a bulldog clip. This technique was quite uncomplicated, yet lent a much higher degree of reproducibility to the fabrication process compared with embossing. Furthermore, the use of a PDMS grating substantially reduced wear and tear on the master as this was required for just one moulding procedure after which the PDMS grating could be used as a sub-master for the fabrication of further stamps. Another advantage was that methanol could be used to clean the stamp without damaging the surface profile, PDMS being resistant to polar solvents.

8.1.2 Results

Having established the possible advantages of SAMIM over embossing, it was necessary to experimentally verify this technique for the production of grating couplers. To this end several gratings were fabricated on glass slides using both procedures, as described in the previous section. These gratings were then examined by Atomic Force Microscopy (AFM). As shown in Figs. 8.2(a) and (b), both gratings display a similar profile. However, the period of the embossed gratings

($\Lambda \approx 1.705\mu$m) was slightly larger than that of the gratings fabricated by SAMIM ($\Lambda \approx 1.66\mu$m). This can be attributed to a slight shrinkage of the PDMS stamp during the thermal curing process.

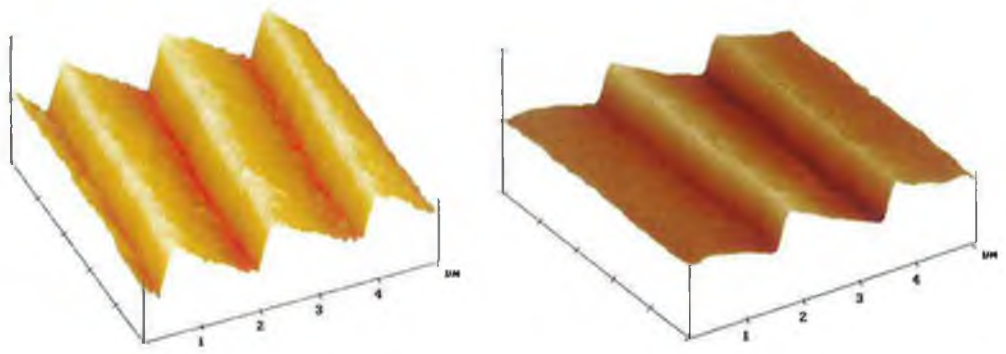

(a) (b)

Figure 8.2: AFM images of sol-gel grating couplers fabricated by (a) SAMIM and (b) embossing.

Of greater importance was the diffraction efficiency of the gratings themselves. Fig. 8.3 shows the experimental setup used to measure the diffraction efficiencies of gratings manufactured by both SAMIM and embossing.

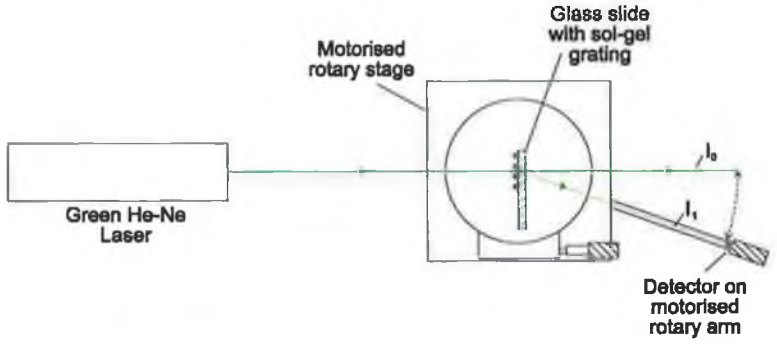

Figure 8.3: Experimental setup for the measurement of diffraction efficiency of sol-gel grating couplers.

Samples were mounted on a motorised rotary stage and light from a green HeNe laser (λ=543.5nm) was incident on the grating. The intensity of the zeroth and first orders was measured by a photodiode detector. This was mounted on a metal arm that was connected to a stepper motor. Both the rotary stage and stepper motor were controlled via PC using LabVIEW software. The diffraction

efficiency, η, was measured as the ratio of the intensities in first and zeroth orders. Figs. 8.4 (a) and (b) show the typical angular dependence of η for both embossed and micromoulded grating couplers, respectively. The efficiency peaks in the same region for both, but $\eta \approx 3.5\%$ for the micromoulded gratings compared with a value of approximately 2.75% for the embossed gratings demonstrating that, not only is the method of fabrication less costly and labour-intensive than embossing, it also produces gratings of a comparable if not greater diffraction efficiency.

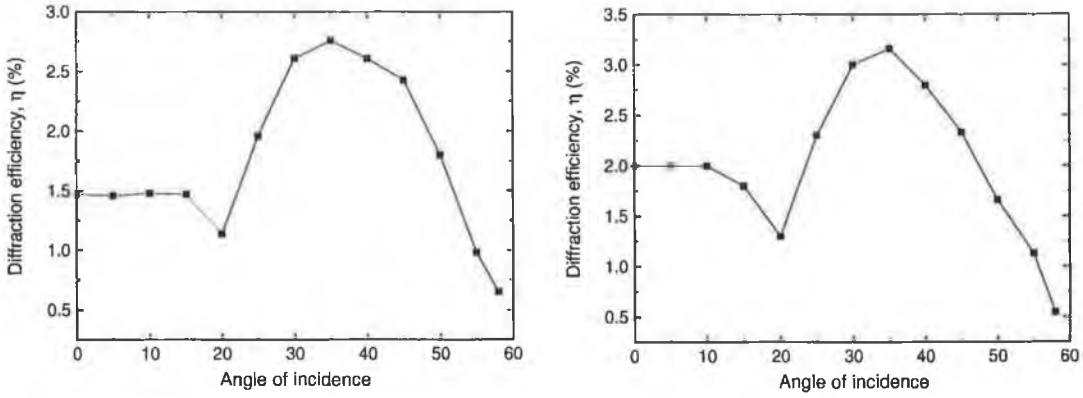

(a) (b)

Figure 8.4: Diffraction efficiencies of (a) embossed and (b) micromoulded sol-gel grating couplers

8.1.3 Summary

The technique of SAMIM was applied to the fabrication of sol-gel grating couplers. The resultant gratings displayed improved diffraction efficiencies compared with those fabricated by embossing. SAMIM was an improvement on this technique in terms of ease of implementation, reproducibility and resultant grating quality.

The following section describes the process of sensor spot deposition by μTM, also referred to as PDMS stamp printing.

8.2 Sensor spot deposition by μTM

The deposition of discrete sensor spots has obvious advantages from the point of view of multianalyte sensing as it enables the immobilisation of multiple sensing

chemistries on a single platform. In this section, the patterning of such spots using a PDMS stamp will be described. The technique employed was a modified version of μTM (see Chapter 4, Sec. 4.1.3), with the PDMS stamp being moulded from a cylindrical cavity approximately 3mm deep and 2mm wide. This initial prototype was then used to transfer sol-gel, doped with a fluorescent ruthenium complex, from a vial to the substrate being patterned. The procedure was tested by patterning a 2 x 2 array of spots on a glass slide and imaging the fluorescence using a CCD camera. The resulting image is shown in Fig. 8.5.

Figure 8.5: Array of sensor spots patterned with PDMS stamp

The spots in the right-hand column were exposed to a low concentration of gaseous oxygen and the reduction in relative intensities between these and the spots in the left-hand column is apparent. This was due to collisional quenching of the fluorescence by oxygen molecules. This experiment, while simple, demonstrated the ease with which such discrete sensor spots could be deposited using an essentially disposable patterning element.

PDMS stamp printing was also employed as an alternative to pin-printing during the development of an integrated optical oxygen sensor (see Sec. 8.5) and was employed for the deposition of sensing layers onto structures designed to enhance fluorescence capture (see next section).

Is is important to note that PDMS stamp printing, while quite versatile and simple to implement, is not a reproducible method of sensor spot deposition. It is more suited to proof of principle applications and serves the purpose of ascertaining the viability of a particular sensing configuration, after which the use

of more reproducible spot deposition techniques such as arraying or pin-printing is desirable (see Sec. 8.5).

8.3 PDMS stamp fabrication by replica moulding

Other work at the Optical Sensors Laboratory has concentrated on the development of enhanced fluorescence-based optical sensor platforms by optimising fluorescence capture. To this end, a previously reported theoretical analysis [6] was applied to the design of a polymer chip carrying an array of frustrated cones onto which fluorescent sensor films were to be deposited. In the absence of a suitable printing apparatus, it was decided to avail of PDMS stamp printing to deposit the sensing layer onto the top of the cone structures. In this case, a 1mm stamp was required as this corresponded to the diameter of the structures' surface. It was possible to employ replica moulding in the fabrication of this stamp.

PDMS was first cast against the structures themselves and the resulting mould was treated with a trichlorosilane to render its surface "non-stick" as described in Chapter 4, Sec. 4.1.4. This silanisation procedure made it possible to cast PDMS *against the mould*, thus obtaining a stamp of the required dimensions. The ability to cast PDMS against PDMS further enhances the versatility of soft lithography as it facilitates the fabrication of PDMS sub-masters, which can be used instead of the often more expensive masters themselves.

8.4 Patterning of an optical Y-splitter by MIMIC

8.4.1 Background

Micromoulding in capillaries (MIMIC), as described in Chapter 4, Sec. 4.1.2, has been applied to the fabrication of sol-gel ridge waveguides in a variety of configurations during the course of this work. These include single ridges, ridge waveguide arrays and optical power splitters, the fabrication of which is the focus of this section. The intended application of the optical Y-splitter fabricated here was to form the basis of a self-referencing optical pH sensor.

The desired configuration for the optical sensor is shown in Fig. 8.6. It consists of two multimode ridge waveguides in a Y-splitter configuration which facilitates the simultaneous interrogation of the two waveguides using a single light source.

Figure 8.6: Schematic of y-splitter.

The circular pad at the input of the splitter is included to act as a reservoir for the UV-curable sol-gel during the patterning process. Sol-gel spots are deposited onto the arms of the splitter by PDMS stamp printing, with one spot being doped with a pH sensitive, colorimetric indicator dye and the other consisting of undoped sol-gel. The arm carrying the undoped spot acts as a reference for the system. By carrying out a ratiometric analysis of the outputs from both arms of the splitter, it is possible to obtain a sensor response which is independent of both intensity fluctuations of the light source and physical changes in the sol-gel matrix comprising the spots.

8.4.2 Experimental

Template fabrication

It was decided to employ UV laser writing of a SU-8 layer to fabricate the template for the Y-splitter (see Chapter 4, Sec. 4.3.4 for a description of the UV laser writing setup). Sec. 8.5.2 describes the steps involved in the deposition of a typical SU-8 layer. In this case, the photoresist was deposited on a silicon wafer by spin-coating at 3000 rpm, after which it was soft-baked in order to evaporate solvent from the layer in preparation for the laser writing step. The coated Si

wafer was mounted on the motorised XY-stage, which was programmed to move to coordinates defining an optical Y-splitter. The splitter was designed using BPM/CAD software (Prometheus, BBV Software, The Netherlands) that also produced a DXF design file. This file was imported into the laser writing control system, thereby providing the coordinates for the XY stage. The SU-8 layer was crosslinked upon exposure to the stationary beam spot of the Helium-Cadmium laser used, enabling the Y-splitter configuration to be written into the photoresist. The sample was subsequently post-baked as described in Table 8.1, Sec. 8.5.2 and developed to produce the Y-splitter template shown in Fig. 8.7. The template was examined by profilometry that measured the height of the structure (defined by the coating parameters) as approximately 80μm and the width of a single ridge (defined by the diameter of the laser beam spot) as approximately 80μm.

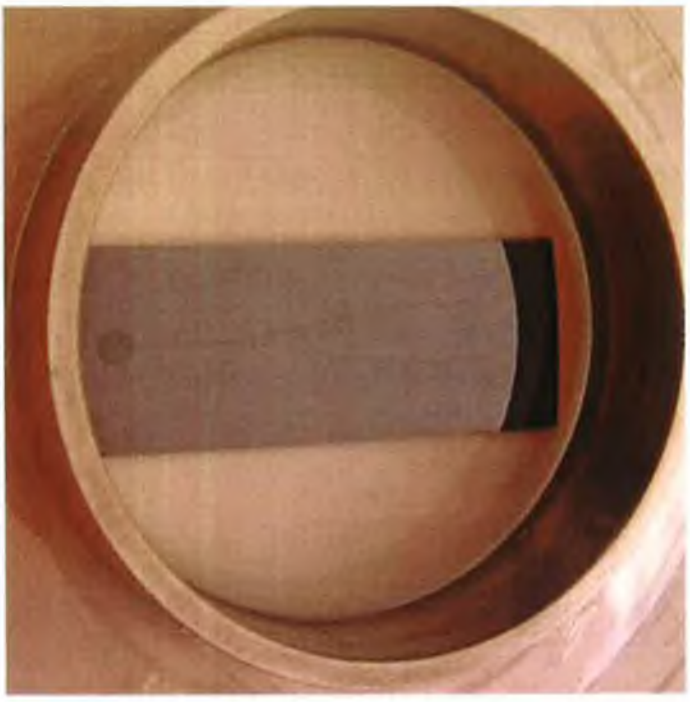

Figure 8.7: SU-8 Y-splitter template (image taken during PDMS moulding step).

Production of PDMS Y-splitter mould

PDMS was prepared as described in Chapter 4, Sec. 4.1.1 and cast against the SU-8 template. The template was silanised prior to this step in order to facilitate removal of the cured PDMS mould (see Chapter 4, Sec. 4.1.4 for a description

of the silanisation procedure). A short length of rubber tubing was glued to the circular disk at the input arm of the template before moulding to define an inlet channel for the sol that was to be patterned by capillary action. After casting, the PDMS was allowed to degas in ambient conditions before curing.

Preparation of UV-curable sol

It was decided to employ UV-curable sol-gel [7] as the ridge waveguide material. The substrate most commonly employed for the fabrication of such structures is silicon due to its ability to be cleaved cleanly, thereby producing waveguide endfaces of optical quality. However, due to the high refractive index of silicon (n>3.4) it was necessary to first deposit a buffer layer which acted as an interface for total internal reflection of light propagating along the guiding layer. To this end two sols were prepared, one to provide a buffer layer and the other to act as the higher index guiding layer.

1. Preparation of buffer layer sol

   The buffer layer sol was prepared by mixing tetraethyl orthosilicate (TEOS), 3-(methoxysilyl)propyl methacrylate (MAPTMS) and water to allow for the hydrolysis of the silica precursors. HCl was added to catalyse the reaction. The photopatternability of the sol was achieved by adding a photoinitiator (Irgacure 1800, Ciba Speciality Chemicals) to the sol and allowing it to stir until completely dissolved.

2. Preparation of guiding layer sol

   The guiding layer sol was prepared in a manner identical to the buffer layer with one additional step. Zirconium propoxide complexed with methacrylic acid (MAA) was added to increase the refractive index of the guiding layer relative to the buffer layer. The function of the complexing agent MAA was to prevent the formation of Zr clusters in the sol due to the differing rates of hydrolysis and condensation of the zirconium and silica precursors. The reaction rates for silica and zirconia precursors were thus comparable, which resulted in homogenous materials.

Fabrication of UV sol-gel-based Y-splitter by MIMIC

Micromoulding in capillaries (MIMIC) has been used in several applications including the fabrication of field effect transistors [8] and ridge waveguides [9]. However, it has not, to our knowledge, been used to pattern UV curable sol-gel materials for optical sensing applications. The principle of the technique is described in Chapter 4, Sec. 4.1.2, and involves the use of capillary action to draw the desired material into a PDMS mould that is in conformal contact with the substrate to be patterned.

The choice of UV-curable sol-gel for waveguide fabrication was influenced by several factors, including the ability to create dense sol-gel structures of high optical quality without the need for a high temperature annealing stage, the ease with which the material refractive index can be modified and the high film thickness achievable when using such a material. While it is possible to modify the refractive index of non-photocurable sol-gel materials such as those derived from TEOS and MTEOS, it is not possible to produce films of the thickness required for this application (i.e., for the fabrication of multimode ridge waveguide structures), nor is it possible to produce dense optical structures without the use of a high temperature annealing process that would destroy the PDMS mould. The use of such an annealing step would necessitate the removal of the PDMS mould after having first permitted the material to dry at a lower temperature, introducing an extra stage to the fabrication protocol and increasing overall chip production time.

In order to fabricate the Y-splitter, the PDMS mould was brought into contact with a silicon wafer onto which a UV-curable sol-gel buffer layer had been deposited by spin-coating. A drop of UV-curable guiding layer sol was placed at the entrance to the PDMS mould defined by the circular inlet and then proceeded to fill the mould by capillary action. Both mould and substrate were exposed to UV radiation from a broadband source (UV Light Technology Ltd., U.K.) for 5 hours. The duration of the exposure was dependent on the thickness of the sol-gel ridges defined by the mould and on the rate of polymerisation of the sol itself. This step was followed by a thermal crosslinking process that consisted of a 30 minute hard-bake at 80°C using a contact hot plate. The PDMS mould was then peeled from the substrate leaving the crosslinked ridge waveguides on the

buffer layer. The samples were then cleaved to provide endfaces of optical quality before sensor spot deposition.

Sensor spot deposition

Sensor and reference spots were deposited by PDMS stamp printing, using a stamp with a 1mm diameter (see Sec. 8.2 for a description of this technique). The sensor spot consisted of a sol-gel matrix doped with Bromocresol purple, while the reference spot consisted of an identical, yet undoped sol-gel matrix. The sol-gel formulation employed here was identical to that described in Chapter 7, Sec. 7.2.1. Fig. 8.8 (a) is a digital photo of the stamp-printed sensor and reference spots, while Fig. 8.8 (b) is an image of the splitter and spots taken using a CMOS camera. The latter image is inverted with respect to the former due to the imaging optics of the CMOS camera. Discrete spots are evident on both arms of the Y-splitter and have been manually outlined in Fig. 8.8 (b).

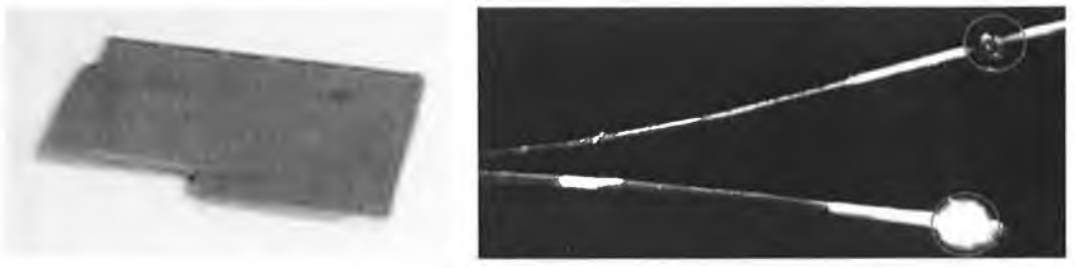

(a) (b)

Figure 8.8: Image of stamp-printed spots on arms of optical Y-splitter taken (a) using a digital camera and (b) using a CMOS camera

8.4.3 Results and Discussion

In order to ascertain the quality of the micromoulded Y-splitter, it was necessary to investigate its guiding efficency. To this end, the sample was incorporated into a CCD imaging setup and light from a red laser diode was coupled by end-firing into the input arm of the splitter. Fig. 8.9 shows the acquired image.

There is clearly a significant amount of scattering at the junction of the Y-splitter and this was found to be due to a defect in the SU-8 template caused by a double-exposure during the laser writing process. This resulted in the junction

Figure 8.9: CCD image of light coupled from red laser diode to micromoulded Y-splitter. Double-exposed region at junction circled.

being thicker than the other sections of the splitter, meaning that an excess amount of UV-curable sol-gel gathered at that point during the moulding stage. The resultant non-uniform polymerisation across this section compared with the rest of the splitter was thought to have caused a difference in the refractive indices of these sections, resulting in the scattering shown in Fig. 8.9.

The poor guiding efficiency of the Y-splitter meant that it could not be used as a viable pH sensor due to the low light levels detectable at its outputs. However, the work clearly showed the viability of patterning UV-curable sol-gel in a ridge waveguide configuration by MIMIC but that the master fabrication process needed to be optimised or an alternative chosen in order the obtain an effective sensor. The following section describes the development of an integrated sensor chip that was fabricated using the same soft lithographic techniques employed here, combined with a more effective template fabrication procedure.

8.5 Development of an integrated optical oxygen sensor

8.5.1 Background

Several recent publications have highlighted the use of rapid prototyping techniques for the fabrication of miniaturised optical sensor platforms. These include the development of sensors for phosphorus [10], copper [11] and dissolved oxygen [12].

This section describes the development of an integrated oxygen sensor using a

combination of soft lithography and high precision patterning. The development protocol reported here can be characterised by its ease of implementation, the efficiency of the resultant sensor and its suitability for the development of a fully integrated sensor chip. Soft lithographic techniques were foremost in the fabrication of this sensor chip and, as such, this work serves to showcase the suitablilty of these techniques for the production of optical sensor platforms.

The sensor chip concept adopted here is illustrated in Fig. 8.10. The oxy-

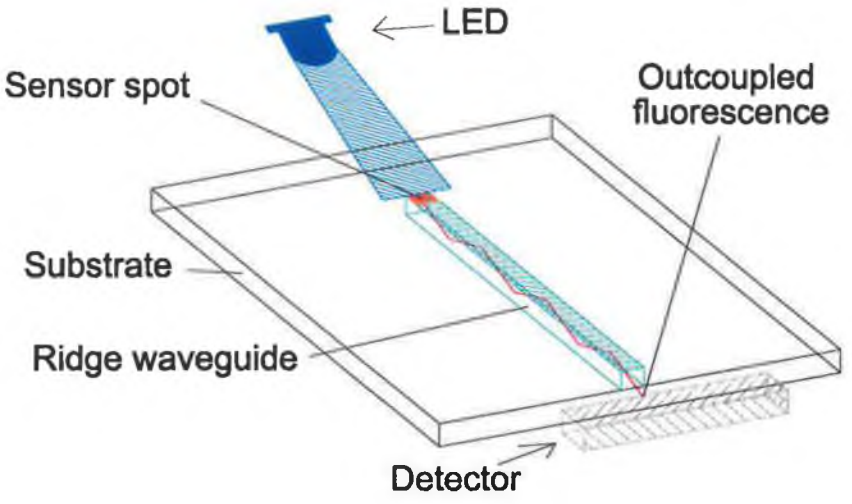

Figure 8.10: Oxygen sensor concept.

gen sensing mechanism is based on the quenching of fluorescence from a sol-gel encapsulated ruthenium complex. A sol-gel sensor spot is deposited onto a multimode ridge waveguide and the ruthenium complex is excited directly using a LED source. The use of direct excitation is an important design feature of the sensor chip as it is considerably more efficient than evanescent-wave excitation. Furthermore, the resultant fluorescence is coupled with high efficiency into the waveguide and propagates along its length to be detected at the endface using an appropriate detector [13, 14]. Changes in oxygen concentration result in a modulation of the detected output intensity (or decay time), thereby providing the basis for the sensor.

Fig. 8.11 is a flowchart of the fabrication protocol used to produce the sensor chip. The first stage was the fabrication of a template for the ridge waveguide from SU-8 photoresist. A PDMS mould of this template was produced and employed to pattern a UV-curable sol-gel ridge waveguide by MIMIC. Crosslinking

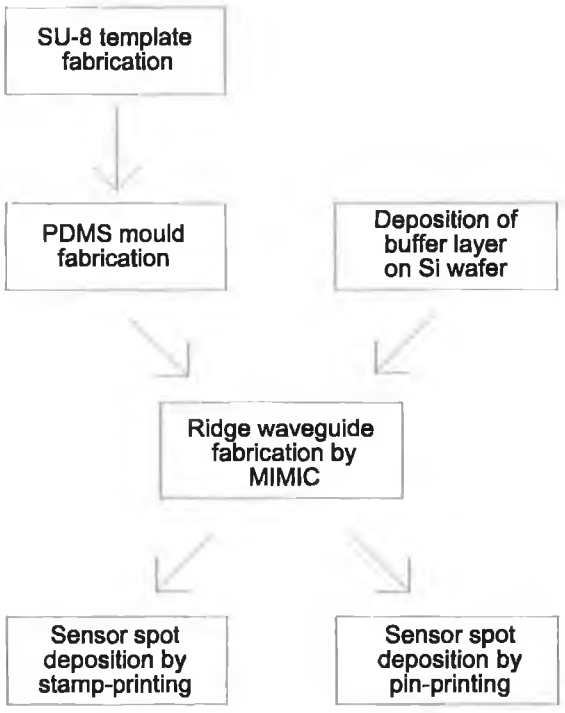

Figure 8.11: Flowchart of sensor fabrication protocol.

of the photocurable sol-gel was achieved by exposure to UV radiation while it is confined within the PDMS mould. A sensor spot was then deposited on the ridge waveguide. Here, two different deposition techniques for the sensor spot were compared, namely stamp-printing and high-resolution pin-printing. The resultant sensor chip was then incorporated into a custom-made flowcell and exposed to varying concentrations of oxygen.

The advantages of this approach over that reported in [12] include the elimination of a fibre-coupling strategy for signal excitation and detection, a much less complex sensor layer deposition process and the ability to produce many sensor chips using only one high-precision photolithographic step for template fabrication. The use of sol-gel technology for the production of oxygen-sensitive spots also makes it possible to tune the sensitivity to specific ranges through correct choice of precursor, lending a greater degree of flexibility to the sensor development process. This is a major advantage over other immobilisation strategies.

8.5.2 Experimental

Fabrication of SU-8 ridge waveguide template

The use of SU-8 photoresist as a material for microsystems fabrication has been widespread in recent years due to the broad range of film thicknesses that can be deposited and the mechanical stability of the crosslinked polymer [15, 16]. It is, therefore, an attractive choice for the fabrication of high quality microsystems templates for use as masters in soft lithographic applications. SU-8 photolithography has been described in Chapter 4, Sec. 4.3.2.

Prior to film deposition, the silicon wafer that was to act as the substrate was pre-treated in order to promote film adhesion and uniformity. Three methods were investigated to this end, namely air plasma treatment, sonication in an aqueous solution of detergent and a Piranha etch.

The air plasma treatment was similar to that described for the surface modification of PS waveguide platforms (see Chapter 7, Sec. 7.3.1) and involved exposing the Si wafer to the plasma for 60s, directly after which it was coated with the SU-8 layer by spin-coating.

The sonication procedure consisted of two steps, the first being sonication of the wafer while immersed in a solution of deionised water and a commercially available detergent, the second, a sonication stage of equal duration in pure deionised water. The wafer was dried by pooling isopropanol (IPA) on its upper surface and spinning it at 1000rpm for 30s using the spin-coater, after which it was ready for photoresist deposition.

The Piranha etch necessitated the preparation of a bath of Piranha solution, which was achieved by adding concentrated sulphuric acid (H_2SO_4) to hydrogen peroxide (H_2O_2, 27.5% wt. solution in water) in a 5:1 ratio by volume (acid:peroxide). The Si wafer was then immersed in this solution for 1 hour and was subsequently rinsed with deionised water and dried using IPA as described in the previous paragraph. It was this pre-treatment method that proved to be most effective for the deposition of a uniform layer of SU-8.

A film of SU-8 2075 (Chestech, U.K.) was deposited on the silicon substrate by spin-coating. The coating process was designed to produce a film 100μm thick. After deposition, the film was soft-baked in a two-step contact hot plate process and then allowed to cool slowly. This step was followed by exposure of the film

through the appropriate mask using a Karl Suss contact mask aligner. The sample was then post-baked using a similar process to that described for the soft-bake after which it was developed under sonication for 10 minutes. The developer used was EC solvent (Chestech, U.K.). Table 8.1 lists the process parameters chosen in order to produce the master desired for this application.

Parameter	Value
Deposition parameters	
Ramp time (s)	7
Spin speed (rpm)	2200
Hold time (s)	30
SU-8 processing parameters	
Soft bake temperature - A (°C)	65
Time - A (mins)	5
Soft bake temperature - B (°C)	95
Time - B (mins)	20
Exposure time (s)	90
Post-exposure bake temperature - A (°C)	65
Time - A (mins)	2
Post-exposure bake temperature - B (°C)	95
Time - B (mins)	15
Development time (mins)	10

Table 8.1: Parameters for the fabrication of the SU-8 ridge waveguide template.

Fig. 8.12 shows an image of the SU-8 ridges formed taken using a Hitachi S-3000N scanning electron microscope. The near-square profile of the ridges is apparent with the average ridge measuring 100μm $\pm$1μm in width $\times$ 95μm $\pm$2μm in height. The discrepancy between the expected and measured ridge height is due to the spin-coating process, which would require some further tailoring to facilitate the fabrication of square waveguides.

Fabrication of PDMS ridge waveguide mould

In order to fabricate the PDMS mould for this application, liquid prepolymer was cast against the SU-8 ridge waveguide master and allowed to degas in ambient

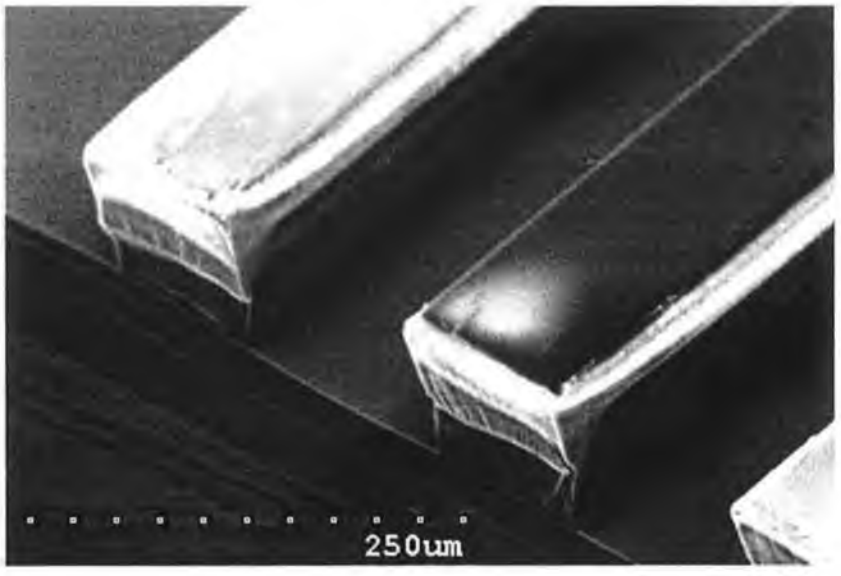

Figure 8.12: SEM image of SU-8 ridge waveguide template.

conditions. The PDMS was then cured at 70C for 1 hour before being peeled from the master. It should be noted that the SU-8 master was first silanised to facilitate lift-off of the cured PDMS mould without causing damage to the master. Silanisation was achieved using the procedure outlined in Chapter 4, Sec. 4.1.4. The mould was then cleaved to provide an opening that facilitated capillary action (see Sec. 8.5.2).

Preparation of sensor sol

The formulation employed for the production of an oxygen sensitive membrane is identical to one reported previously for a sol-gel film for optical sensing of oxygen [17]. The oxygen-sensitive complex, Tris-(4,7-diphenyl)-1,10-phenanthroline ruthenium (II) chloride ($Ru(dpp)_3Cl_2$), was dissolved in ethanol and mixed with pH 1 hydrochloric acid (HCl) whilst stirring. The required amount of methyltriethoxysilane (MTEOS), the sol-gel precursor, was then added and the mixture was stirred for 4 hours at room temperature. The film was then deposited by both stamp-printing and pin-printing on the ridge waveguides and cured at 70°C for 18 hours.

Preparation of UV-curable sol

This formulation was prepared as described in Sec. 8.4.2.

Patterning of UV-curable sol-gel ridge waveguides by MIMIC

The MIMIC procedure was carried out as described in Sec. 8.4.2. As shown in Fig. 8.12, the SU-8 template consisted of an array of ridge waveguides approximately 100μm x 100μm. One can pattern a full waveguide array using this technique and, using multiple PDMS moulds, it is possible to produce many times the original number of waveguides simultaneously having fabricated just one template. However, for the purposes of sensor fabrication it was necessary to pattern only one waveguide. Mould filling was usually achieved in less than 1 minute. The samples were again cleaved before sensor spot deposition. The average length of a cleaved ridge waveguide was 8mm.

Another important advantage of using MIMIC to pattern UV-curable sol-gel waveguides is the ability to produce much thicker waveguides than is possible by spin-coating the current sol-gel formulation and using conventional photolithography. By making the waveguides thicker, the number of modes they can support is increased, which leads to an increased signal level and improved sensor performance. The waveguides patterned for this application were approximately five times thicker than those currently fabricated by conventional photolithography.

Deposition of sensor spots

Sensor spots were deposited by PDMS stamp-printing and high-resolution pin-printing. In the case of stamp-printing, the PDMS patterning element described in Sec. 8.3 was used to transfer a drop of sol onto the upper surface of a ridge waveguide. Due to the dimensions of the stamp, sensor spots produced by this method typically covered a large fraction of the length of the waveguide. High-resolution pin-printing was achieved using a Cartesian Technologies MicroSys 5100 MicroArrayer (Genomic Solutions, UK). With this device it was possible to deposit uniform spots measuring 60μm in diameter onto the upper surface of the sol-gel ridge waveguides. Fig. 8.13 (a) shows a typical sensor spot deposited by pin-printing onto the upper surface of a ridge waveguide while Fig. 8.13 (b) shows the fluorescence from the same spot under illumination by a blue LED.

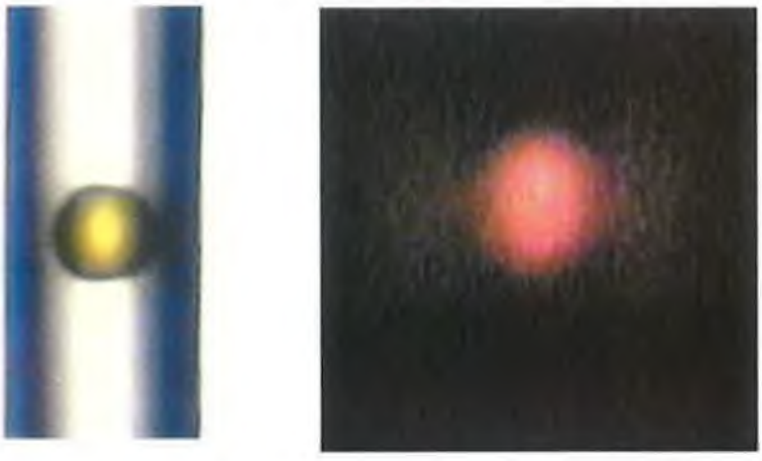

(a) (b)

Figure 8.13: Image of pin-printed spot on upper surface of ridge waveguide (a) in white light and (b) under optical excitation from a blue LED

Both images were recorded using an Olympus BX51M video microsope with a gel filter being employed to remove excitation light in the case of the latter image.

Oxygen sensor system

The sensing mechanism is based on the quenching of the fluorescent indicator dye , $Ru(dpp)_3Cl_2$, in the presence of oxygen. This oxygen quenching process is described by the Stern Volmer Equation:

$$\frac{I_0}{I} = 1 + K_{SV}[O_2] \tag{8.1}$$

where K_{SV} is the Stern Volmer constant, $[O_2]$ is the oxygen concentration and the term I_0/I is the ratio of the the maximum fluorescence intensity, i.e., that obtained for 0% oxygen, relative to the fluorescence intensity at each oxygen concentration.

The experimental setup used in this work is shown in Fig. 8.14.

The silicon substrate bearing the ridge waveguide was placed in a custom-made flowcell through which varying mixtures of oxygen and nitrogen were passed. Gas concentrations were regulated using mass flow controllers (Celerity, Ireland). Excitation of the sensor spots was accomplished using a blue LED (Nichia NSPB500S, λ_{max} = 470nm), which was incorporated into the flowcell itself and

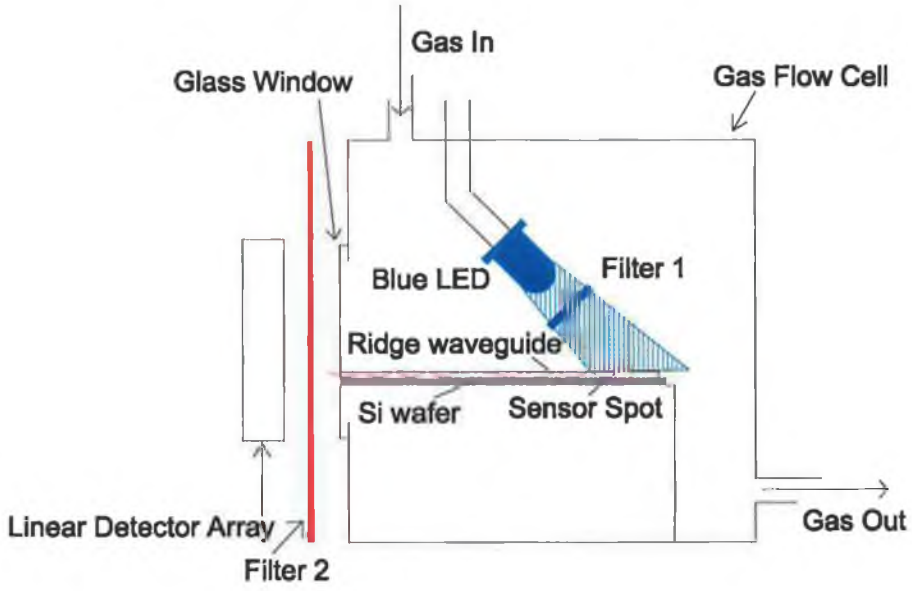

Figure 8.14: Experimental setup.

the output fluorescence from the waveguides was detected using a linear detector array (LDA - Hamamatsu, Japan). A Schott BG12 glass bandpass filter (Filter 1) was used to eliminate the higher wavelength tail from the blue LED. A LEE 135 gel filter (Filter 2) was used to eliminate excitation light from the detected output signal The output from the LDA displayed the light intensity detected as a function of channel number, i.e., the position along the LDA at which the light was detected. This makes it possible to distinguish between the outputs of several ridge waveguides according to their position on the sensor chip. Therefore, using the same detector, it is possible to develop a multianalyte sensor based on a ridge waveguide array with each waveguide carrying a sensor spot for a different analyte.

8.5.3 Results and Discussion

Stamp-printed sensor performance

Fig. 8.15 shows the signal traces recorded by the LDA (using a 1s integration) upon exposure of a stamp-printed ridge waveguide sample to varying concentrations of gaseous oxygen. Data acquisition for each concentration was completed in 50s, during which time 50 data points were acquired and the mean value plotted

at the end of each scan. The data acquisition software also generated a spreadsheet file containing the intensity values recorded for each channel number every second along with the maximum, minimum, mean and standard deviation (σ) associated with each set of intensity values. It should be noted that the "Channel number" referred to on the x-axis corresponds to the position along the detector array. Consequently, the recorded trace is a plot of the horizontal distribution of the output fluorescence intensity as measured by the LDA. Maximum signal (i.e., maximum fluorescence intensity) was observed at 0% O_2 with subsequent, increasing concentrations resulting in reduced signal levels, clearly demonstrating the oxygen-sensitivity of the sample.

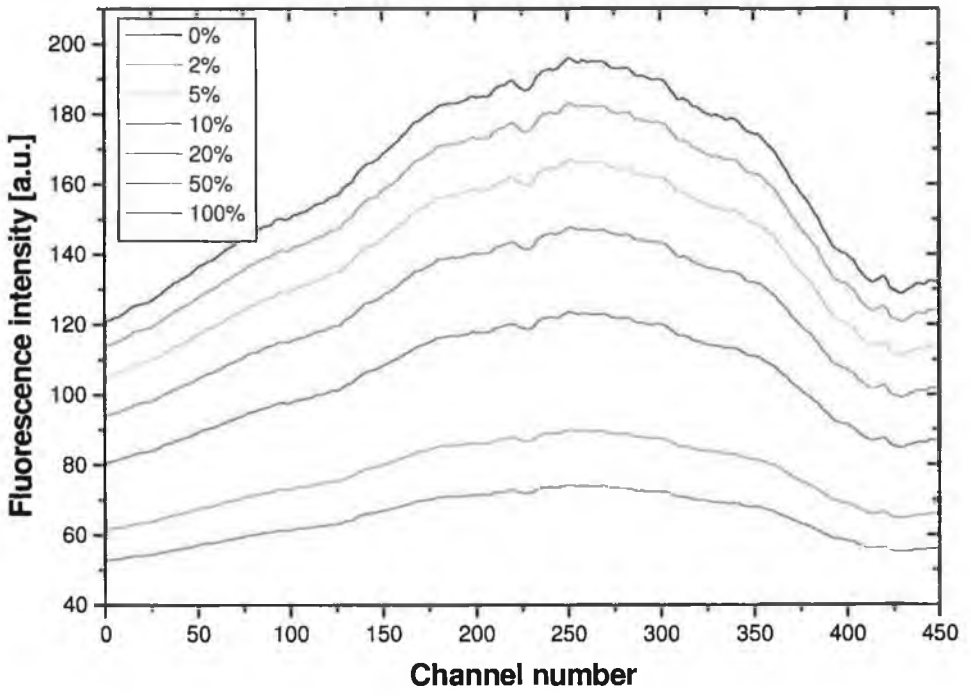

Figure 8.15: Stamp-printed sensor response to varying concentrations of gaseous oxygen.

The calibration curve of the sample is shown in Fig. 8.16. This was obtained by plotting the fluorescence intensity for the channel number corresponding to the signal peak of the recorded traces as a function of oxygen concentration. In this case, maximum intensity for each concentration was detected at channel number 260 and it is these values that were used to generate the sensor calibration curve.

Using the 3σ noise level (determined by calculating the average standard

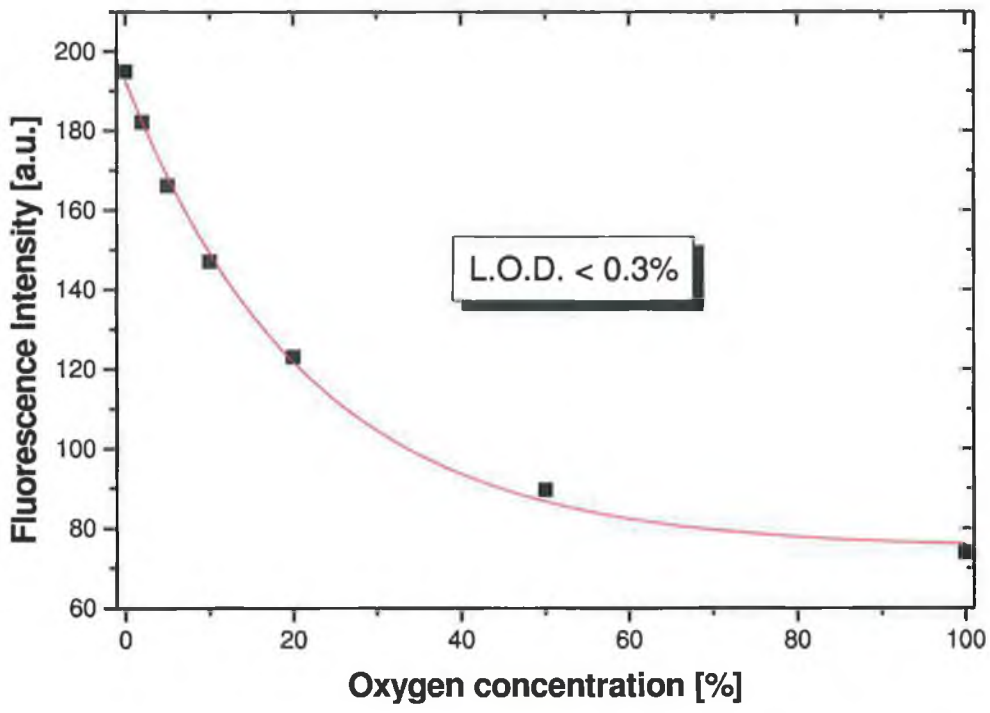

Figure 8.16: Calibration curve for stamp-printed sensor (1s integration time).

deviation, $\overline{\sigma}$, of the recorded data for channel 260 and two adjacent channels), it was possible to calculate a limit of detection (L.O.D.) for gaseous oxygen of less than 0.3% and a resolution of less than 0.6% over the range 0% to 20%. Taking into account an equivalent dissolved oxygen (DO) concentration of 9.2 ppm for air saturated water, this would correspond to a L.O.D. of approximately 150 ppb and a resolution of 250 ppb over the range 0 ppm to 9.2 ppm if the sensor were deployed in dissolved phase.

Pin-printed sensor performance

The calibration curve of a pin-printed is illustrated in Fig. 8.17. In this case, an integration time of 10s was employed for data acquisition due to the lower levels of fluorescence present compared with stamp-printed samples.

The sensor has a L.O.D. of 0.65% for gaseous oxygen and a resolution of 1% over the range 0% to 20%. This corresponds to an equivalent L.O.D. for DO of approximately 300ppb and a resolution of less than 500ppb over the range 0ppm to 9.2ppm

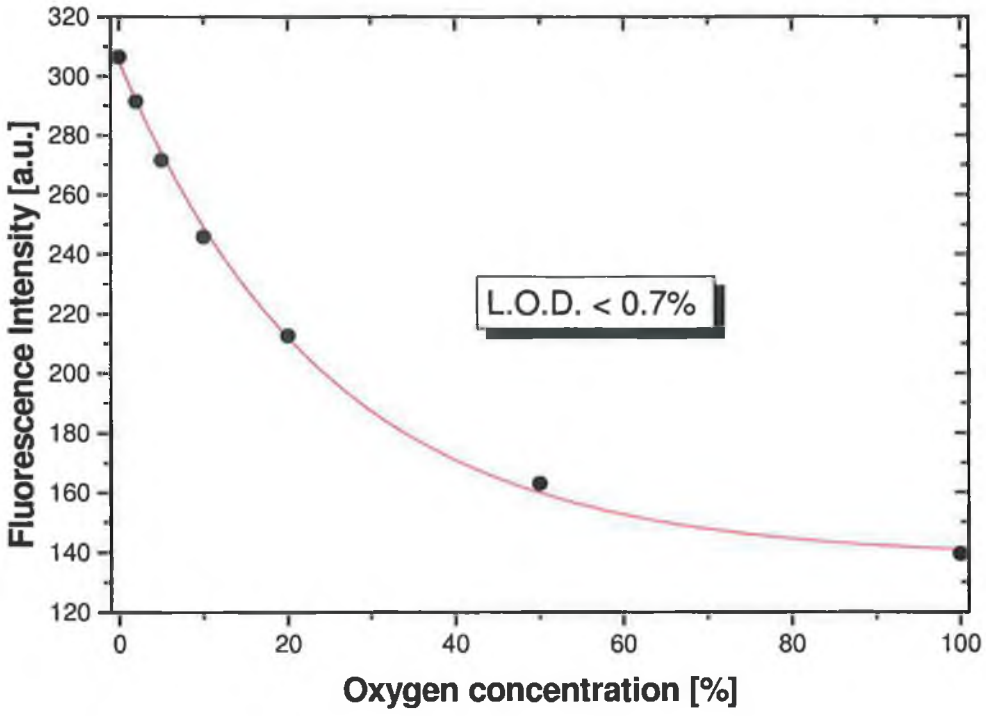

Figure 8.17: Calibration curve for pin-printed sensor (10s integration time).

Comparison of sensor performances

The oxygen-sensitive response is clearly demonstrated for both samples and the resultant Stern-Volmer plots are shown in Fig. 8.18. The advantage of stamp-printing is that it yields a relatively high signal level due to the larger spot size, facilitating the use of shorter integration times. The stamp-printed sensor also demonstrates improved sensitivity compared with the pin-printed sensor. This is thought to be due to the increased porosity of the sol-gel layer yielded when drying the thicker film. This results in enhanced film permeability, which facilitates improved dye accessibility to the oxygen molecules and, consequently, superior quenching characteristics. However, the lack of reproducibility mentioned earlier makes this technique suitable for proof of principle applications only. The automated pin-printing process, on the other hand, facilitates a high level of reproduciblity as far as sensor spot deposition is concerned. Furthermore, the results yielded by these sensors compare favourably with those reported in [12] where a maximum resolution of 600ppb was obtained over the range 0.8ppm to 24.8ppm.

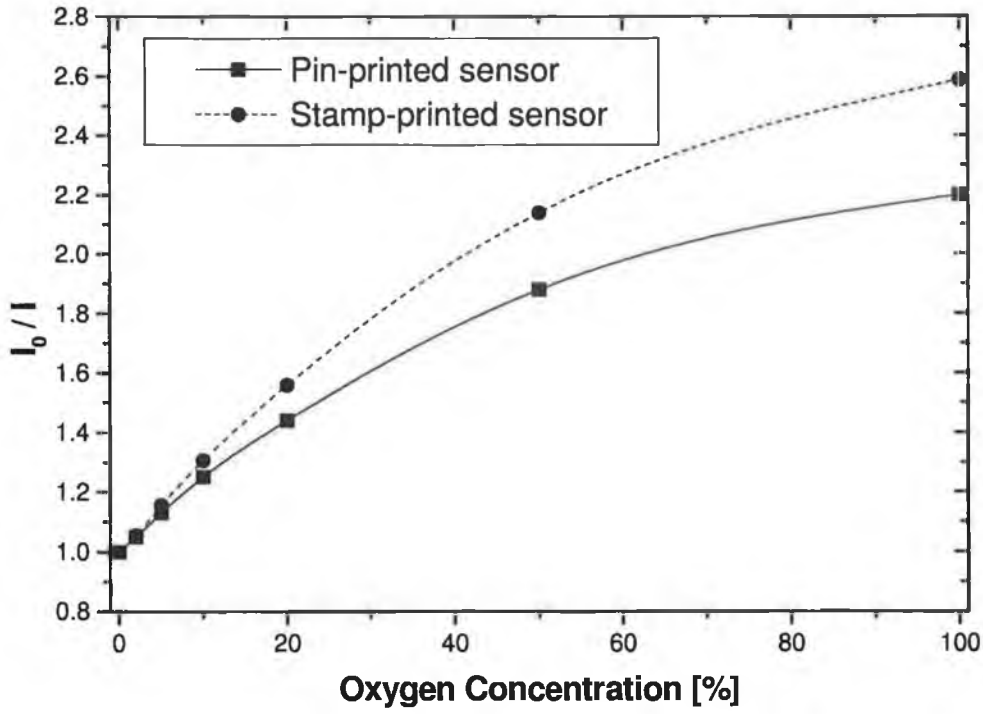

Figure 8.18: Stern-Volmer plots yielded by both stamp-printed and pin-printed sensor chips.

8.5.4 Summary

This section has described the development of a highly sensitive platform for the detection of gaseous oxygen that exploits both soft lithographic fabrication techniques and high accuracy micropatterning technology.

The sensor presented here displays comparable sensitivity to a recently reported system over the same concentration range and outperforms it in terms of resolution over lower concentration ranges. This was achieved by employing a far less complex fabrication protocol and resulted in a more compact, robust and miniaturisable sensor system that is well suited for lab-on-a-chip applications outside a laboratory environment.

8.6 Conclusions

Soft lithographic techniques have been applied to the fabrication of a variety of optical structures with applications in optical sensing. It has been shown that, not

only do these techniques simplify the fabrication process, but they yield improved results compared with conventional methods. This was demonstrated in the case of sol-gel grating coupler fabrication and, in particular, by the development of the integrated optical oxygen sensor described in the previous section.

The rapid production of systems for proof of principle applications is another advantage provided by the use of soft lithography, e.g., discrete sensor spot deposition by PDMS stamp printing and the patterning of UV-curable sol-gel ridge waveguides five times thicker than previously possible by MIMIC.

The use of rapid prototyping technologies such as soft lithography is central to the development of low-cost, disposable microsensors for lab-on-a-chip applications without the need to compromise on sensitivity when compared to more complex sensor configurations.

The work reported here is representative of the growing trend towards the use of rapid prototyping technology for the development of miniaturised sensor platforms and clearly demonstrates the capability of these techniques in the production of efficient devices.

Bibliography

[1] I. A. Avrutsky, A. S. Svakhin, V. A. Sychugov, and O. Parriaux, "High-efficiency single-order wave-guide grating coupler," *Optics Letters*, vol. 15, no. 24, pp. 1446–1448, 1990.

[2] S. I. Najafi, *Introduction to Glass Integrated Optics.* Boston: Artech House, 1992.

[3] T. Tamir, *Guided-Wave Optoelectronics, Second Edition.* New York: Springer-Verlag, 1990.

[4] C. Malins, A. Doyle, B. MacCraith, F. Kvasnik, M. Landl, P. Simon, L. Kalvoda, R. Lukas, K. Pufler, and I. Babusik, "Personal ammonia sensor for industrial environments," *Journal of Environmental Monitoring*, vol. 1, pp. 417–422, 1999.

[5] S. Choquette, B. Ramos, and N. F. Jr., "Embossable grating couplers for planar waveguide optical sensors," *Analytical Chemistry*, vol. 68, no. 7, pp. 1245–1249, 1996.

[6] L. Polerecky, J. Hamrle, and B. D. MacCraith, "Theory of the radiation of dipoles placed within a multilayer system," *Applied Optics*, vol. 39, no. 22, pp. 3968–3977, 2000.

[7] P. Ayras, J. T. Rantala, S. Honkanen, S. B. Mendes, and N. Peyghambarian, "Diffraction gratings in sol-gel films by direct contact printing using a uv-mercury lamp," *Optics Communications*, vol. 162, no. 4-6, pp. 215–218, 1999.

[8] J. Hu, R. Beck, T. Deng, R. Westervelt, K. Maranowski, A. Gossard, and G. Whitesides, "Using soft lithography to fabricate GaAs/AlGaAs heterostructure field effect transistors," *Applied Physics Letters*, vol. 71, no. 14, pp. 2020–2022, 1997.

[9] A. Stoddart, X.-M. Zhao, S. Smith, E. Kim, Y. Xia, M. Prentiss, and G. Whitesides, "Fabrication of single-mode polymeric waveguides using micromolding in capillaries," *Advanced Materials*, vol. 8, no. 5, pp. 420–424, 1996.

[10] M. Bowden, O. Geschke, J. P. Kutter, and D. Diamond, "CO2 laser microfabrication of an integrated polymer microfluidic manifold for the determination of phosphorus," *Lab on a Chip*, vol. 3, no. 4, pp. 221–223, 2003.

[11] E. Tyrrell, C. Gibson, B. D. MacCraith, D. Gray, P. Byrne, N. Kent, C. Burke, and B. Paull, "Development of a micro-fluidic manifold for copper monitoring utilising chemiluminescence detection," *Lab on a Chip*, vol. 4, 2004.

[12] D. A. Chang-Yen and B. K. Gale, "An integrated optical oxygen sensor fabricated using rapid-prototyping techniques," *Lab on a Chip*, vol. 3, pp. 297–301, 2003.

[13] J. F. Gouin, A. Doyle, and B. D. MacCraith, "Fluorescence capture by planar waveguide as platform for optical sensors," *Electronics Letters*, vol. 34, no. 17, pp. 1685–1687, 1998.

[14] M. Feldstein, B. MacCraith, and F. Ligler, "Integrating multi-waveguide sensor," October 24th 2000, U.S. Patent No. 6,137,117.

[15] H. K. Chang and Y. K. Kim, "UV-LIGA process for high aspect ratio structure using stress barrier and c-shaped etch hole," *Sensors and Actuators a-Physical*, vol. 84, no. 3, pp. 342–350, 2000.

[16] J. Zhang, K. L. Tan, and H. Q. Gong, "Characterization of the polymerization of SU-8 photoresist and its applications in micro-electro-mechanical systems (mems)," *Polymer Testing*, vol. 20, no. 6, pp. 693–701, 2001.

[17] C. McDonagh, A. McEvoy, and B. MacCraith, "Dissolved oxygen sensor based on fluorescence quenching of oxygen-sensitive ruthenium complexes immobilized in sol-gel derived porous silica coatings," *The Analyst*, vol. 121, pp. 785–788, 1996.

Chapter 9

Conclusions

A combination of rapid prototyping and polymer processing technology has been used to develop a variety of platforms for optical sensing applications. Dedicated sensor enhancement strategies were applied to the design and fabrication of these platforms. In particular, enhanced polymer waveguide platforms for absorption-based optical chemical sensing applications were developed and soft lithography has been applied to the fabrication of a number of optical structures with applications in optical sensing.

The objectives of this work (as described in Chapter 1) were realised.

1. An outline of the theoretical analysis formulated with respect to planar optical absorption-based sensors was presented and verified experimentally.

2. A LED-based prototype sensor was subsequently fabricated. This prototype exhibited an enhanced performance compared to other, more complex sensor configurations, both as an ammonia sensor and a pH sensor.

3. The enhancement strategy was applied to the development of mass-producible polymer waveguide platforms, which were fabricated by micro-injection moulding. These platforms formed the basis of an optical ammonia sensor that was a significant improvement on previously reported systems, specifically in terms of ease of fabrication and device sensitivity. It was also possible to verify, albeit empirically, the predictions of the aforementioned theoretical analysis as it pertained to the dependence of platform sensitivity on interaction length. The results presented here have significant implications

for the design of efficient, potentially disposable sensor platforms and highlighted the possibility of enhanced sensitivity through miniaturisation of the sensing element.

4. Soft lithographic techniques were implemented successfully in the fabrication of a variety of optical structures including sol-gel grating couplers, discrete sensor spots and UV-curable sol-gel ridge waveguides.

5. The advantages of soft lithography were effectively showcased by the development of an integrated optical oxygen sensor that combined an enhanced fluorescence excitation strategy with a micromoulded ridge waveguide and a pin-printed sensor spot. This platform exhibited high sensitivity and an overall improvement in performance characteristics compared with recently reported systems.

Future work should involve the fabrication of enhanced polymer sensor chips employing a single reflection configuration for optical absorption-based sensing applications. Optimisation of the micro-injection moulding process would be required in order to produce chips of high optical quality. The use of a single reflection configuration would allow for further miniaturisation of the overall sensor head without loss in sensitivity, assuming an adequately high sensing layer absorption coefficient. Alternative sensing chemistries for the optical detection of ammonia and pH should also be examined, e.g., polyaniline-based sensing layers. It is believed that such sensors will not suffer from the instabilities associated with the reagent-based systems presented in this work. The soft lithographic technique of μTM should be investigated with a view to the fabrication of discrete optical components from UV-curable sol-gel along with the fabrication of ridge waveguides, the lengths of which would not be limited by capillary flow within the PDMS mould. Microcontact printing could be applied to the patterning of metallic nanoislands for fluorescence enhancement purposes and the development of on-detector sensing platforms with integrated optical elements through the use of PDMS monoliths should also be examined. Such platforms would provide "modular" and efficient sensor systems at low-cost, whilst eliminating many of the optical alignment issues associated with more complex sensor configurations.

List of publications and conference presentations

Oral presentations

1. "Optical Ammonia Sensor Employing a Planar Waveguide Platform.", Photonics East, Nov 5-8 2000, Boston, U.S.A.

2. "Optical ammonia sensor based on a polymer multimode waveguide platform.", Europt(r)ode VI, April 7-11 2002, Manchester, U.K. (presented by supervisor).

3. "Enhanced polymer waveguide platforms for absorption-based optical chemical sensors", Opto-Ireland, Sept 5-6 2002, Galway.

4. "Production of optical microsystems using soft lithography.", Opto-Ireland, Sept 5-6 2002, Galway.

Poster presentations

1. "Applications of Soft Lithography in the Optical Sensing Domain.", Europt(r)ode V, April 16-19 2000, Lyon - Villeurbanne, France.

2. "Optimisation of waveguide platforms for absorption-based sensors.", Europt(r)ode V, April 16-19 2000, Lyon - Villeurbanne, France.

3. "Optical Chemical Sensor Systems based on Photosensitive Hybrid Sol-gel Glass.", Sol-Gel 2001, 16-21 September 2001, Abano Terme, Italy.

4. "Performance of optical absorption-based sensors employing multimode waveguide platforms - single versus multiple reflection configurations.", Europt(r)ode VI, April 7-11 2002, Manchester, U.K.

5. "Enhanced polymer platforms for absorption-based optical chemical sensors.", Institute of Physics in Ireland - 32nd Spring Weekend Meeting, 11-13 April 2003, Westport, Co. Mayo.

6. "Development Of A Sol-Gel Based Integrated Optical Oxygen Sensor Using Rapid Prototyping Technology." BOC Gases Poster Competition, April 14 2004, Dublin City University.

Publications

1. L. Polerecky, C. S. Burke and B.D. MacCraith, "Optimization of absorption-based optical chemical sensors that employ a single-reflection configuration", *Appl. Opt.*, Vol. 41, No. 15, pp. 2879-2887, 2002.

2. C. S. Burke, L. Polerecky and B.D. MacCraith, "Enhanced polymer waveguide platforms for absorption-based optical chemical sensors" , Opto-Ireland 2002: Optics and Photonics Technologies and Applications, *Proc. of SPIE*, Vol. 4876, pp. 848-885, 2002.

3. E. Tyrrell, C. Gibson, B. D. MacCraith, D. Gray, P. Byrne, N. Kent, C. Burke and B. Paull, "Development of a micro-fluidic manifold for copper monitoring utilising chemiluminescence detection", *Lab on a Chip*, Vol. 4, 2004

4. C. S. Burke, L. Polerecky and B.D. MacCraith, "Design and fabrication of enhanced polymer waveguide platforms for absorption-based optical chemical sensors", *Meas. Sci. Tech.*, Vol. 15, Iss. 6, pp. 1140-1145, 2004.

5. C. S. Burke, O. McGaughey, J-M. Sabattié, H. Barry, A. K. McEvoy, C. McDonagh and B. D. MacCraith, "Development of a sol-gel-based integrated optical oxygen sensor using rapid prototyping technology", submitted to *The Analyst*, 2004

Appendix A

Derivation of guidance condition in an asymmetric slab waveguide

The following is a standard wave optics approach to the analysis of guidance conditions within an asymmetric slab waveguide and can be found in *Electromagnetic Principles of Integrated Optics* by Donald L. Lee (John Wiley & Sons, 1986).

The guidance condition for TE modes is given by

$$\nabla \times \tilde{E} = -\mu \frac{\partial \tilde{H}}{\partial t} = -\omega j \mu \, \tilde{H} \tag{A.1}$$

From the definition of the curl of a field and knowing that the electromagnetic fields are independent of y (i.e., $\partial/\partial y = 0$), we can write

$$(\vec{\nabla} \times \vec{E})_x = \left(-\frac{\partial E_y}{\partial z}\right) \tag{A.2}$$

$$(\vec{\nabla} \times \vec{E})_y = \left(\frac{\partial E_x}{\partial z} - \frac{\partial E_z}{\partial x}\right) \tag{A.3}$$

$$(\vec{\nabla} \times \vec{E})_z = \left(\frac{\partial E_y}{\partial x}\right) \tag{A.4}$$

Further simplification is possible knowing that, for TE modes, $E_z = 0$ and $\partial/\partial z = -jk_z$, yielding

$$(\vec{\nabla} \times \vec{E})_x = (jk_z E_y) \tag{A.5}$$

$$(\vec{\nabla} \times \vec{E})_y = (-jk_z E_x) \tag{A.6}$$

$$(\vec{\nabla} \times \vec{E})_z = \left(\frac{\partial E_y}{\partial x}\right) \tag{A.7}$$

However, equation A.1 states

$$\nabla \times \tilde{E} = -\mu \frac{\partial \tilde{H}}{\partial t} = -\omega j \mu \tilde{H} \tag{A.8}$$

which makes it possible to generate the following (equating x, y and z components)

$$jk_z E_y = -\omega j \mu H_x \tag{A.9}$$

$$-jk_z E_x = -\omega j \mu H_y \tag{A.10}$$

$$\frac{\partial E_y}{\partial x} = -\omega j \mu H_z \tag{A.11}$$

For guided TE modes, the fields are assumed to be of the form

$$E_y(x,z) = \left\{ \begin{array}{l} E_l \exp[-\alpha_l x] \\ E_g \cos(k_x x + \psi) \\ E_s \exp[+\alpha_s x] \end{array} \right\} \exp[-jk_z z] \quad \begin{array}{l} \text{Cover} \\ \text{Waveguide} \\ \text{Substrate} \end{array} \tag{A.12}$$

where the transverse wavenumbers are defined by the appropriate dispersion relation in each region

$$\alpha_l = \sqrt{k_z^2 - \omega^2 \mu_l \epsilon_l} \tag{A.13}$$

$$\alpha_s = \sqrt{k_z^2 - \omega^2 \mu_s \epsilon_s} \tag{A.14}$$

$$k_x = \sqrt{\omega^2 \mu_g \epsilon_g - k_z^2} \tag{A.15}$$

and ψ is a phase term, representing the asymmetry of the structure. In order to elucidate the relationship between ψ and the amplitude coefficients, $E_l - E_s$, we exploit the requirement of continuity of tangential E and H at both interfaces, i.e., at $x = \pm d/2$. The tangential component of H can be obtained from equation A.11, which yields

$$H_z(x,z) = \frac{j}{\omega \mu} \frac{\partial}{\partial x} E_y(x,z) \tag{A.16}$$

From (A.12), therefore

$$H_z(x,z) = \left\{ \begin{array}{l} \frac{-j\alpha_l}{\omega\mu_l} E_l \exp[-\alpha_l x] \\ \\ \frac{-jk_x}{\omega\mu_g} E_g \sin(k_x x + \psi) \\ \\ \frac{j\alpha_s}{\omega\mu_s} E_s \exp[\alpha_s x] \end{array} \right\} \exp[-jk_z z] \quad \begin{array}{l} x > d/2 \\ |x| \leq d/2 \\ x < -d/2 \end{array} \tag{A.17}$$

Applying boundary conditions at $x = d/2$ results in

$$E_l \exp[-\alpha_l d/2] = E_g \cos(k_x d/2 + \psi) \tag{A.18}$$

$$E_l \exp[-\alpha_l d/2] = \frac{\mu_l k_x}{\mu_g \alpha_l} E_g \sin(k_x x + \psi) \tag{A.19}$$

Equating the right-hand sides of these equations and taking their ratio gives

$$\tan(k_x d/2 + \psi) = \frac{\mu_g \alpha_l}{\mu_l k_x} \tag{A.20}$$

In a similar fashion, applying boundary conditions at $x = -d/2$ yields

$$\tan(k_x d/2 - \psi) = \frac{\mu_g \alpha_s}{\mu_s k_x} \tag{A.21}$$

Taking into account the fact that $\tan x = \tan x \pm n\pi$, equations A.20 and A.21 can be rewritten as

$$k_x d/2 + \psi = \tan^{-1}\left(\frac{\mu_g \alpha_l}{\mu_l k_x}\right) \mp n\pi \tag{A.22}$$

and

$$k_x d/2 - \psi = \tan^{-1}\left(\frac{\mu_g \alpha_s}{\mu_s k_x}\right) \mp m\pi \tag{A.23}$$

Further manipulation yields

$$k_x d/2 + \psi = \tfrac{1}{2}\phi_l^{TE} \pm n\pi \tag{A.24}$$

$$k_x d/2 - \psi = \tfrac{1}{2}\phi_s^{TE} \pm m\pi \tag{A.25}$$

where

$$\phi_l^{TE} = \tan^{-1}\left(\frac{\mu_g \alpha_l}{\mu_l k_x}\right) \tag{A.26}$$

$$\phi_s^{TE} = \tan^{-1}\left(\frac{\mu_g \alpha_s}{\mu_s k_x}\right) \tag{A.27}$$

Adding equations A.24 and A.25 to eliminate ψ produces

$$2k_x d - \phi_l^{TE} - \phi_s^{TE} = 2p\pi \qquad p = 0, 1, \ldots \tag{A.28}$$

This generalised guiding condition for TE modes within an asymmetric slab waveguide can be simplified by substituting for k_x, ϕ_l^{TE}, ϕ_s^{TE}, α_l and α_s from equations A.13 – A.15, A.26 and A.27 to obtain

$$d\sqrt{\omega^2\mu_g\epsilon_g - k_z^2} = p\pi + \tan^{-1}\left(\frac{\mu_g\sqrt{k_z^2-\omega^2\mu_l\epsilon_l}}{\mu_l\sqrt{\omega^2\mu_g\epsilon_g-k_z^2}}\right) + \tan^{-1}\left(\frac{\mu_g\sqrt{k_z^2-\omega^2\mu_s\epsilon_s}}{\mu_s\sqrt{\omega^2\mu_g\epsilon_g-k_z^2}}\right) \tag{A.29}$$

Knowing $k_z = \omega\sqrt{\mu\epsilon_{eff}}$ and assuming magnetic equivalence yields

$$d\omega\sqrt{\mu}\sqrt{\epsilon_g - \epsilon_{\text{eff}}} = p\pi + \tan^{-1}\left(\sqrt{\frac{\epsilon_{\text{eff}} - \epsilon_l}{\epsilon_g - \epsilon_{\text{eff}}}}\right) + \tan^{-1}\left(\sqrt{\frac{\epsilon_{\text{eff}} - \epsilon_s}{\epsilon_g - \epsilon_{\text{eff}}}}\right) \tag{A.30}$$

The following parameters are now defined

$$b = \frac{\epsilon_{\text{eff}} - \epsilon_s}{\epsilon_g - \epsilon_s} \tag{A.31}$$

and

$$a^{TE} = \frac{\epsilon_s - \epsilon_l}{\epsilon_g - \epsilon_s} \tag{A.32}$$

where b is the normalised waveguide index and a^{TE} is a measure of the asymmetry of the waveguide for TE modes. Having equations A.31 and A.32, it is possible, by simple manipulation to rewrite equation A.30 as

$$d\omega\sqrt{\mu}\sqrt{\epsilon_g - \epsilon_{\text{eff}}} = p\pi + \tan^{-1}\left(\sqrt{\frac{b + a^{TE}}{1 - b}}\right) + \tan^{-1}\left(\sqrt{\frac{b}{1 - b}}\right) \tag{A.33}$$

Finally, a normalised frequency parameter, V (the V number), is defined. This is a measure of the number of modes a waveguide may support

$$\mathrm{V} = k_0\, d\sqrt{(\epsilon_g - \epsilon_s)/\epsilon_0} \tag{A.34}$$

where $k_0 = \omega\sqrt{\mu\epsilon_0}$. This means V can, alternatively, be defined as

$$\mathrm{V} = d\omega\sqrt{\mu}\sqrt{(\epsilon_g - \epsilon_s)} \tag{A.35}$$

Therefore

$$\mathrm{V}\sqrt{1 - b} = d\omega\sqrt{\mu}\sqrt{(\epsilon_g - \epsilon_{\text{eff}})} \tag{A.36}$$

and equation A.33 can be rewritten as

$$V\sqrt{1-b} = p\pi + \tan^{-1}\left(\sqrt{\frac{b+a^{TE}}{1-b}}\right) + \tan^{-1}\left(\sqrt{\frac{b}{1-b}}\right) \tag{A.37}$$

Equation A.37 fully describes the guidance condition for TE modes within a planar waveguide.

Appendix B

Photomask / SU-8 template designs

Figure B.1: Photomask used to define the SU-8 template for the fabrication of the PDMS flowcell used during the pH sensing experiments described in Chapter 7.

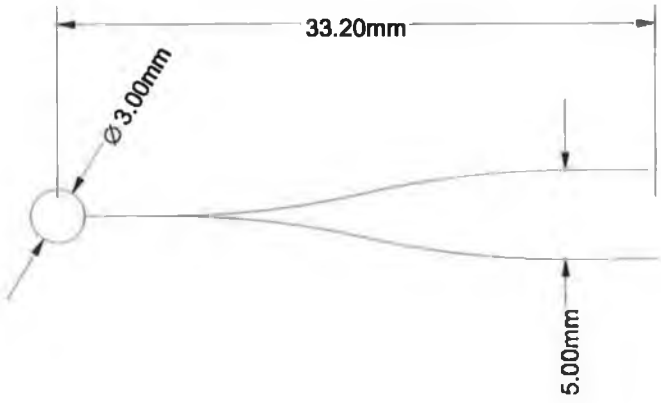

Figure B.2: Design of optical Y-splitter fabricated by UV laser writing (see Chapter 8, Sec. 8.4)

Appendix C

LabVIEW programs

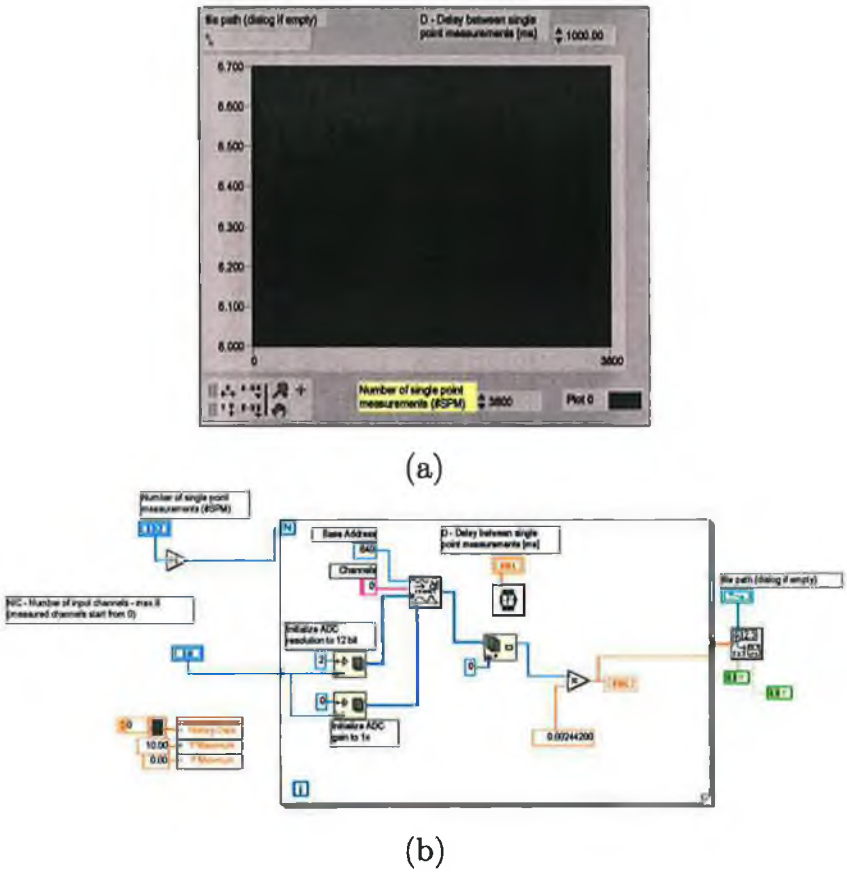

(a)

(b)

Figure C.1: (a) Front panel of Labview VI used to acquire data from LED-prototype sensors presented in Chapters 6 and 7 and (b) corresponding block diagram.

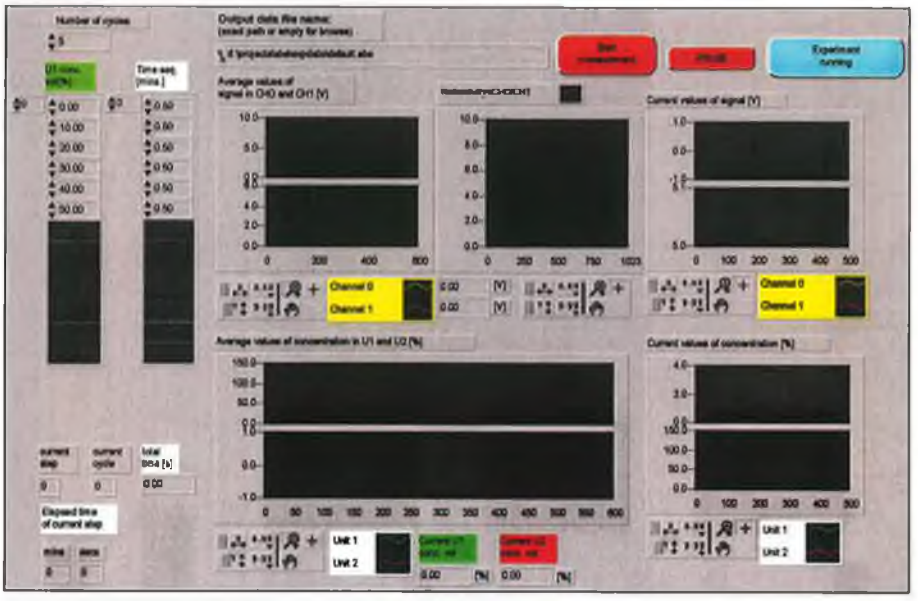

(a)

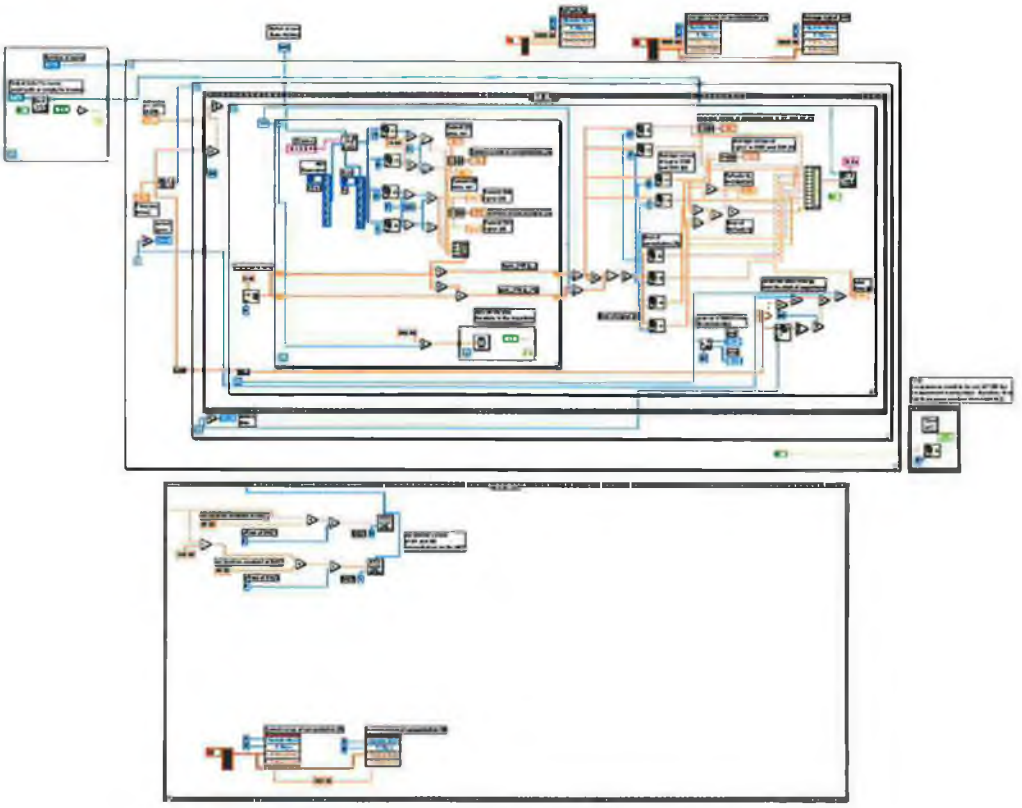

(b)

Figure C.2: (a) Front panel of Labview VI (virtual instrument) used to acquire reflectivity data presented in Chapter 6 and (b) corresponding block diagram.

Appendix D

Circuit diagrams

Note: all three circuits designed and fabricated by Lubos Polerecky and Jaroslav Hamrle.

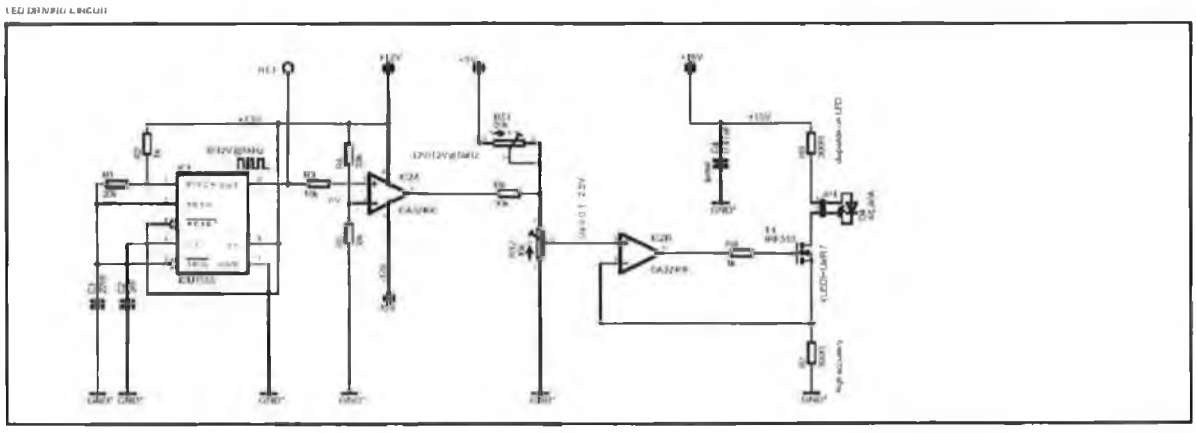

Figure D.1: LED driver circuit.

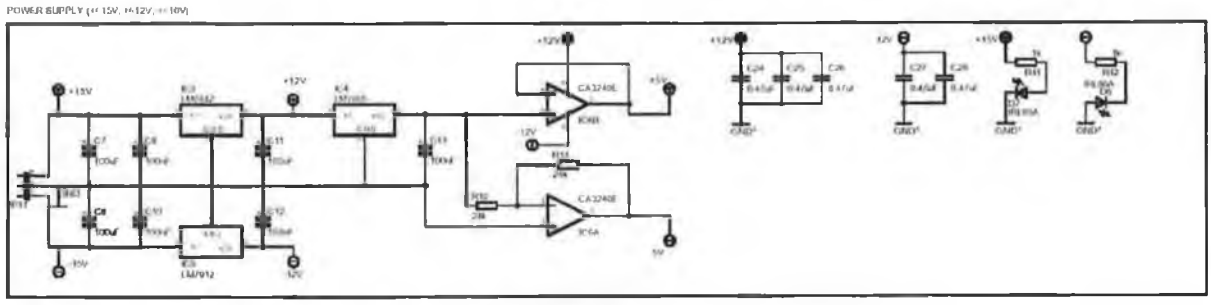

Figure D.2: Power supply.

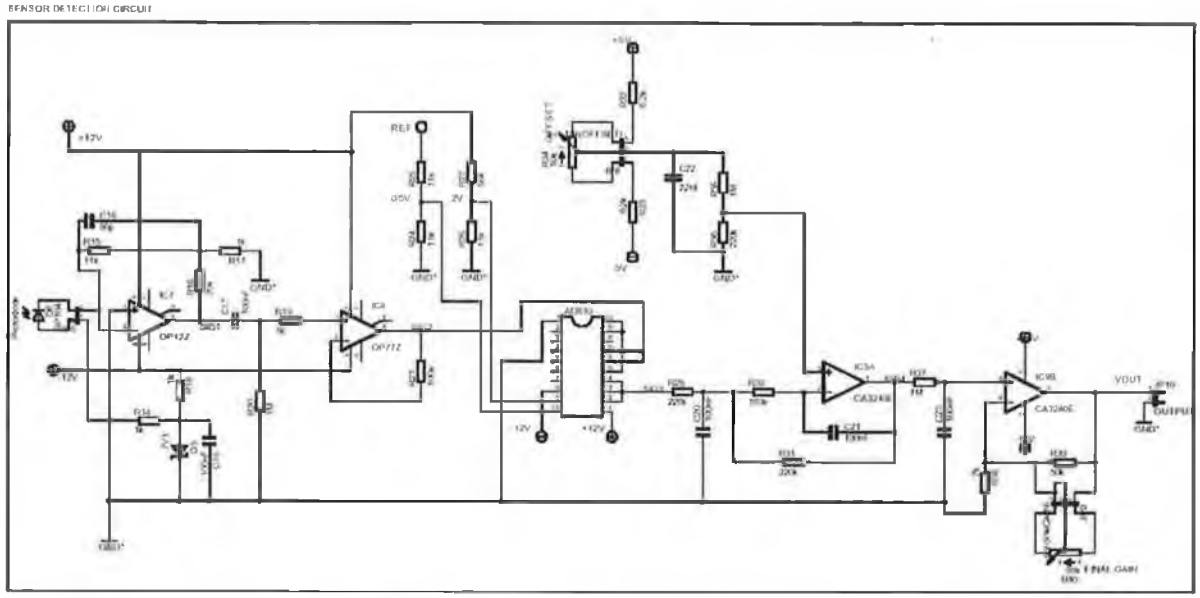

Figure D.3: Detection circuit.